ABSTRACT

FREGOSI, DANIEL JESSE. Ripple Droop Control: Control of Distributed Storage Devices with Droop Control using AC Voltage Injection. (Under the direction of Subhashish Bhattacharya.)

This work is concerned with the control of distributed devices on the power distribution system using a power-line signal injection technique. We propose a method to control power transfer in a plug-and-play manner from distributed energy storage devices such as plug-in electric vehicles without the use of external communications. Ripple voltage injection has been used to control distributed loads to implement demand response. We propose a novel technique to improve ripple control by utilizing power-frequency droop on the injected signal to control the power flow of distributed storage devices. Droop enables an arbitrary number of distributed devices to communicate bi-directionally with a defined response time to achieve power sharing. By controlling distributed storage through ripple control, communication systems on the grid are freed to perform other functions. This thesis is an effort to demonstrate the feasibility of the proposed method and to identify the potential issues and propose appropriate solutions for ripple droop control.

Ripple Droop Control: Control of Distributed Storage Devices with Droop Control using AC Voltage Injection

by
Daniel Jesse Fregosi

A dissertation submitted to the Graduate Faculty of
North Carolina State University
in partial fulfillment of the
requirements for the degree of
Doctor of Philosophy

Electrical Engineering

Raleigh, North Carolina

2014

APPROVED BY:

Srdjan Lukic	Mo-Yuen Chow
Xiangwu Zhang	Subhashish Bhattacharya Chair of Advisory Committee

DEDICATION

In this thesis and in all that I do, I strive to be a humble servant to God, from whom I have received everything.

BIOGRAPHY

Danny Fregosi was raised in Harrisburg and then Concord North Carolina. He is the son of Lorrie and Ronald and the younger brother of Josh. Danny graduated from Central Cabarrus High School and got his Bachelor's degree from NC State. He married his wife Anna while in Graduate School. Upon finishing his degree, Danny will begin working for Bosch in Mooresville, NC.

ACKNOWLEDGEMENTS

I would like to thank the organizations who supported me during my graduate studies. First I would like to thank the leaders in the ECE department at NC State and at the FREEDM Systems Center for providing excellent opportunities for education and research. I would like to thank the MIT Lincoln Laboratories and the US Department of Defense for funding me through fellowships. Lastly, I would like to thank Sandia National Laboratories for their generous student internship program.

I would like to thank all of those who mentored me during my time at NC State: my advisor Dr. Subhashish Bhattacharya for his support, guidance, and his overall enthusiasm for research; Dr. Stan Atcitty for his professional, technical, and personal mentoring; Dr. Leda Lunardi for her guidance, especially during the difficult first year of graduate school; and the numerous other professors who put the effort into being excellent teachers.

Finally, I'd like to thank my family: Anna, Mom, Dad, Josh, Dianne, Mya, Tabb, Tena, and Nathan, for their love and support. I'd like to thank my church families at Hope and at Brooks. Finally I'd like to thank the friends I have made at FREEDM who have helped me in my schoolwork and in providing a fun and interesting atmosphere to work: Tom, Ryan, Phil, Ghazal, Mengqi, Edward, Saman, Babak, Behzad, Hesam, Lee, Seunghun, Eric, Arun, Karen, Hulgize, and many others.

TABLE OF CONTENTS

LIST OF TABLES

LIST OF FIGURES

Chapter 1

Introduction

1.1 Background

A major challenge to overcome for the widespread adoption of renewable energy sources is their intermittency or non-dispatchable nature. In grids with high renewable energy penetration, intermittency can lead to instability caused by generation load mismatch [32], [30], [12].

The stability issue can be mitigated with the use of energy storage. Researchers at the Pacific Northwest National Laboratory have examined the storage requirements for accommodating an increase of renewable sources in the Northwest Power Pool [24], [29]. The researchers studied the impact of increasing the wind energy resource from 3.3 GW to 14.4 GW. They found the total intra-hour balancing requirement for the power system to be nearly 4 GW in both the generation increment and decrement directions to satisfy a 99.5% probability that the storage will be sufficient to balance the system. To illustrate the balancing requirement, the researchers simulated a typical balancing requirement signal for the Northwest Power Pool. Figure 1.1 and Figure 1.2 illustrate the dynamic

storage power needed to accommodate the wind power over one day and one month respectively.

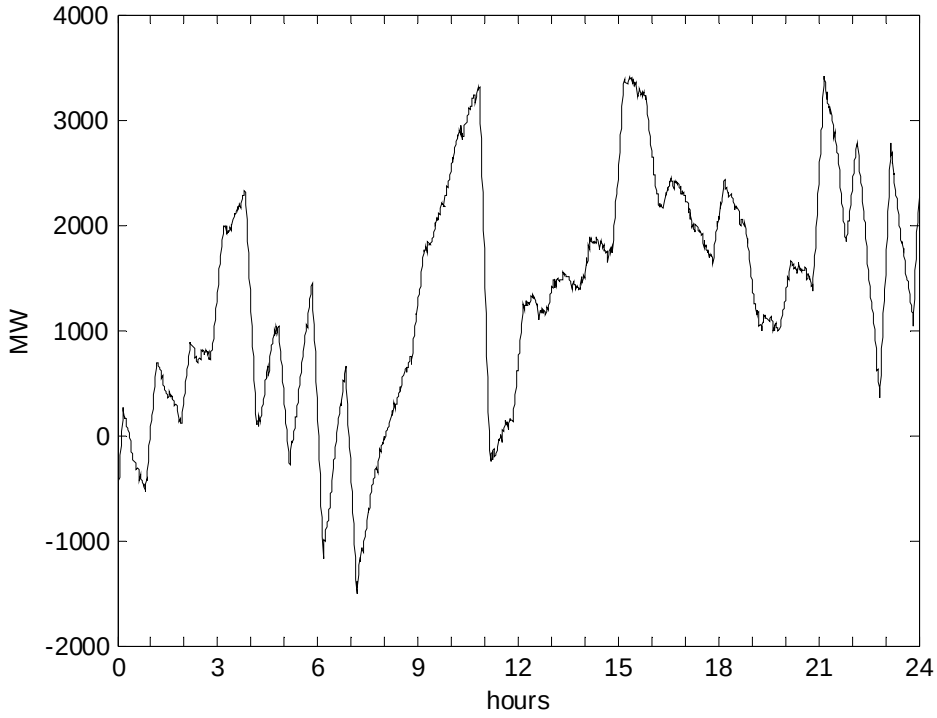

Figure 1.1: Balancing Requirement for NWPP for August Day [24]

Numerous studies have described the various benefits of adding storage to the utility grid. A report from the U.S. Department of Energy defines various ancillary services for the power grid [1]. Many of these services can be supplied by energy storage such as:

- Regulation - minute by minute generation/load balance within a control area
- Spinning Reserve - on-line generation capacity that can respond within 10 minutes to compensate for generation or transmission outages
- Frequency Response - spinning reserve that responds within 10 seconds

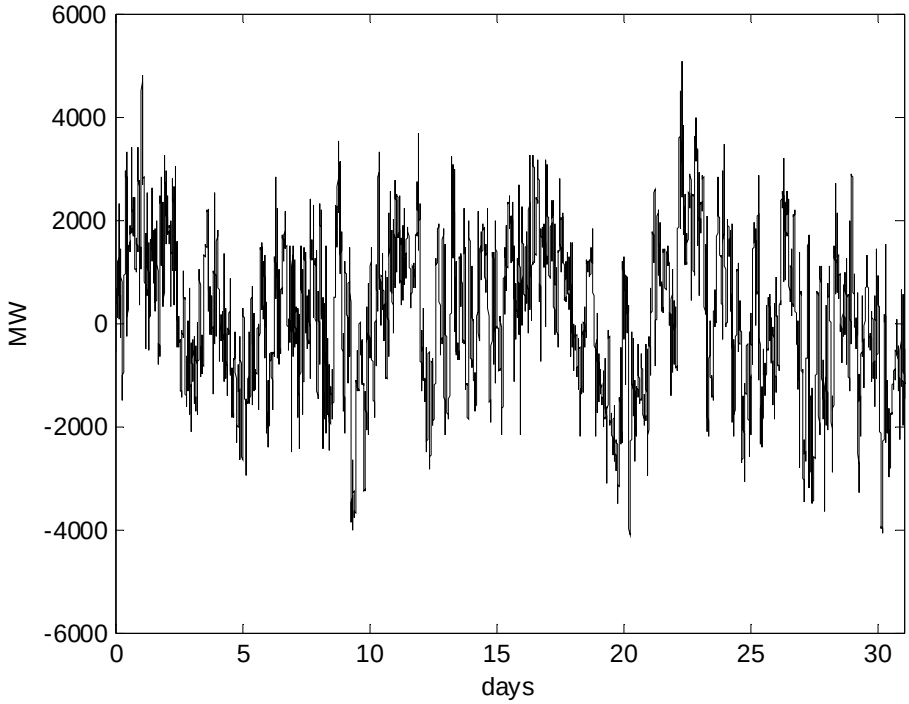

Figure 1.2: Balancing Requirement for NWPP for August Month [24]

- Supplemental Reserve - off-line capacity that can respond within 10 minutes
- Load Following - meeting hour-to-hour and daily load variations
- Backup Supply - generation within an hour, for backing up reserves

There are many promising technologies for utility scale storage or bulk storage such as batteries, flywheels, superconducting magnetic energy storage and compressed air [34]. Researchers at Sandia National Laboratories have studied the value for supplying such services to the grid [14], [13], and have examined the costs associated with the various forms of storage [15]. Results from their studies are summarized in Table 1.1. These results show that presently the value that is added for supplying the various ancillary services comes close to justifying the storage cost. As the ancillary service requirements

increase with increasing renewable energy penetration, storage becomes an even more viable solution.

Table 1.1: Value of Ancillary Services and Cost of Storage Technologies [14][15]

Storage Application		Life-cycle Estimated Benefit
Bulk Electricity Price Arbitrage		\$200 to \$300/kW
Transmission Support		\$169/kW
Renewables Capacity Firming		\$192/kW
Storage Technology	Energy Cost	Power Cost
Lead-acid Batteries (VRLA)	\$200/kWh	\$225/kW
Lithium-Ion Batteries	\$500/kWh	\$175/kW
Sodium-Sulfur Batteries	\$250/kWh	\$150/kW
Compressed Air	\$120/kWh	\$600/kW
Low-speed Flywheel	\$380/kWh	\$280/kW

In addition, electric vehicles are expected to become much more widespread in the coming years. Studies have been conducted on electric vehicles to show their impact on the electric grid and how they can be used to support increased distributed generation penetration [10], [36]. Using electric vehicle storage to provide grid support can be economically beneficial to the owner since the grid support application adds value to the storage which has already been purchased primarily for transportation. The downside of this approach is the increased cycling of the battery which may lead to degradation. Attempts must be made to study and understand the effects of increased cycling on the battery to determine the proper value of using electric vehicle batteries for grid-support. Researchers at the Pacific Northwest National Laboratory studied the feasibility of using electric vehicle storage to meet the balancing requirement that comes from adding 10 GW

of wind power to the Northwest Power Pool [38]. They found that balancing requirements can be met by utilizing the storage of 1.6 million electric vehicles that have at least a 33 mile range capacity battery if the vehicles are available for grid support while at home and at work. The 1.6 million vehicles necessary is roughly 10% of the current number of vehicles in the Northwest Power Pool. These results illustrate the large potential that exists for electric vehicle storage to add grid support, given the projected outlook on widespread electric vehicle adoption.

Researchers at Idaho National Laboratories have identified the need for communication between the charger and the electric grid so that the utility and consumer can optimize the timing of charging and discharging [44]. Existing methods for controlling distributed storage include the use of power line or wireless communication [16], [19]. These methods are capable of very high bandwidth allowing for flexibility and the use of sophisticated protocols such as IEC 61850 [3]. These communication technologies are effective for transferring large amounts of data and selectively communicating between specific nodes in a system.

However, for control operations on the power system, the latency of the communication technology is of high importance. For wireless and power line communication technologies, the communication latency is a complex function of the protocol, scheduler, amount of data, and number of nodes, routers and repeaters among other factors. In addition to controlling distributed storage, wireless or power line communication systems may be expected to simultaneously perform high level operations such as advanced metering infrastructure (AMI) functions, communication of real time pricing signals, remote sensing, and phasor measurement unit (PMU) data acquisition.

A recent study [47] examining the ability of the mobile communication network 3GPP Long Term Evolution (LTE) to meet these high-level smart grid communications needs,

found that with a scheduler designed specifically for smart-grid applications, certain latency requirements for wide-area measurement systems (WAMS) [6] and automated meter reading [22] can be met for a specific number of devices. However, the the additional responsibility of performing control of distributed storage would be highly burden the communication system.

1.2 Proposed Technique

We propose a method to control distributed devices by communicating through the power line with an injected AC signal. The proposed method does not require additional hardware as the electric vehicle charger is capable of generating the injected signal. The method allows for plug-and-play of devices and the system latency does not increase as the number of devices on the system increases. The injected signal is seen by all devices and acts as a global variable, and the devices are controlled using droop control on the injected signal.

This proposed method is called ripple droop control because it expands upon the idea of ripple control by incorporating the basic elements of frequency-droop control. Frequency droop control enables an arbitrary number of devices to communicate over the power line with a fixed system response time. This is possible with frequency droop because the system frequency acts as a global variable that can be accessed by each device simultaneously and bi-directionally. Since the system frequency is analog, the data transfer occurs continuously. In the ripple droop control application, the only constraint for the system response or latency comes from the delay associated with filtering the signal to isolate the targeted frequency and the delay associated with controlling the distributed charger to output the desired current and voltage. Furthermore, no additional

communication hardware is needed since, due to the low frequency of the signal, the power electronics in the electric vehicle chargers can be programmed to perform the ripple voltage injection.

The objective of this work is to demonstrate the ability of the proposed ripple droop control method to effectively control distributed storage devices on the power distribution system. The proposed method addresses the problem of coordinating distributed devices on the power system without the use of additional communication equipment. If a communication infrastructure exists on a feeder in which ripple droop control is implemented, the communication system can be used as a backup in case of a failure in ripple droop control.

For implementation of ripple droop control, the distributed devices must be able to supply and absorb power on command and they must be controlled by a standard power electronics inverter, capable of generating the ripple droop signal. The distributed devices can be any combination of generation, load and storage.

The proposed method utilizes the inherent advantages of frequency droop control, which include:

- a global control variable (the frequency of the voltage signal). This is the frequency of the fundamental voltage in traditional droop and the frequency of the injected voltage in ripple droop. The frequency defines the system state and all devices on the system have simultaneous read and write access to it.

- power sharing in steady state according to droop slopes of the individual devices. This is a result of the uniform frequency of the system in steady state.

- ability of the system to return to an equilibrium upon changes in load and the addition or removal of devices (plug-and-play ability).

The advantages of droop control are so beneficial that researchers have found numerous applications for which droop can be used. Many of these applications are described in the next chapter.

This work is the presentation of a previously unexplored application of droop control. The contributions in this work include:

- the use of frequency droop on injected signal in the distribution system.
- the use of central inverter to control the frequency of the system by drawing and supplying power to the injected signal. The central inverter is able to command a specific quantity of power from the distributed inverters through a simple control loop with a single integrator term.
- performing single phase droop control on a three phase system at zero sequence. The coordination is done by central inverter in order to generate only zero sequence voltages which can be easily filtered to avoid upstream propagation.
- a method to identify the number of distributed EV plugged in to the system and to determine the amount of of power lost through the injected signal into loads. This self commissioning process is necessary for the accuracy of the proposed method in drawing a specific quantity of power from distributed sources.
- a linearized state-space model of the ripple droop control system with distributed inverters on the IEEE 13 Bus Test Feeder.
- a three-stage cascaded controller to regulate fundamental frequency current and output ripple voltage and frequency without undesired control interactions between fundamental and ripple frequencies

Lastly, the objectives targeted in this work are:

- to explain a the derivation and basic operation of ripple droop control.
- to describe a practical application for ripple droop control.
- to present an accurate model of the system and analyze its stability
- to discuss and address the limitations of the proposed method.
- to demonstrate the method's effectiveness through simulation and hardware-in-the-loop experimentation

1.3 Organization

In the next chapter we describe the proposed method of ripple droop control. First, the predecessor of ripple droop control, ripple control is presented. Next, we give an overview of many of the previous uses of droop control. Our proposed method builds on the droop control theory previously developed. In this chapter, we describe how to utilize frequency droop on an injected signal to control distributed devices on the distribution system and how a central device is able to coordinate the distributed devices.

In the following chapter, we describe the specifications for a particular application of ripple droop control. We present specifications for the IEEE 13 bus distribution feeder under consideration, the capacity and power ratings for distributed EV batteries, schematics for the EV chargers, and parameters for ripple droop control.

In the fourth chapter, we develop a state-space system model in order to understand the dynamics of the system and to design the control. In this chapter, we analyze the stability and speed of the system by examining eigenvalues of the the system model.

Next, we attempt to address limitations of the proposed method. We present an analysis for the selection of the signal voltage, frequency, and power level. A detailed analysis of the power lost due to loads (leakage power) on the system is presented. A method for identifying the state of the system (amount of load and number of EV) is presented as a solution to the leakage issue. To address the issue of signal spilling into the transmission system, we propose zero-sequence signal injection in which the central inverter coordinates droop on all three phases. The zero-sequence signal can be easily filtered at the substation to avoid propagation of the signal into transmission. Additionally, the power electronics hardware and control are described in detail in this chapter.

Lastly, we attempt to validate the proposed method through simulation and experimentation. The ripple droop control system on the distribution feeder is simulated with average models for the power electronics components. Additionally, a switching-model system is simulated with the feeder in a Real-Time-Digital-Simulator with an external power electronics emulator and controller.

Future work includes testing the system on a variety of feeders and inclusion of more detailed active loads on the feeder.

Chapter 2

Ripple Droop Control

2.1 Review of Present Status

The ripple droop control method we propose adds droop control to the established method of ripple control, thus enabling bi-directional communication and greater control function. Before elaborating on our method, we briefly review the methods and applications of ripple control and droop control.

Ripple Voltage Injection, also referred to as Ripple Control, is a commercially available, well-established technology used in power distribution systems for demand response [33], [8]. Ripple control systems consist of a central generator that is controlled to inject a voltage into the distribution grid at a specific, non-fundamental frequency. Specific relays on the system are tuned to the ripple frequency and are programmed to connect or disconnect their loads from the grid whenever the ripple voltage is present. In this way, the ripple control operator can control all participating loads from one location without the use of additional communication equipment such as modems, dedicated lines, or wireless transmitters. Typical parameters for ripple control signals include voltages at 1% - 3% of

nominal fundamental voltage and frequencies from 100-1000 Hz. Coding techniques have been developed to enable more advanced control functions like tiered load shedding or rate scheduling. Two of the main drawbacks and technical issues associated with ripple control include:

- limited capability and flexibility due to the uni-directionality of the signal
- high ripple generator power requirement and introduction of harmonics into transmission due to spill-over of the signal into the transmission system

Our proposed method improves upon traditional ripple control and directly addresses these two drawbacks. We propose the use of frequency droop to enable all devices to communicate simultaneously in a manner similar to the way frequency droop is used in automatic generation control. To address the signal spill-over into transmission, we propose to inject the ripple voltage at zero sequence (without phase offset) in all three phases. The zero sequence voltage can more easily be filtered at the substation by a filter on the neutral wire to avoid propagation into the transmission system.

A requirement for the proposed method is that the distributed devices must be active and controlled by power electronics. The application we have focused on in this work is the control of distributed electric vehicle chargers. The electric vehicle batteries are controlled by the proposed method to provide support for the grid. With the proposed control, the distributed batteries are aggregated, acting as a single large storage device capable of rapidly responding to a power command. Specifications for the target application are given in Chapter 3 of this work and the zero-sequence signal injection is expanded upon in Chapter 5.

The advantages of the proposed method over traditional Ripple Control are enabled by the use of droop control. Droop control was first invented for and is still used for

controlling the power output of large generators connected to a power system. The main features of droop control are the ability of generators to automatically adjust their mechanical power input to match the electrical load on a system and the ability of generators to share the load proportionately without the use of external communications. The power output of a generator when connected to an infinite bus through an inductive line, such as in Figure 2.1, is given in Eq. 2.1.

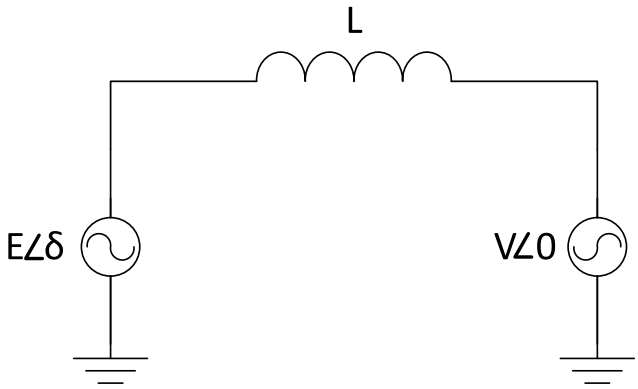

Figure 2.1: Power Flow Circuit

$$P = \frac{EV}{\omega L}\sin(\delta) \tag{2.1}$$

When the system's load varies, the current drawn through the inductor varies and the angle of the generator with respect to the angel of the system changes. Figure 2.2 and Eq. 2.2 illustrate the relationship between the voltage and current phasors.

$$\tilde{E} = \tilde{V} + \tilde{I}_L j\omega L \tag{2.2}$$

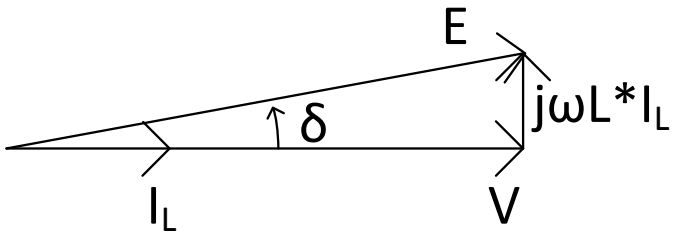

Figure 2.2: Power Flow Phasor Diagram

The power drawn from the generator initially comes from the energy stored in the rotating inertia. The frequency of the generator's rotor is proportional to the mechanical power input from the turbine minus the electrical power drawn by the load, as in Eq. 2.3.

$$\dot{\omega}_{gen} = \frac{P_m - P_e}{K_{inertia}} \tag{2.3}$$

As the electric load on the generator increases with the mechanical power constant, the rotor frequency decreases. This causes the angle between the generator and the grid to increase, further increasing the power drawn from the rotor. This positive feedback cycle is broken as the droop controller senses the change in frequency and adjusts the mechanical power input according to a predefined droop function such as Eq. 2.4, where m is the droop coefficient.

$$P_m^* = P_0 - m(\omega_{gen} - \omega_0) \tag{2.4}$$

The mechanical power is adjusted dynamically until equilibrium is reached for the rotor frequency. The frequency at which the rotor reaches equilibrium is found by rearranging the terms in Eq. 2.4 and is given in Eq. 2.5.

$$\omega_{gen} = \omega_0 - \frac{P_m - P_0}{m} \quad \text{where} \quad P_e = P_m \tag{2.5}$$

Using this simple control, a single generator and load will achieve generation-load balance. In a system with multiple generators, when an equilibrium is reached, all generators on the system be rotating at the same frequency and the system load will be shared among generators proportional to their droop coefficients as in Eq. 2.6 and Eq. 2.7 [5]. A sample equilibrium from a 3-generator system is illustrated in Figure 2.3 where the system frequency is $\omega_{equilibrium}$. This frequency acts as a global variable describing the system's state. The dynamics described in the single generator and load scenario are present between all generators in a multi-generator system. For an equilibrium to be reached, the frequency must be uniform in all generators, otherwise the relative angles would not be constant in a steady-state.

$$P_{total} = P_1 + P_2 + \cdots + P_n \tag{2.6}$$

$$\frac{P_1}{m_1} = \frac{P_2}{m_2} = \cdots = \frac{P_n}{m_n} \tag{2.7}$$

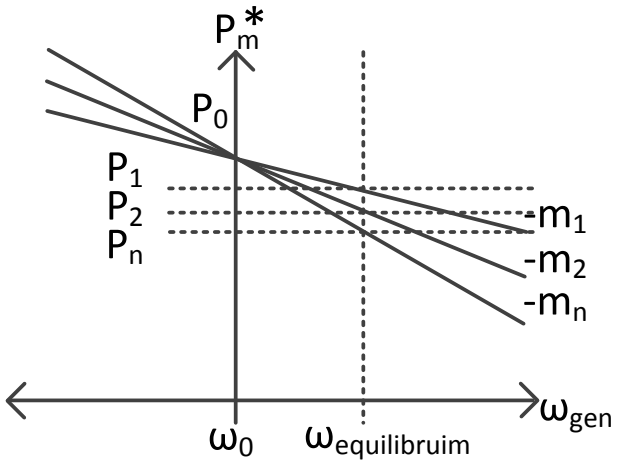

Figure 2.3: Power Sharing with Droop Control

Researchers have expanded the application of droop control to islanded micro-grids [17], [21], [18], parallel operation of uninterruptable power supplies (UPS) [7], and distributed active filters [9]. In the case of islanded micro-grids and parallel UPS, the generation in the system is often comprised entirely of inverters connected to batteries or renewable energy sources rather than synchronous generators. When the load on an inverter varies, the inverter can supply the necessary power without any change in its frequency, since the frequency is generated by the local controller and does not depend on a rotating inertia. Therefore, to achieve the same power sharing in inverters in a micro-grid as with traditional droop control in synchronous generators, a relationship between power and inverter frequency is artificially implemented in control as in Eq. 2.8.

$$\omega_{inv}^{*} = \omega_0 - m(P_{inv} - P_0) \tag{2.8}$$

Droop control in inverters is achieved by making the frequency a function of the electrical power output, contrary to droop control in synchronous generators, where the mechanical power is a function of the rotor frequency (Eq. 2.4). In both cases, the system frequency reaches equilibrium and the power output from each source can be found according to either Eq. 2.8 or Eq. 2.5. Figure 2.4 is shows the closed loop block diagram of the droop controller along with the plant for an inverter controlled by droop. The frequency of the system is represented as a disturbance input here. For a relatively a small angle (δ) the dynamics are approximately linear and first order.

Further research has been done to study the stability of droop control in a micro-grid [20], [27], and to find methods to improve the dynamic performance of droop control [23]. Researchers have used a variation of droop control for active filters to ensure that the harmonic currents are shared evenly among devices [9], [26], [41]. As nonlinear loads in-

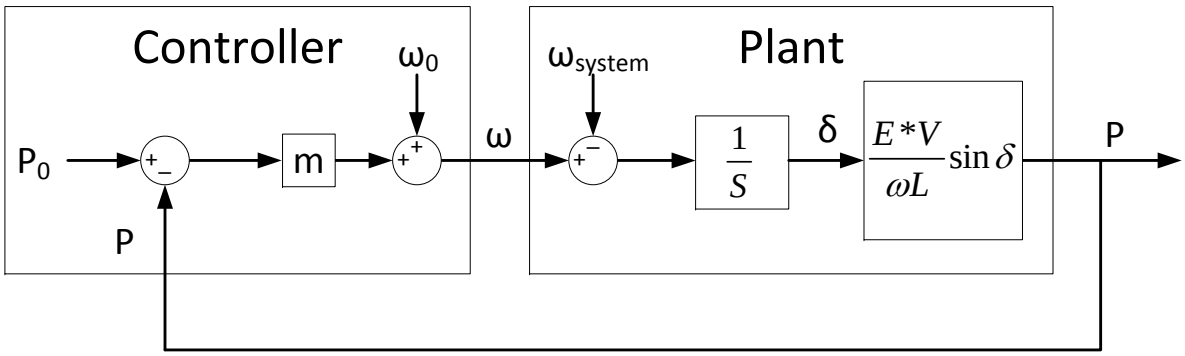

Figure 2.4: Power-Frequency Droop Closed Loop Block Diagram

crease, harmonic currents on the line increase and can be measured by the total harmonic distortion (THD) of the line current. The active filters measure the THD and adjust their conductance according to a predefined droop equation, Eq. 2.9.

$$G^*_{af} = G_0 - b(THD_{measured} - THD_0) \tag{2.9}$$

The THD is seen by all active filters on the system, thus it is a global variable. The active filters under the droop control will share the harmonic load proportional to their droop coefficients. Another variation of droop control is a method of controlling the reactive power output of inverters in a micro-grid [7]. The reactive power output of a source to an infinite bus through and inductor, as in Figure 2.1 is given by Eq. 2.10.

$$Q = \frac{E^2}{\omega L} - \frac{EV}{\omega L}\cos(\delta) \tag{2.10}$$

As a load's reactive current varies, the voltage magnitudes (E and V) vary and the load draws reactive power from the source. Under reactive power droop control, the source adjusts its voltage magnitude according to Eq. 2.11. The closed loop dynamics for Q-V

droop control are shown in Figure 2.5.

$$E^*_{inv} = E_0 - n(Q_{inv} - Q_0) \tag{2.11}$$

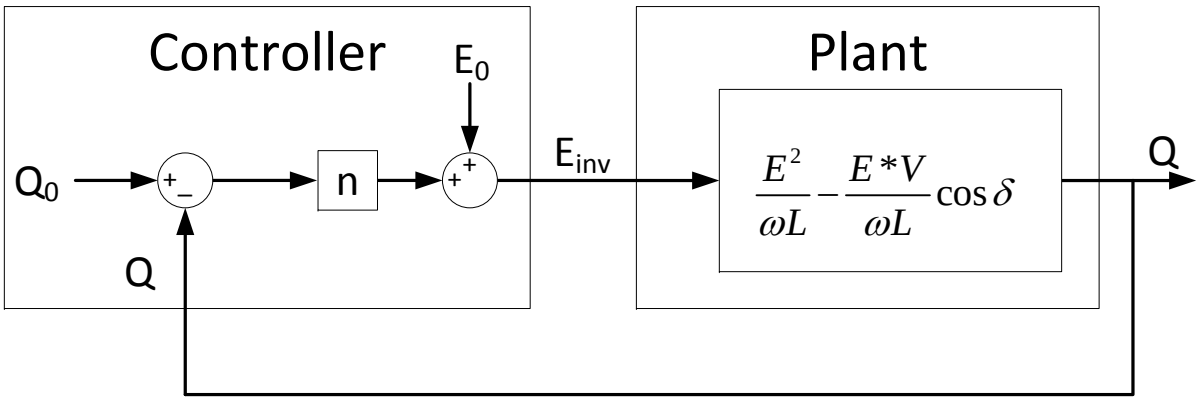

Figure 2.5: Reactive Power-Magnitude Droop Closed Loop Block Diagram

As the system reaches equilibrium, the reactive power is somewhat shared among inverters. Reactive power sharing is not completely achieved because the voltage magnitude is the variable used to control the reactive power and it is not uniform across the system. A voltage gradient across the line is necessary for the transfer of reactive power. Therefore, there is no global variable. Consequently, inverters closer to loads take on more of the reactive power load than inverters separated by larger impedances due to voltage drop across those impedances. In micro-grids, often line impedances have very low inductances such that resistance of the lines has more of an impact on the power transfer than the reactance. In this case, the real and reactive power equations given in Eq. 2.1 and Eq. 2.10 are no longer valid. For low X/R ratios, the power flow predominantly becomes a function of voltage magnitude and the reactive power flow becomes

a function of phase angle. In these cases, researchers have proposed power-voltage and reactive power-frequency droop [28], [25]. The steady-state error problem exists in this case but for real power sharing. The power is not shared evenly since the voltage is not a global variable. This problem was identified in [42] where an analogy was made between traditional droop control in the main grid and power-voltage droop control in a micro-grid. In this work, the authors suggest the global variable for power sharing should be the DC voltage of each inverter. For this variable to be shared among all converters, the authors suggest communication to be installed to transmit the information.

Lastly, researchers have addressed the problem of lacking a global variable in certain cases when performing droop control and proposed a solution involving a signal injection. These researchers studied a predominantly inductive micro-grid system for which inverters share the real power, reactive power, and harmonic current [39], [40]. Here the sharing of real power was accomplished through traditional power-frequency droop control. However, for the sharing of both reactive power and harmonic current, the researchers used AC signals injected into the line at two alternate frequencies to represent the amount of reactive power and harmonic current sourced by each inverter. The amount of power transferred in each of these signals is proportional to the variable each one represents. The researchers achieved uniform sharing of reactive power and harmonic currents by decoupling the variable used for communication from the quantity under control. In other words, for real power sharing, the fundamental voltage frequency both communicates the state of the system and controls power transfer. For reactive power sharing, communication is achieved through the small injecting a signal, while the act of controlling reactive power flow is achieved by altering the inverter fundamental voltage magnitude. The authors show how to use droop control as simply a method of communication among distributed devices on a power system. The authors demonstrated that the small power

levels transferred at the alternate frequency can be used to control and represent other quantities in the system. Figure 2.6 shows the closed loop block diagram for this reactive power droop method.

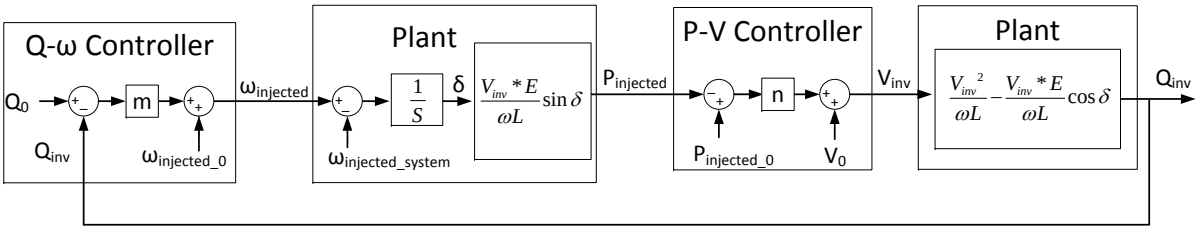

Figure 2.6: Reactive Power Sharing with Droop in Injected Signal

The researchers modified the traditional method, as shown in Figure 2.5, to include frequency droop. The presence of the integrator in the power transfer plant ensures that the frequency is uniform at steady state, therefore the quantity being controlled is shared with no error.

2.2 Proposed Technique

The proposed method extends the droop concept by attempting to control distributed devices in the power distribution system (rather than in a micro-grid) as in Figure 2.7. This method differs from previous applications of droop for inverters because these inverters are connected to a stiff grid, where local inverters in distribution cannot communicate by altering the system frequency. Instead a signal is injected at a different frequency whose scope is local. Power-frequency droop is performed on this superimposed signal, and a small quantity of power is transferred among the inverters at the alternate frequency. The quantity of power transferred at the alternate frequency is then scaled up by a defined

constant to determine the desired power to be transferred from the distributed device at fundamental frequency. In this way, the injected signal is used to coordinate and control the distributed devices.

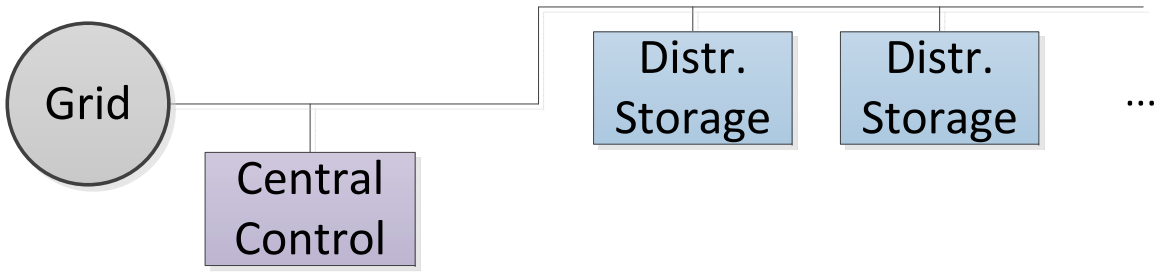

Figure 2.7: Central Control and Distributed Storage on a Feeder

Power sharing occurs at steady state because the injected signal frequency is uniform across the system. The same closed loop dynamics that occur in droop control of inverters in a micro-grid (Eq. 2.8 and Figure 2.4) apply to ripple droop control. The power transferred in the ripple signal is controlled in a closed loop manner, while the fundamental power to be transferred is simply an output variable. This is illustrated in Figure 2.8.

An important distinction of ripple droop control from previous droop methods is the ability to command a specific quantity of power rather than just reacting to changes in the system (load, reactive load, harmonics, etc.). In other words, there is a controllable input to the system. In ripple droop control, the input is received by the central inverter from an external source. All distributed inverters react to the frequency of the injected signal and are controlled with no external communication. The closed loop portion of

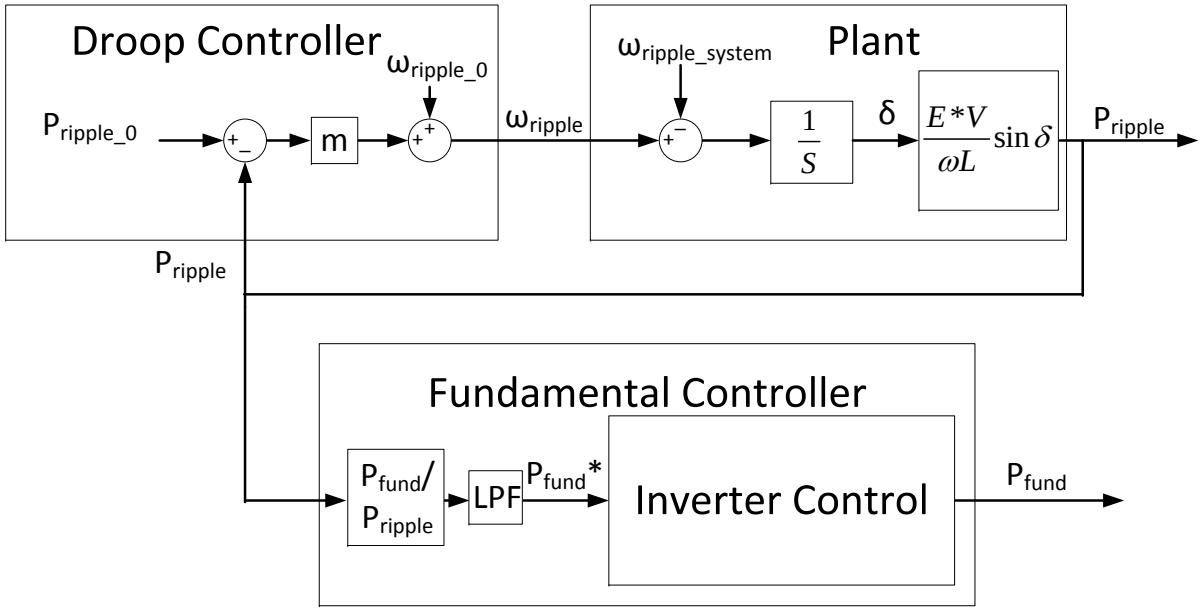

Figure 2.8: Real Power Sharing with Droop in Injected Signal

Figure 2.8 shows the distributed controller's function of adjusting its frequency in response to the power drawn in the injected signal. P_{ripple_0} is a constant control parameter although it is placed where an input is commonly placed in a closed loop block diagram. A rearrangement of this block diagram in Figure 2.9 places ω_{ripple_system} as the input. This illustrates how the power in the injected signal can be altered by changes in the system frequency.

In ripple droop control the system frequency is set by the central controller, whereas in traditional droop control the system frequency is set as a function of the load on the system. The central controller is able to command a specific quantity of power (positive or negative) from the injected signal by altering its frequency. The central inverter is controlled according to Eq. 2.12. Its closed loop dynamics are shown in Figure 2.10.

$$\omega_{offset} = k(P^* - P)/S \tag{2.12}$$

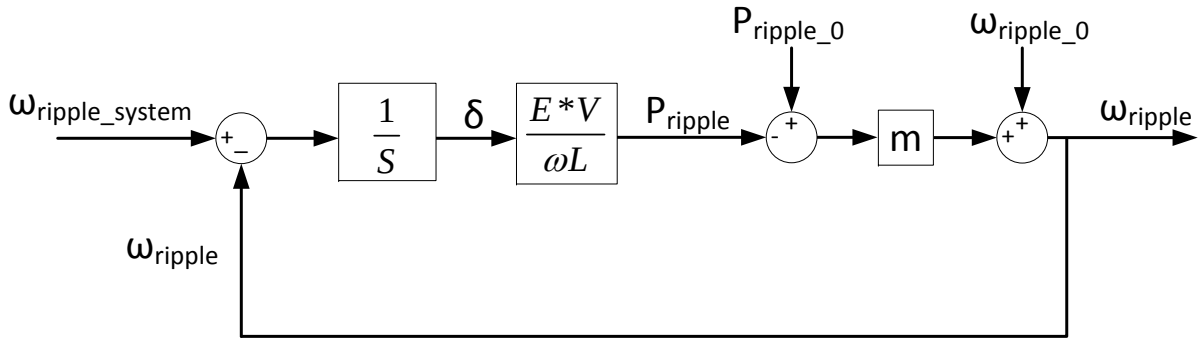

Figure 2.9: Closed Loop Block Diagram with Frequency as Input

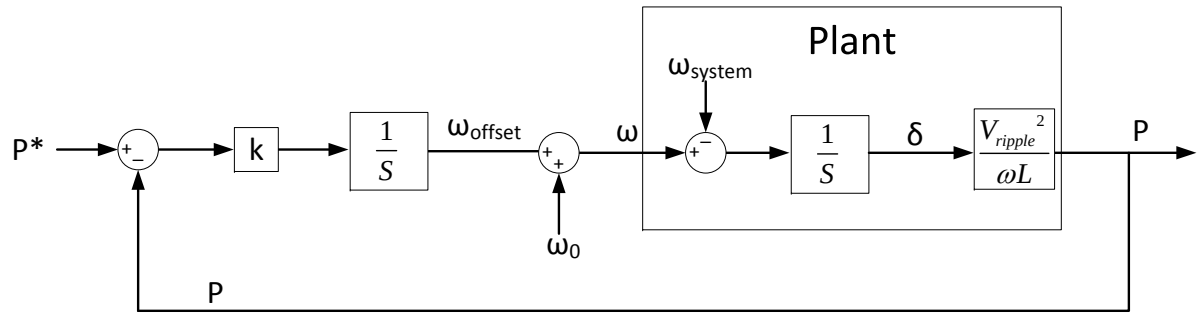

Figure 2.10: Central Inverter Closed Loop Block Diagram

A plot of the droop curve of a distributed controller and that of the central controller is illustrated in Figure 2.11. The central inverter frequency has been shifted downward from ω_0 such that its angle lags the distributed inverter's angle. Consequently, the central inverter draws power from the injected signal. The distributed inverter senses that power is drawn and adjusts its frequency according to its droop slope until an equilibrium is reached. In a system with multiple distributed inverters, the inverters share the power drawn by the central inverter according to their droop slopes, as with traditional droop control (Eq. 2.7).

In this simple control scheme only one control constant is necessary per controller.

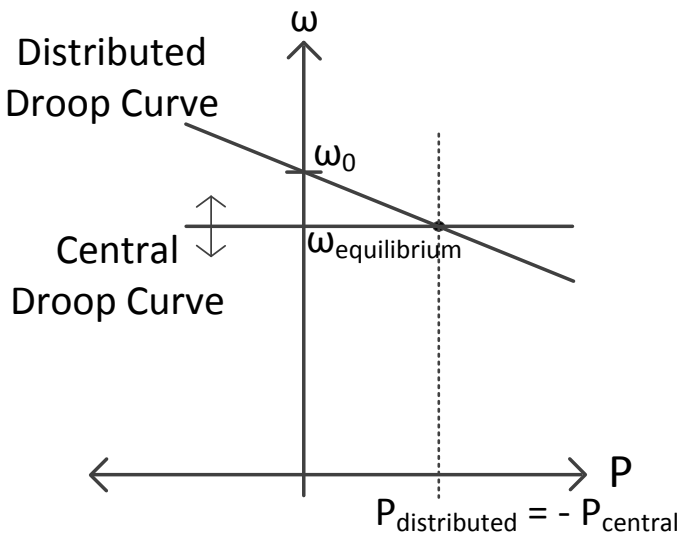

Figure 2.11: Adjustable offset droop slope

The distributed controllers have only a droop slope and the central controller has an integrator coefficient. The integrator coefficient in the central controller determines the damping of the system, while the droop slope constant determines the system response time. A system model is developed and the dynamics and stability of the system are analyzed in Chapter 4. In the following chapter, a specific application of ripple droop control is described and system specifications are given for control of EV chargers on a distribution feeder. In Chapter 6, various design considerations for ripple droop control are investigated including filtering the signal from going upstream into transmission and identifying and compensating for the signal power that is dissipated in loads on the system.

Chapter 3

Application Specifications

To illustrate the usefulness and practicality of the proposed ripple droop control method, we have targeted the application of aggregating electric vehicle chargers on a distribution system to provide frequency support to the grid. Frequency support is traditionally provided by fast-responding natural gas generators. However, energy storage and demand response are becoming increasingly economical for this application [10]. As plug-in electric vehicles (EV) become more widespread, the storage capacity added to the grid will be a valuable asset in providing stability and inertia [38].

Controlling distributed EVs for frequency support is an ideal application of ripple droop control. EV chargers contain the necessary power electronics devices and controllers to implement ripple droop control. The distributed storage on the feeder will respond to the frequency of the injected signal. Through ripple droop control, the capacity of the distributed storage is aggregated and controllable by a single central inverter. The reference power command must be communicated to the central inverter by an outside source, such as a system operator or SCADA.

3.1 IEEE 13 Bus Feeder

The IEEE 13 bus test feeder is used as the base system. All specifications for this feeder are detailed in [37]. This feeder was selected as the base for our application because it provides typical values for a distribution feeder. The feeder includes a variety of line sizes and configurations as well as both balanced and unbalanced and both delta and wye connected loads. A one-line diagram for the feeder is given in Figure 3.1.

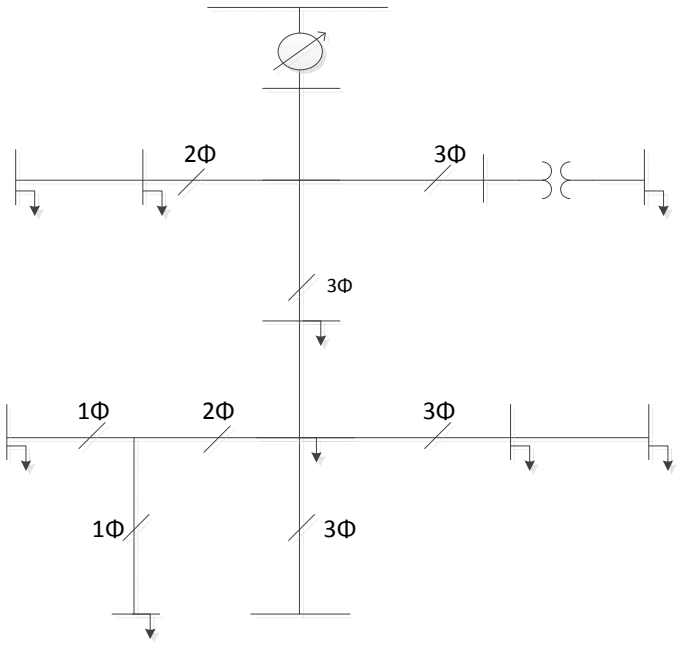

Figure 3.1: IEEE 13 Bus Feeder

Parameters for the feeder are shown in Table 3.1. The feeder has a neutral wire, and, since the phases are not balanced, the neutral wire carries current under normal conditions. The line impedances are given in the specification document in terms of self and mutual impedances for a 3-wire equivalent system. Thus the impedance of the neutral

Table 3.1: IEEE 13 Bus Feeder Parameters

Total Load	3.97 KVA	p.f. 0.9
Line Voltage	4.16 kV	(phase-phase rms)
Phase A	593.3 A	p.f. 0.88
Phase B	435.6 A	p.f. 0.93
Phase C	626.9 A	p.f. 0.90

wire is included in the impedance values and it should be modeled as an ideal conductor.

The voltage regulator steps up the voltage to 1.0625 V, 1.05 V, and 1.06875 V per unit on phases A, B, and C respectively. This is done so that all loads on the system are subject to 1 ± 0.05 V p.u. The generation and transmission system upstream of the feeder is modeled as an infinite bus.

3.2 Electric Vehicle Storage

In this application, the distributed storage on the feeder that exists in the batteries of plug-in electric vehicles can be aggregated to act as a single utility-scale energy storage system. Utility-scale energy storage systems supply mega-watts of power to the grid and can go from sourcing rated power to sinking rated power in less than a second [43], [4]. Typical values for such a system are given in the top section of Table 3.2.

The number of EV plugged into the feeder is taken to be 128 for this application. The EV chargers were placed throughout the feeder, four on each bus on each phase, according to Figure 3.2.

The power and energy rating for each EV is taken such that the capacity of the

Table 3.2: Comparison of Utility-Scale and Secondary-Use EV Energy Storage

Utility Scale Energy Storage System	
Capacity	250 kWh
Power	1 MW
Discharge Time	15 min. at rated power
Response Time	20 milli-seconds
Distributed EV Battery	
Capacity per EV Battery	20 kWh
Capacity Used for Grid-Support	1.95 kWh
Secondary Application Usage	9.75%
Charger Rating	7.2 kW
Total Number of Distributed EV	128
Total Capacity	250 kWh
Total Power	0.921 MW
Discharge Time	16 min. at rated power

battery used for grid-support is a small fraction of the overall battery capacity (9.75% in this application). The power rating for each EV is selected such that a single-phase level 2 charger is easily capable of supplying it. The bottom half of Table 3.2 gives the specifications for the individual EV battery and charger capacity and power rating. The sum of the capacities and power ratings for the distributed chargers approximately equal a single utility-scale energy storage system. To verify that the EV battery and charger power ratings are practical, several common EV battery capacities and charger sizes for level 2 chargers are given in Table 3.3 [2]. The proposed ripple droop control method can be implemented for both single-phase and three-phase systems. We assume the EV chargers are single-phase for this application because three-phase level-3 chargers not economically practical for household use.

It is interesting to note that commercially available chargers that are equipped with

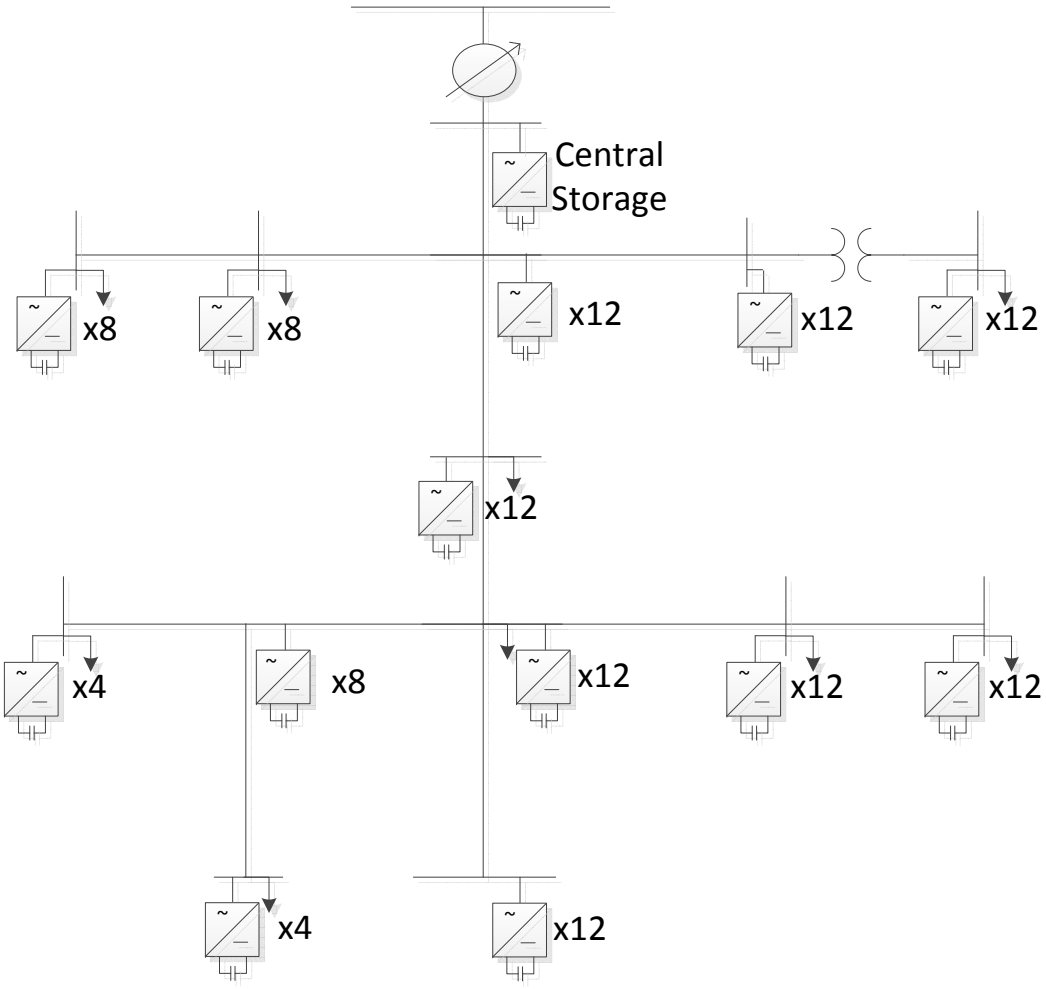

Figure 3.2: IEEE 13 Bus Feeder with 500 EV Chargers

communication technology such as the GE DuraStation ($4,500) and the Siemens Smart Grid EVSE charger are significantly more expensive than basic chargers such as the Schneider charger ($800). This illustrates the cost of communication equipment. To implement ripple droop control, the chargers need no additional hardware. The chargers all have a requisite micro-controller and current and voltage sensors necessary to perform ripple droop control.

Table 3.3: Common PHEV/EV Battery and Charger Sizes [2]

Plug-in Hybrid Electric Vehicle (PHEV)	Battery Capacity
Toyota Prius	4.4 kWh
Honda Accord	6.6 kWh
Volkswagen TwinDrive	12 kWh
Chevrolet Volt	16.5 kWh
Electric Vehicle (EV)	**Battery Capacity**
Chevrolet Spark	20 kWh
Ford Focus Electric	23 kWh
Nissan Leaf	24 kWh
Mercedes BlueZero	35 kWh
Tesla Roadster	56 kWh
Level 2 Charger (240 V/1Φ)	**Power (Current)**
GE, Schneider, Siemens	7.2 kW (30 A)
Ford	7.68 kW (32 A)
Eaton	16.8 kW (70 A)

3.3 Charger Specifications

The chargers considered in this application are off-board, bi-directional, conductive level 2 chargers. A comprehensive review of EV chargers is given in [45], and bi-directional chargers are examined specifically in [11]. The charger considered is a two-stage converter. The AC-DC stage is a single-phase half-bridge configuration. This stage converts the 240 V AC voltage to 400 V at DC. The DC-DC stage is chosen to be a bi-directional buck converter. This topology is chosen for its simplicity. If isolation is required, a dual active bridge topology could be selected instead. The DC-DC stage converts the 400 V DC bus voltage to the battery voltage of 300 V. For our control method, the AC-DC stage controls the power flow and performs the signal injection necessary for ripple droop control, while

the AC-DC stage regulates the DC bus voltage. The battery and dc-dc converter are later modeled as an ideal DC source, while they are shown here for completeness. A detailed description of the power electronics control is given in chapter 5. The overall charger schematic and list of parameters, including the distribution transformer, are given in Figure 3.3 and in Table 3.4.

Table 3.4: Bi-directional EV Charger Specifications

EV Charger	
Transformer Ratio	2.4 kV:240 V
Transformer Z	0.02 + j0.03 p.u.(50 kVA, 60 Hz)
$L_{leakage}$	91.7 μH (secondary)
AC Voltage	240 V_{rms}
Switching Frequency	10 kHz
L_{ac}	2.2 mH
C_{ac}	20 μF
V_{dc_bus}	400 V

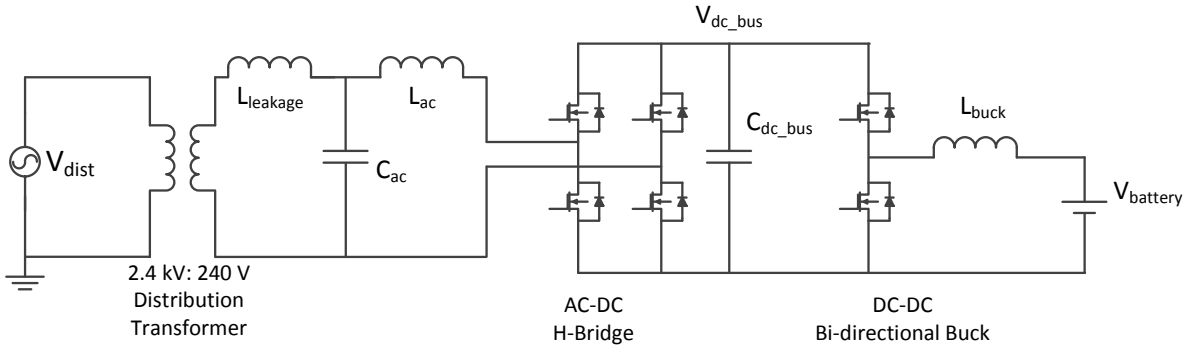

Figure 3.3: Bi-directional EV Charger Schematic

3.4 Ripple Droop Control Parameters

As mentioned in the previous section, for the target application 128 distributed EV chargers and batteries are added to the IEEE 13 bus feeder to constitute an aggregate capacity of 250 kWh and power of nearly 1 MW. In this section, the remaining parameters for the system and its control are presented. The design and selection criteria for several of the parameters presented here are explained in next couple chapters. The purpose of this section is to present the information concisely in a single location. The parameters are given in Table 3.5.

Table 3.5: Ripple Droop Control Parameters

Injected Signal	
Voltage Magnitude	3%
Frequency	90 Hz
Signal Range (Central Inverter)	3.46 kW
Power per Charger (Distributed Inverter)	27 W
Fundamental Power/Signal Power Ratio	267
Response Time	2.5 seconds
Droop Slope	0.00343 radians/s/W

The injected signal voltage magnitude is selected to be 3% of the nominal voltage, which complies with the harmonic voltage standard's recommendation of 3% for individual voltage harmonics [31]. The frequency selection and power range that the central inverter can pull from or put into the injected signal are a function of the line and filter impedance, injected signal voltage, and amount of load on the system and are derived later.

The response time is related to the speed of the controller, including the extraction filter that separates the injection signal measurements from the fundamental frequency signal and its harmonics. It is shown that the droop slopes can be set to achieve an arbitrarily fast system response, however the response time for filtering the injected signal from the line is the limiting factor. Due to the delay associated with the filtering, the system response time is limited. The central integrator gain term controls damping in the system. The system dynamics are modeled in Chapter 4.

Chapter 4

System Model

The purpose of this chapter is to model and analyze the system dynamics. By describing the system in terms of a mathematical model, we are able to quantitatively examine the stability and performance of the system. In addition, with the model we are able properly select values for the droop slope and the central inverter integrator gain term. Lastly, we examine the effects of of changing the number of distributed chargers on the system.

4.1 Model Development

In the development of the system model, a few approximations are made for simplicity and linearization. For each of the four approximations (ideal power measurement, time invariant system, inductive line, small angle), a justification is given.

Approximation 1: Ideal Power Measurement. The first approximation is that we have an ideal measurement of the magnitudes of the injected signal voltage and current. The power in the injected signal is an input to the droop controller. Ideal measurement includes the exclusion of components other than ones at the frequency of the

injected signal. Therefore, this approximation states that only power in the ripple signal is included and fundamental frequency components can be ignored. Furthermore, ideal measurement means there is no delay from changes in the actual magnitude and changes in the measured magnitude. In the extraction filter design section in the next chapter, the rejection capability and the speed of the extraction filter are examined. The speed of the filter does not have a significant effect on the dynamics of ripple droop control system if its speed is at least an order of magnitude faster than the system speed. The simple example in Figure 4.1 and Figure 4.2 illustrates a feedback loop with a delay in the feedback path.

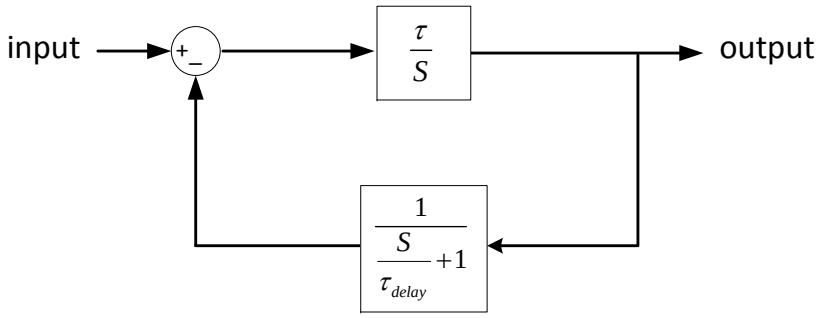

Figure 4.1: Simple Step Response with Feedback Delay

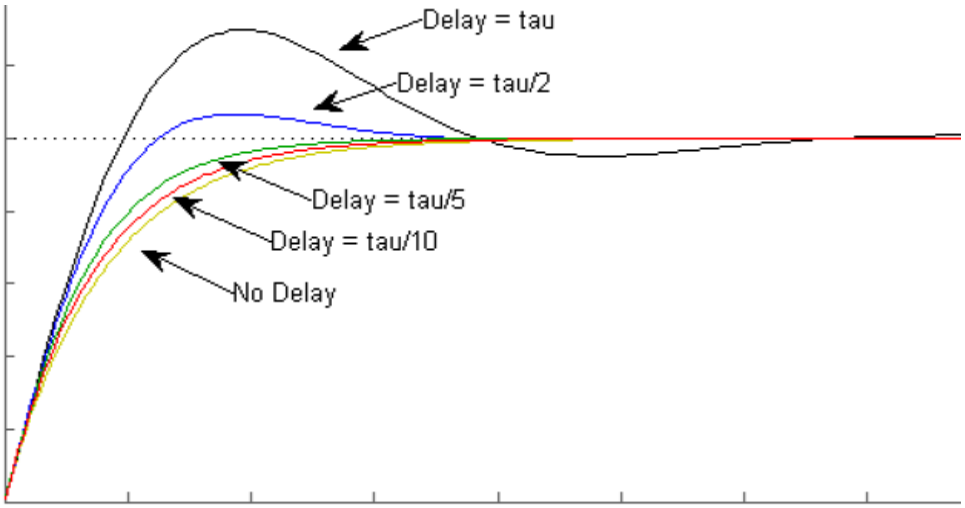

Figure 4.2: Step Response of the System with Various Delay Magnitudes

The step response of the system for delays of different values (fractions of the system time constant, τ) are shown. The results show that the diminishing effect of the delay as its time constant becomes a small fraction of the overall time constant. In the ripple droop control system, for this approximation to be accurate, the speed of the system (magnitudes of the dominant eigenvalues) should be at least an order of magnitude less than the speed of the extraction filter.

Approximation 2: System Time Invariance. The second approximation is that the system parameters in the model remain constant. The two cases in which the system model changes under normal operation is in the line reactance value and in the number and location of EV on the feeder. The line reactance seen by the injected signal is a function of the frequency of the injected signal. This approximation is accurate as long as the variations in the signal frequency are small. The system frequency varies less than 1 Hz under nominal conditions.

For the case of varying number and location of EV chargers, the approximation is

not valid. The system model changes significantly as the number and location of EV on the system changes. We desire to design a system which can accommodate the addition and removal of EV's. Therefore, we generate several models of the system under varying numbers of EV chargers in this chapter.

To describe the system, we first develop a nonlinear state-space model, then linearize the model. The states of the system are the angles of the chargers, $\delta_1, \delta_2, \ldots, \delta_n$. We will use the central inverter angle as the reference angle. The quantities of the central inverter have the subscript c in the notation. For a system with n total distributed chargers and one central inverter, there are n+1 states. The central inverter angle is not a state (since it is the reference), however, there is an integrator in the controller of the central inverter which adds a state to the system. This integrator which is used to adjust the central inverter frequency in order to meet the commanded reference power. The next-state equations are given in Eq. 4.1. In the following equations, P_x is the power supplied by charger x, P^* is reference power command, and K is gain in central inverter controller.

$$\begin{pmatrix} \dot{\delta}_1 \\ \dot{\delta}_2 \\ \vdots \\ \dot{\delta}_n \\ \dot{\omega}_{c\,offset} \end{pmatrix} = \begin{pmatrix} \omega_1 - \omega_c \\ \omega_2 - \omega_c \\ \vdots \\ \omega_2 - \omega_c \\ K(P^* - P_c) \end{pmatrix} \tag{4.1}$$

The frequencies of each charger, $\omega_1, \omega_2, \ldots, \omega_n, \omega_c$, are determined by the droop controllers in each charger. The central inverter frequency is the nominal frequency plus the offset term. These equation are shown in Eq. 4.2, where m is the droop slope and ω_0 is the nominal injected signal frequency.

$$\begin{pmatrix} \omega_1 \\ \omega_2 \\ \vdots \\ \omega_n \\ \omega_c \end{pmatrix} = \begin{pmatrix} \omega_0 - mP_1 \\ \omega_0 - mP_2 \\ \vdots \\ \omega_0 - mP_n \\ \omega_0 + \omega_{c\,offset} \end{pmatrix} \tag{4.2}$$

The power supplied by each charger (P_x) can be computed as a function of the state variables, system parameters, and inputs to the system. Its computation is derived in the next several equations. The power supplied by an AC source is given in phasor notation in Eq. 4.3.

$$P_i = real[\widetilde{V}_i \widetilde{I}_i^*] \tag{4.3}$$

The voltage magnitude is a constant parameter and its angle is a state variable, thus the voltage phasor can be computed simply. However, to find the current phasor, Kirchoff's Voltage Law must be used. For an arbitrary system with ground-connected voltage sources and loads, as in Figure 4.3 where all possible paths from the source to ground are shown, the current from any inverter, i, can be found by summing the currents along all paths as in Eq. 4.4. In this equation, Z_{ij} is the total impedance between voltage source i and j, and $Z_{load\,i}$ is the equivalent impedance from the voltage source i to ground through all loads on the system.

$$\widetilde{I}_i = \frac{\widetilde{V}_i - \widetilde{V}_1}{Z_{i1}} + \frac{\widetilde{V}_i - \widetilde{V}_2}{Z_{i2}} + \ldots + \frac{\widetilde{V}_i - \widetilde{V}_n}{Z_{in}} + \frac{\widetilde{V}_i - \widetilde{V}_c}{Z_{ic}} + \frac{\widetilde{V}_i}{Z_{load\,i}} \tag{4.4}$$

Using Eq. 4.3 and Eq. 4.4, the power from voltage source i to source j due to the current from i to j is given in complex variable notation by Eq. 4.5, where $|V|$ is the common

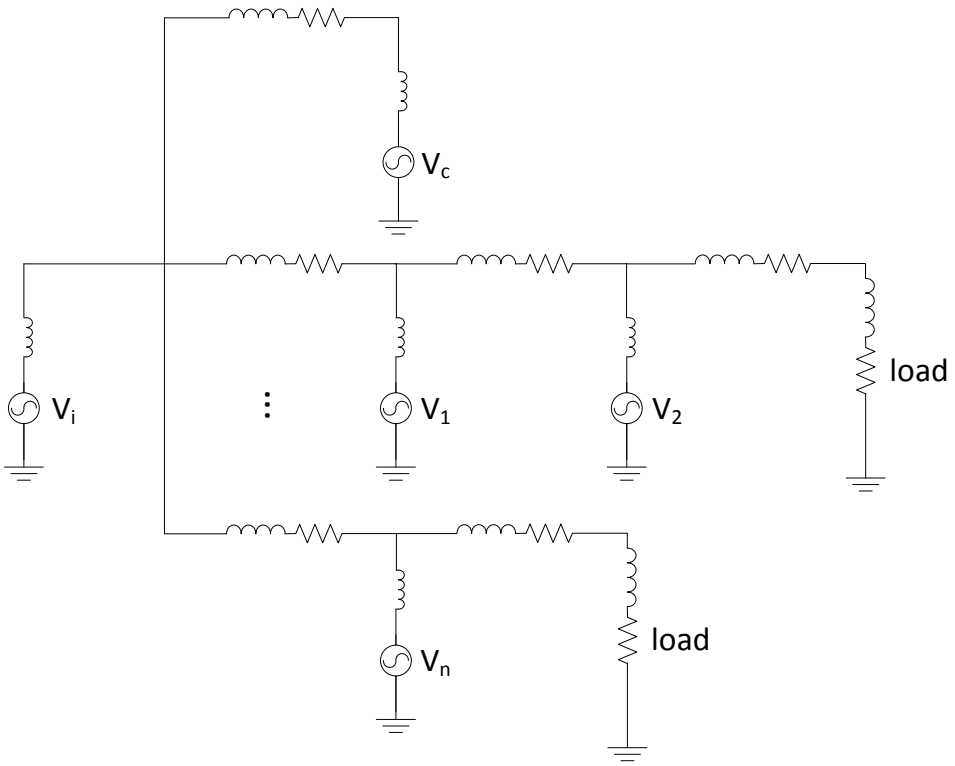

Figure 4.3: Arbitrary System with Multiple Voltage Sources and Loads

magnitude for all voltage sources.

$$P_{ij} = real[|V|\,(\cos\delta_i + j\sin\delta_i)\frac{|V|\,(\cos\delta_i - j\sin\delta_i) - |V|\,(\cos\delta_j - j\sin\delta_j)}{Z_{ij}}] \tag{4.5}$$

Multiplying the terms through gives Eq. 4.6.

$$\begin{aligned} P_{ij} = rea[\left|V^2\right|\,(&\frac{\cos^2\delta_i + \sin^2\delta_i + \cos\delta_i\cos\delta_j + \sin\delta_i\sin\delta_j}{Z_{ij}} \\ &+ \frac{j(\sin\delta_i\cos\delta_j - \cos\delta_i\sin\delta_j)}{Z_{ij}})] \end{aligned} \tag{4.6}$$

Lastly, using the trigonometric identities ($\cos^2\delta + \sin^2\delta = 1$) and ($\sin\delta_i\cos\delta_1 - \cos\delta_i\sin\delta_1 =$

$\sin(\delta_i - \delta_1)$), the equation can be simplified to Eq. 4.7

$$P_{ij} = real[\left|V^2\right| \frac{1 + \cos\delta_i \cos\delta_j + \sin\delta_i \sin\delta_j + j\sin(\delta_i - \delta_j)}{Z_{ij}}] \tag{4.7}$$

Approximation 3: Purely Reactive Line Impedance. Given that the impedance between any two sources is purely reactive, the power transfer equation simplifies to the easily recognizable form of Eq. 4.8. The approximate total power from inverter i is given in Eq. 4.9.

$$P_{ij} = \left|V^2\right| \frac{\sin(\delta_i - \delta_j)}{X_{ij}} \tag{4.8}$$

$$P_i = \left|V^2\right| (\frac{\sin(\delta_i - \delta_1)}{X_{i1}} + \frac{\sin(\delta_i - \delta_2)}{X_{i2}} + \ldots + \frac{\sin(\delta_i - \delta_n)}{X_{in}} + \frac{\sin\delta_i}{X_{ic}} + \frac{1}{R_{load\,i}}) \tag{4.9}$$

For this application, the approximation that the line impedance is purely reactive is fairly accurate. The impedance between two sources in the system is made up of the transformer impedance and the line impedance. The equivalent low voltage impedance for the line impedance is found by dividing by the square of the transformer turns ratio (10 in this case). For this system, the transformer impedance is 23 $m\Omega$ + 92 μH and the typical line impedance low voltage equivalent is 1.73 $m\Omega$ + 13.5 μH. At the selected injection frequency of 90 Hz, the typical total reactance between chargers is about 118 $m\Omega$ and the total resistance is about 25 $m\Omega$.

The impedances between all of the distributed chargers on the system are found through simulation in the next section. With the impedance values, the voltage magnitude, and control parameters (m and K), all of the information is known for the next-state equations. The final step in the development of the model is to linearize the equations for the state variables $(\delta_1, \delta_2, \ldots, \delta_n)$.

Approximation 4: Small Angle Approximation. The final approximation is

necessary for the linearization of the system. Eq. 4.8 is non-linear with respect to the state variables, δ. A common solution is to approximate the sinusoidal function as in Eq. 4.10. This approximation is accurate for low values of $\delta_1 - \delta_2$. In the next chapter, we define and determine the proper range of operation of the system such that all of the angles of the distributed chargers are within 60° of the central inverter angle. With this approximation, the power transfer equation reduces to Eq. 4.11.

$$\sin(\delta_1 - \delta_2) \approx (\delta_1 - \delta_2) \tag{4.10}$$

$$P_i = \left|V^2\right| \left(\frac{\delta_i - \delta_1}{X_{i1}} + \frac{\delta_i - \delta_2}{X_{i2}} + \ldots + \frac{\delta_i - \delta_n}{X_{in}} + \frac{\delta_i}{X_{ic}} + \frac{1}{R_{load\,i}}\right) \tag{4.11}$$

Collecting the equations and arranging them in matrix form gives the linearized next-state equations in Eq. 4.12, where $C_{ij} = |V^2| / X_{ij}$. In these equations, the system load is a disturbance input and the power reference command is the control input. In the following section, we will use the state-model to analyze the stability and dynamic performance of the system.

$$\begin{pmatrix} \dot{\delta}_1 \\ \dot{\delta}_2 \\ \vdots \\ \dot{\delta}_n \\ \dot{\omega}_{c\,offset} \end{pmatrix} = \begin{pmatrix} -m\sum_{i\neq 1} C_{1i} & mC_{12} & \dots & mC_{1n} & -1 \\ mC_{21} & -m\sum_{i\neq 2} C_{2i} & \dots & mC_{2n} & -1 \\ \vdots & \vdots & \ddots & \vdots & \vdots \\ mC_{n1} & mC_{n2} & \dots & -m\sum_{i\neq n} C_{ni} & -1 \\ KC_{c1} & KC_{c2} & \dots & KC_{cn} & 0 \end{pmatrix} \begin{pmatrix} \delta_1 \\ \delta_2 \\ \vdots \\ \delta_n \\ \omega_{c\,offset} \end{pmatrix} + \begin{pmatrix} |V^2|/R_{load\,1} \\ |V^2|/R_{load\,2} \\ \vdots \\ |V^2|/R_{load\,n} \\ 0 \end{pmatrix} + \begin{pmatrix} 0 \\ 0 \\ \vdots \\ 0 \\ K \end{pmatrix} P^* \tag{4.12}$$

4.2 Stability and Performance Analysis

The system stability depends on the eigenvalues of the state transition matrix. If all eigenvalues of the state transition matrix are negative and the approximations are valid, the system is asymptotically stable. In an asymptotically stable system, the system will always return to an equilibrium unless one of the inputs causes an approximation to become invalid. One of our approximations can become invalid if the system changes configuration significantly or if the load power or the power reference command causes the small angle approximation to become invalid. If an angle in the system goes above 90° then the system becomes unstable altogether.

In this system, the states are the angles of the distributed chargers relative to the central inverter angle. In equilibrium, all of the angles remain constant with respect to

one another, thus the frequency of the system must be uniform across all distributed chargers. This result proves that for a stable system controlled by droop, the frequency of the system is uniform in steady state.

The impedances between each distributed charger were found through simulation. To find X_{ij}, source i is replaced by a one amp AC-current source at the injection frequency and source j is shorted. All other paths to ground on the system are opened. The magnitude of the voltage across the current sources is measured and recorded. From Ohm's law, the voltage magnitude equals the current magnitude times the impedance magnitude. Since the current magnitude is unity and since we approximate the impedance as purely reactive, the voltage magnitude equals X_{ij}. The filter impedances were not included since the power electronics controller regulates the output voltage directly, thus the output filter dynamics are not part of the droop dynamics, given that they are fast enough. This is further analyzed in the next chapter.

A 33×33 impedance matrix, which includes all mutual impedances among the distributed chargers (one per bus) and the central inverter. Selected values from the impedance matrix are given in Table 4.1. The impedance between chargers on the same phase is around 102 $m\Omega$, which is close approximated impedance value from the previous section. Impedances between chargers on separate phases is larger than that between those on the same phase. It is not infinite since there are line-to-line connected loads on the system. This coupling across phases does not cause a problem in the control because chargers on all three phases are controlled identically with the same system frequency. As more EV are added to the system, the impedance matrix for the existing chargers does not change since the matrix does not consider the overall impedance an inverter sees. This impedance matrix consists of point-to-point impedances, with all other paths on the system open.

Table 4.1: Feeder Impedance Matrix

$X_{ij}(\Omega)$	Inv. A_1	Inv. A_2	Inv. B_1	Inv. B_2	Inv. C_1	Inv. C_2	Central Inv.
Inv. A_1	-	0.102	1.222	1.222	0.812	0.812	0.092
Inv. A_2	0.102	-	1.232	1.232	0.812	0.812	0.102
Inv. B_1	1.222	1.232	-	0.102	0.582	0.582	0.092
Inv. B_2	1.222	1.232	0.102	-	0.592	0.592	0.092
Inv. C_1	0.812	0.812	0.582	0.592	-	0.102	0.082
Inv. C_2	0.812	0.812	0.582	0.592	0.102	-	0.082
Central Inv.	0.092	0.102	0.092	0.092	0.082	0.082	-

With the impedance matrix values, the state transition matrix, given in Eq. 4.12, was found for the system. Figure 4.4 shows the location of the eigenvalues on the complex plane for $m = 0.001$ and $k = 0.005$. There is one pair of complex roots, while the other 31 roots lie on the real axis. All of the roots for the system are in the left-hand plane, which means that they system is asymptotically stable as long as all of the approximations are valid.

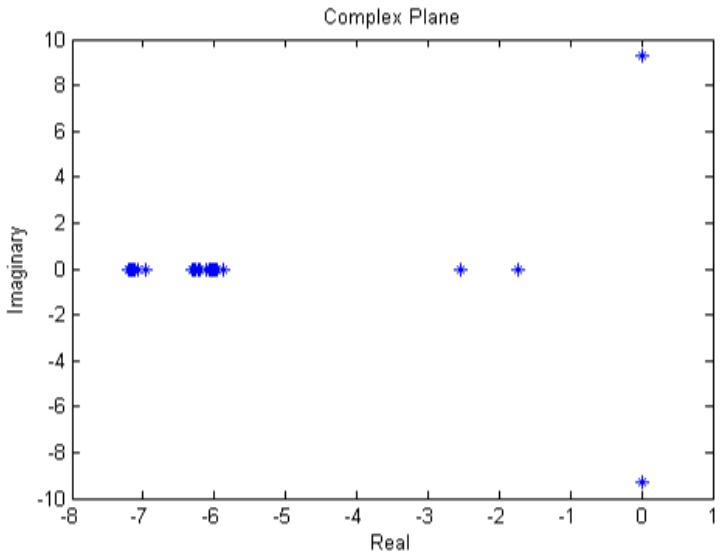

Figure 4.4: Eigenvalues of 32 Inverter System ($m = 0.001$ and $k = 0.005$)

The $n - 1$ real eigenvalues are due to the first-order dynamics of the distributed chargers, as shown previously and pictured again in Figure 4.5. The dynamics of the droop controlled chargers are first order due to the absence of an integrator in the droop controller (an integration exists in the plant). The two complex eigenvalues come from the central inverter controller and plant dynamics, as shown previously and pictured again in Figure 4.6.

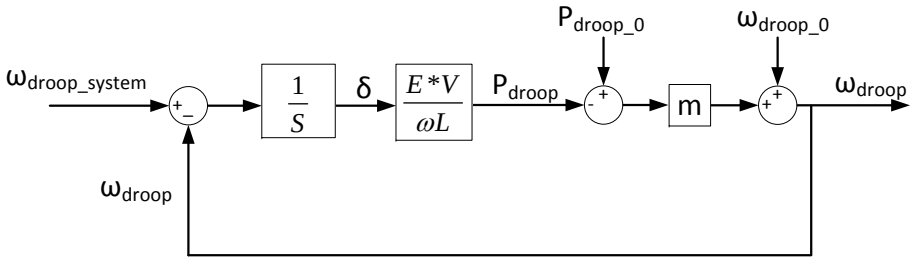

Figure 4.5: Simplified Droop Control Block Diagram

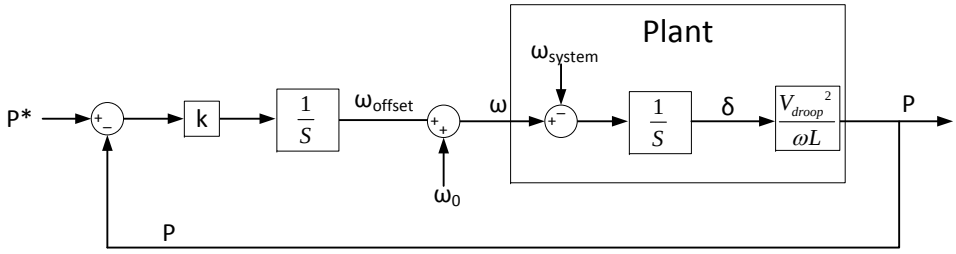

Figure 4.6: Simplified Central Controller Block Diagram

Figure 4.7 shows the migration of the eigenvalues on the complex plane as the droop slope changes. As the droop slope increases, all of the eigenvalues move away from the origin and farther negative on the real axis. Increasing the droop slope increases the speed of the system.

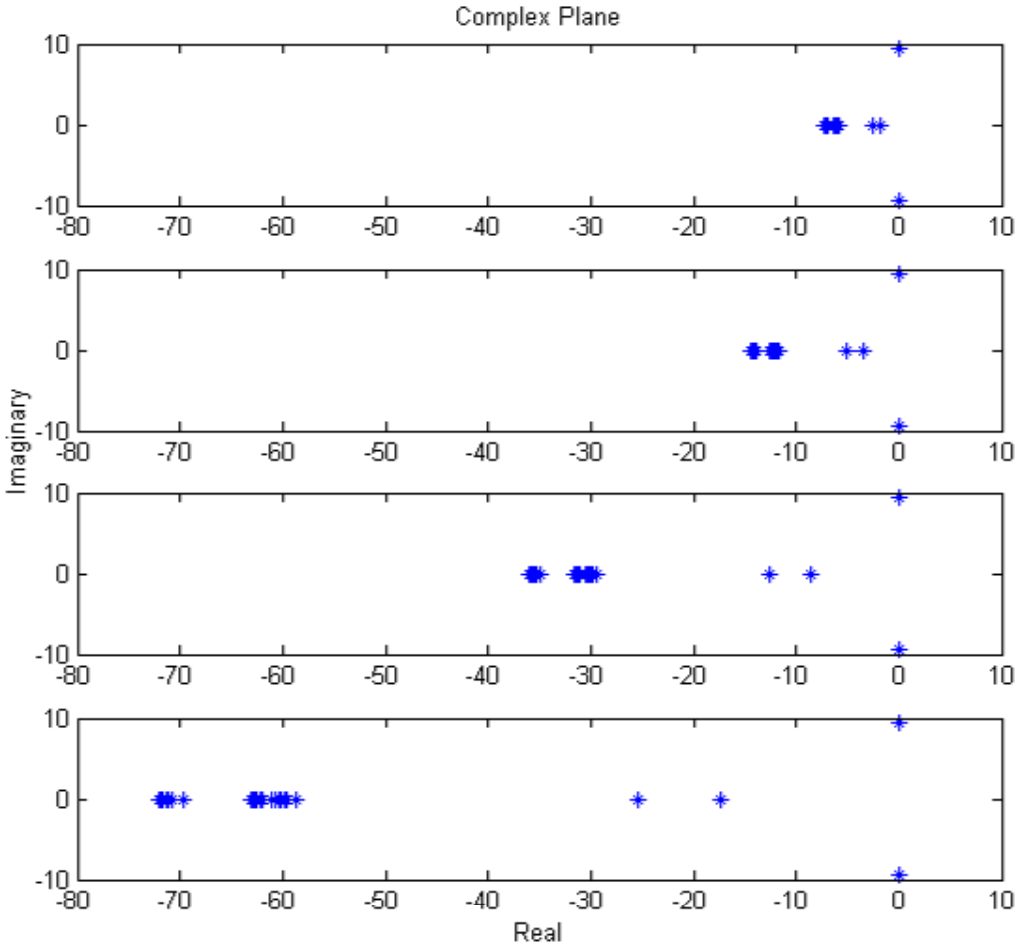

Figure 4.7: Eigenvalues of 32 Inverter System with Increasing m (top to bottom)

The two complex conjugate eigenvalues are the slowest eigenvalues in the system, thus the system performance is dominated by their values. The droop slope should be chosen such that the real component of slowest eigenvalues are placed at the desired response time of the system (in rad/s). In placing the eigenvalues, the speed of the system must not be controlled to be too fast that the signal extraction filter dynamics effect the system dynamics. The speed of the signal extraction filter dynamics provides an upper bound to the speed of the system.

The eigenvalues of the state transition matrix were computed for varying values of the central inverter control variable k. The eigenvalues are shown on the complex plane in Figure 4.8. For the best system performance, k should be selected such that the complex roots have adequate damping without overly slowing down the system response.

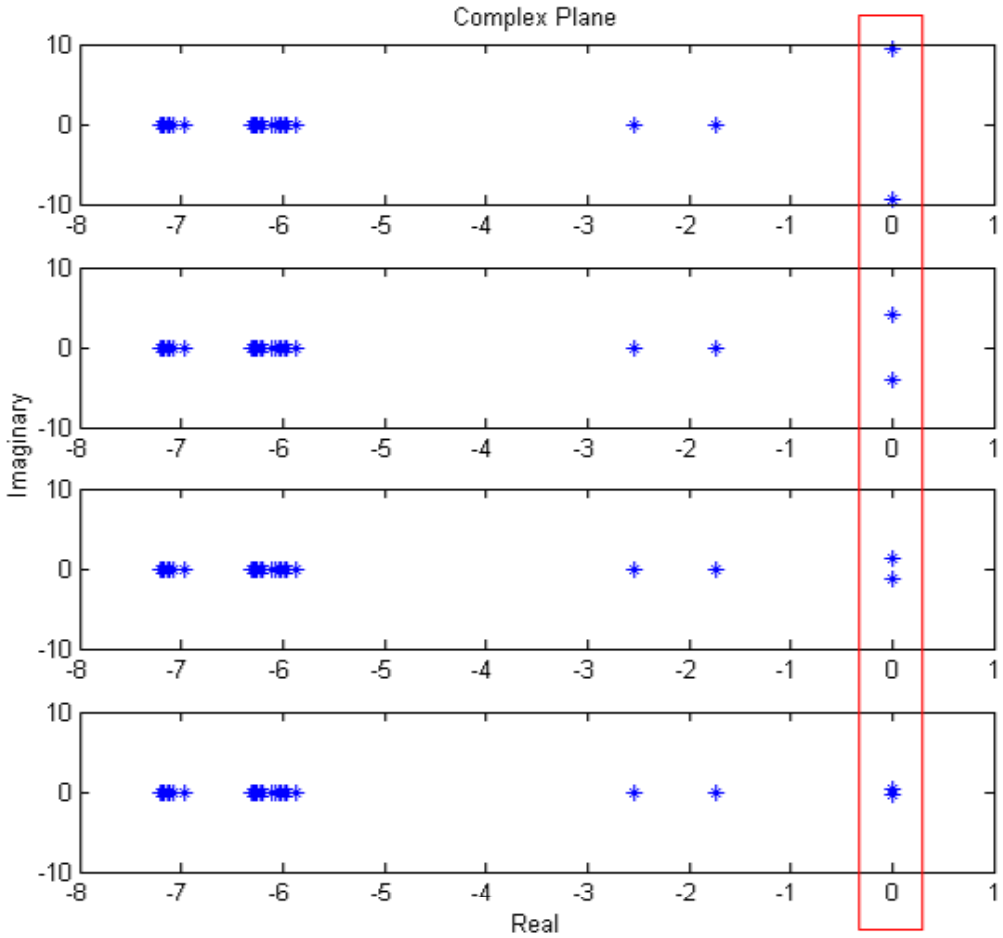

Figure 4.8: Eigenvalues of 32 Inverter System with Decreasing k (top to bottom)

The state transition matrices were found for varying numbers of inverters. The 33x33 impedance matrix was duplicated in order to achieve the appropriate dimensions. This

method assumes that the EV are distributed equally in each case. For example, in the 64 EV case, the model assumes there are two sets of 32 EV that are distributed identically in the system (exactly two at each bus). The eigenvalues of the system for varying numbers of inverters are shown in Figure 4.9.

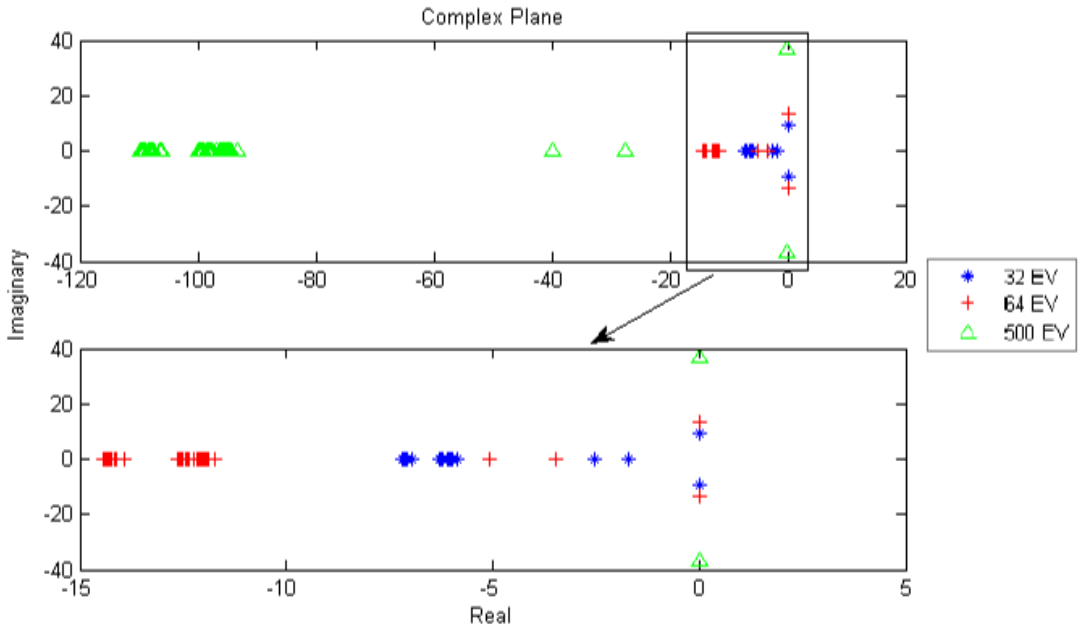

Figure 4.9: Eigenvalues of System with Varying Number of EV

As the number of EV increases, the real eigenvalues move further from the origin, while the imaginary eigenvalues move farther from the real axis. The system can be designed with a central inverter integrator gain term for an average number of EV. The central inverter can update its gain term to adjust the damping based on the number of EV on the system, which the central inverter can determine through a procedure described in the next chapter.

Chapter 5

System Design Considerations

This chapter addresses design challenges and potential issues regarding the implementation of ripple droop control on a distribution feeder.

5.1 Zero-Sequence Signal Injection

One of the main drawbacks of traditional ripple control is the 'spill-over' of the injected signal into the transmission system. Not only does this cause unwanted voltages and currents in the transmission system, the spill-over also causes the ripple signal generator to use more power. Additionally, there may be interference between different ripple signals on separate substations if the two signals are close to the same frequency. With traditional ripple control, in order to filter the injected signal a blocking filter must be placed in series on the line between the substation transformer and the ripple generator as in Figure 5.1. This filter must carry the entire fundamental frequency current during normal operation, thus it is not feasible because the components would be to large and expensive.

We propose to inject the ripple signal in all three lines with no phase shift. In other

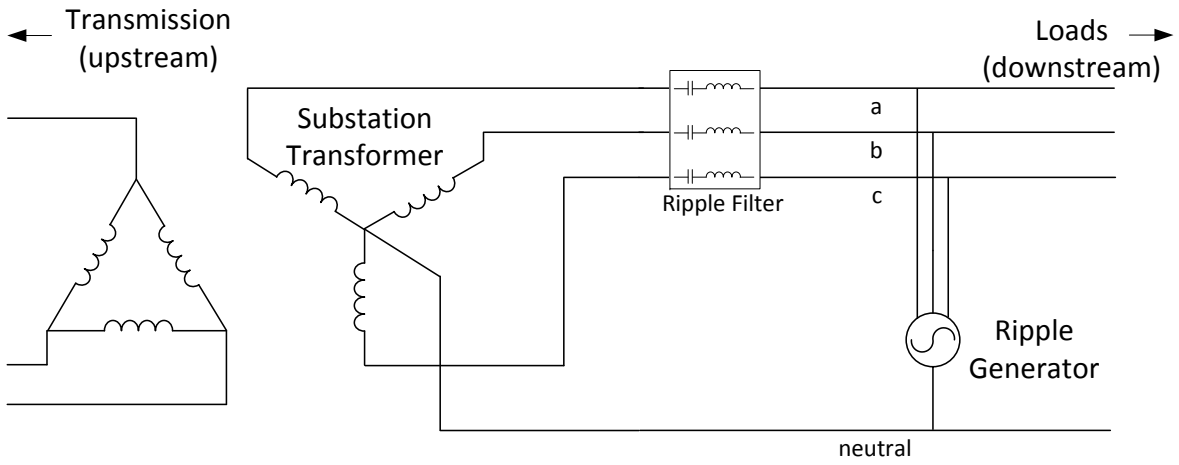

Figure 5.1: Traditional Ripple Voltage with Series Line Filter

words, the ripple signal is a zero-sequence voltage injected into the line. The substation transformer naturally is a short circuit to zero-sequence currents on the wye-neutral connected side (distribution side) since the delta connected side (transmission side) has no neutral wire. As a result, zero sequence voltages can not propagate into transmission. To avoid shorting the zero-sequence ripple generator, a small ripple filter is placed on the neutral wire between the substation transformer and the ripple generator as in Figure 5.2. The advantages of filtering the signal on the neutral wire rather than on the three line wires are that the filter carries much less current, that there is only one filter rather than three, and that the filter does not have to be insulated for high voltage.

The concept of zero-sequence power transfer has been proposed for Distributed Flexible AC Transmission System (D-FACTS) devices [46]. Researchers used zero sequence voltages to transfer power from shunt connected devices to series connected devices which are used to control power flow on transmission lines. In their application, a neutral wire was added to the transmission system to accommodate the power transfer and wye-delta transformers were used to filter the voltages. In our application, the neutral wire is al-

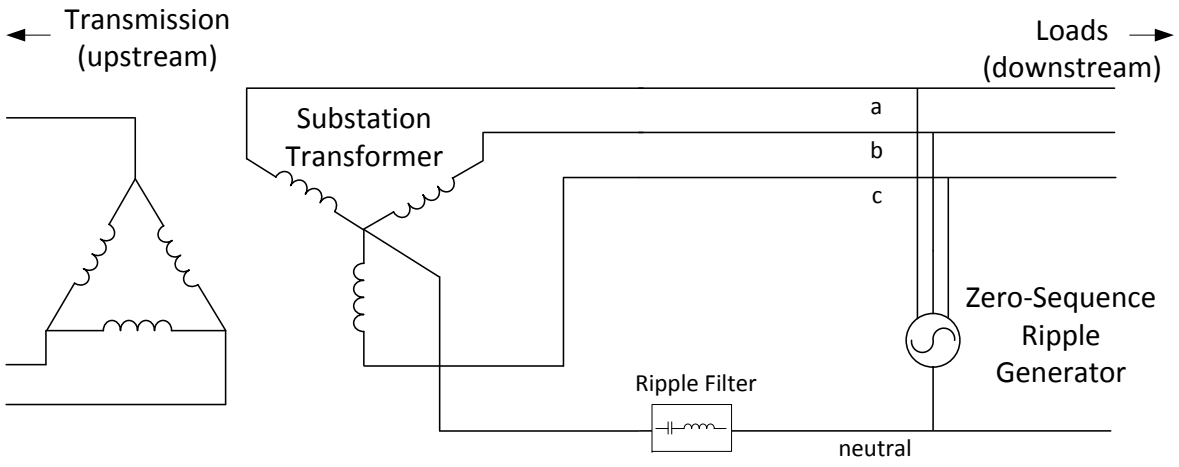

Figure 5.2: Zero-sequence Ripple Voltage with Neutral Wire Filter

ready present in the system. Whereas the devices were series connected in the D-FACTS application, all devices are connected in parallel in the ripple droop application, thus a filter is needed to prevent the wye-grounded transformer from shorting the devices.

The central inverter is controlled to output the injected voltage at zero-sequence. While a more detailed description of the power electronics and control is included in a later section of this chapter, a basic overview of the control is given here. The central inverter consists of 3 single phase converters that can exchange both fundamental, positive-sequence power and zero-sequence power with the system. The inverter controls the injected signal to be zero-sequence by applying identical ripple-voltage commands with respect to neutral to each of the three converters. In effect, the ripple-voltage command is added to fundamental, positive sequence voltage command before being sent to the pulse width modulator (PWM) for each particular converter. This is illustrated on the average model (non-switching model) for the central inverter in Figure 5.3. The signal V^*_{droop} is common to the three converters, while each converter has a unique V^*_{fund} command. Applying the same ripple voltage (V^*_{droop}) to each phase ensures the voltage is

zero sequence at the point of the central inverter and upstream from it.

The distributed EV chargers are single phase, so when they exchange power with the ripple signal they draw or supply power from one of the three chargers of the central inverter. It is desired to have the chargers on the system be treated equally in terms of power sharing regardless of which phase the chargers are connected to. As illustrated in Figure 5.3, this is accomplished in the central inverter control by summing the power from each phase before computing the system frequency. In addition, all three converters are controlled to have the same frequency. Thus every distributed EV charger on the system sees the same injected signal frequency, and every EV charger on the system impacts the system frequency by drawing power from or supplying power to the central inverter converter corresponding the phase to which the charger is connected.

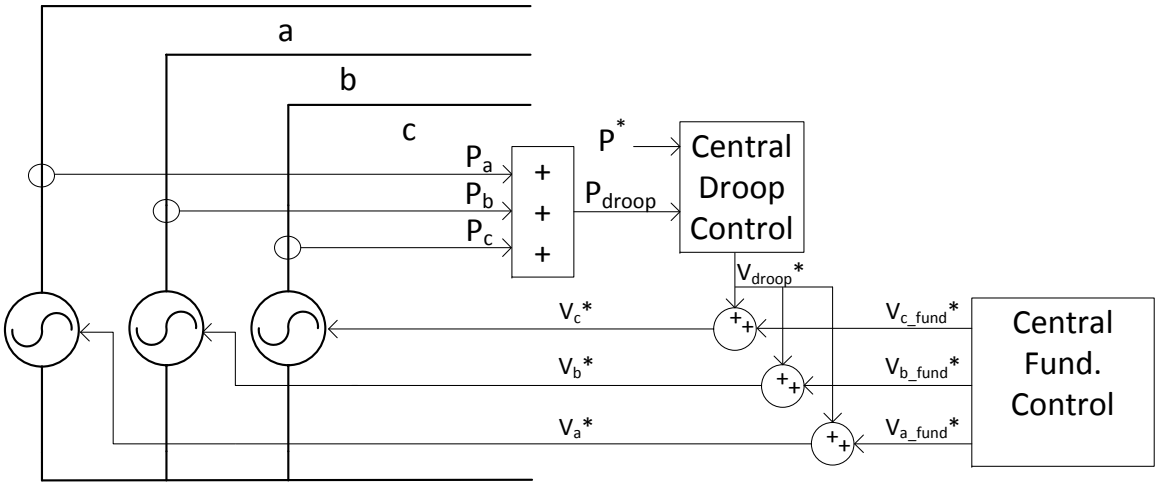

Figure 5.3: Central Inverter Control for Zero-Sequence Signal Injection

A simple example of the phase-independent droop control is given here. Consider a system as in Figure 5.4, where there are 3 distributed chargers on phase A, 2 on phase B,

and one on phase C. In this example, the central inverter adjusts its frequency such that it injects a total of 200 W into the ripple signal. Since the frequency is uniform across the system and since the distributed chargers have the same droop slope, the distributed chargers each equally draw 33.3 W. The power from each central inverter converter is not equal in this case since the phases are not balanced. The results from this simulation are pictured in Figure 5.5. It can be seen that the distributed chargers converge on a single value while the central converters remain unbalanced.

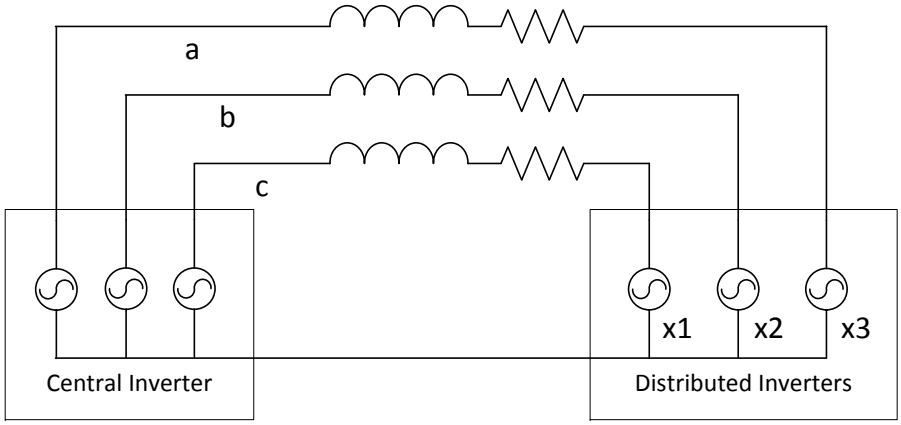

Figure 5.4: Schematic for Control of Unbalanced EV Chargers with Ripple Droop

For some applications, it may be beneficial to control the power on each phase of the system to a specific quantity. This is possible with ripple droop control. The control given in Figure 5.3 would be modified to include three central droop controllers, one for the power input from each phase. This system could accommodate three independent power reference commands. This approach could be used to balance the system, to relieve a particular phase from a high loading, or to regulate the voltage on the system. The downside to this approach is that the injected signals are not uniform across the system

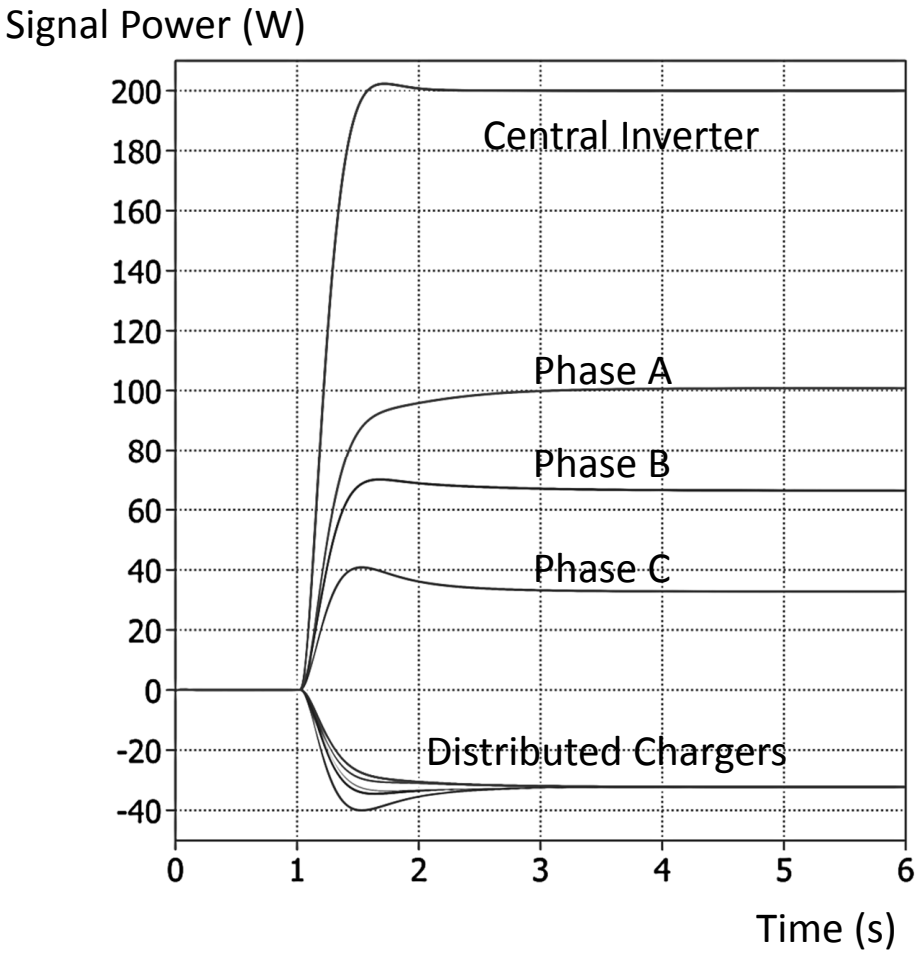

Figure 5.5: Results for Control of Unbalanced EV Chargers with Ripple Droop

and zero-sequence injection is not possible. A series line current filtering strategy similar to that in Figure 5.1 would be necessary.

5.2 Leakage Power

A potential issue with ripple droop control for the application we are considering is what we have termed 'leakage power'. In this section, the problem is examined and

quantified through analysis and simulation. Additionally, a method for the central inverter to determine the quantity of leakage power on the system in real-time is presented.

5.2.1 Leakage Power Overview

Ideally, the power injected into the ripple signal from the central inverter equals the sum of the power received by the distributed inverters, as in Figure 5.6 and Eq. 5.1.

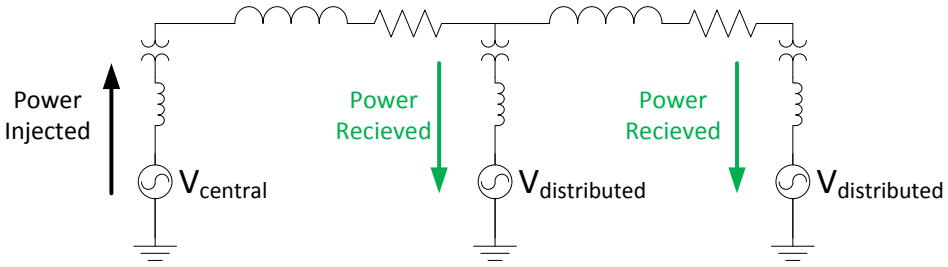

Figure 5.6: Ideal Conservation of Power in Ripple Droop Control

$$P_{injected} = \sum P_{received} \tag{5.1}$$

This conservation of power is important because the quantity of power transferred in the injected signal is used to control the quantity of fundamental frequency power for each distributed charger to supply. The total power injected into the system from the distributed chargers at fundamental frequency is is proportional to the power in the ripple signal as in Eq. 5.2.

$$P_{fund} = (\frac{P_{fund}}{P_{ripple}} Raio) \times \sum P_{received} \tag{5.2}$$

The central inverter can measure the amount of power it transfers into the signal, however it is not able to measure the power received by the distributed chargers. The problem is that there is not conservation of power. Not all of the power injected by the central inverter goes to the distributed chargers. Some of the power is lost in the distribution line and some of the power is lost across the loads in the system. This non-ideal scenario is illustrated in Figure 5.7 and Eq. 5.3. In the figure all of the loads on the feeder are grouped together as $Z_{load\ aggregate}$. The power lost in the distribution line is termed 'line leakage' and the power lost through the loads on the system is termed 'load leakage'. The sum of these two quantities is the total leakage power.

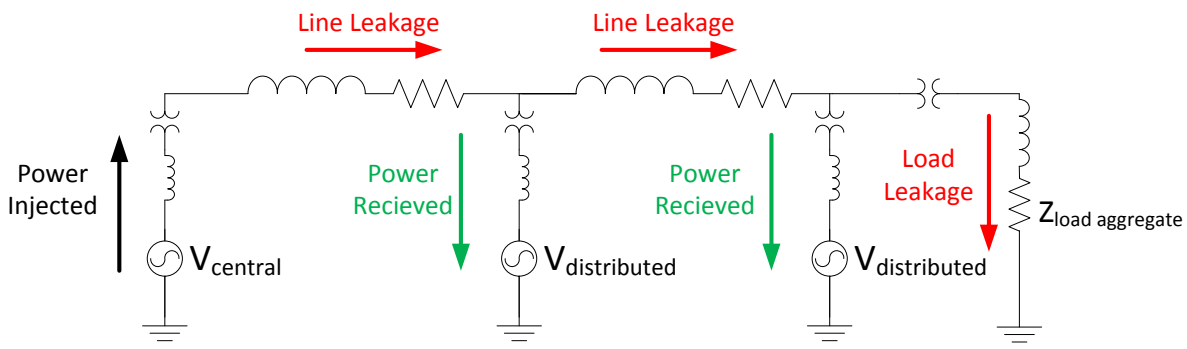

Figure 5.7: Division of Injected Power in Ripple Droop Control

$$P_{injected} = \sum (P_{received} + P_{line} + P_{load}) \tag{5.3}$$

The line leakage comes from the I^2R losses on the distribution line. The load leakage comes from the power dissipated into loads on the system due to the presence of the ripple voltage. Consider the simple case of a resistive load. The power it consumes at fundamental frequency is the square of the voltage divided by the resistance. The power

consumed due to the ripple voltage (load leakage) is found the same way. Both the load leakage and the fundamental load power are inversely proportional to the load resistance. As the fundamental load power increases, not only does the load leakage increase, the line leakage also increases because the current must travel through the line before it is dissipated into the load. For active or non-linear loads, the relationship is more complex and is not examined here. The purpose of this analysis is to get a general idea of where the sources of leakage come from.

To determine the exact relationships between the leakage power and system parameters, several simulations were run on the IEEE 13 Bus Feeder, illustrated in Figure 5.8. In the simulations, one distributed charger was placed on each phase and on each bus in the system, totaling 32 chargers. The injected signal voltage magnitude was set at 3% of nominal voltage, and the injected signal frequency was set at 90 Hz. An average model was used for the power electronics converters and the fundamental voltage was not included in the simulation. All loads on the feeder were assumed to be constant impedance loads.

The results shown in this subsection illustrate the leakage power as functions of dynamically changing variables (ripple power injected by the central inverter, load power, and number of distributed EV chargers). These relationships are used in the next subsection for the real-time determination of the leakage power. All of the data points in the plots in this section are for quantities of power that lie within the stable signal range. The signal range, along with the selection of the ripple voltage magnitude and the ripple frequency, are examined in detail in the 'Signal Attributes' section later in this chapter. In short, the signal range is defined as the range of power for which under any operating condition (number of EV or load on the feeder) each distributed on the system can absorb or supply the commanded power with an angle within 60° of the central inverter angle.

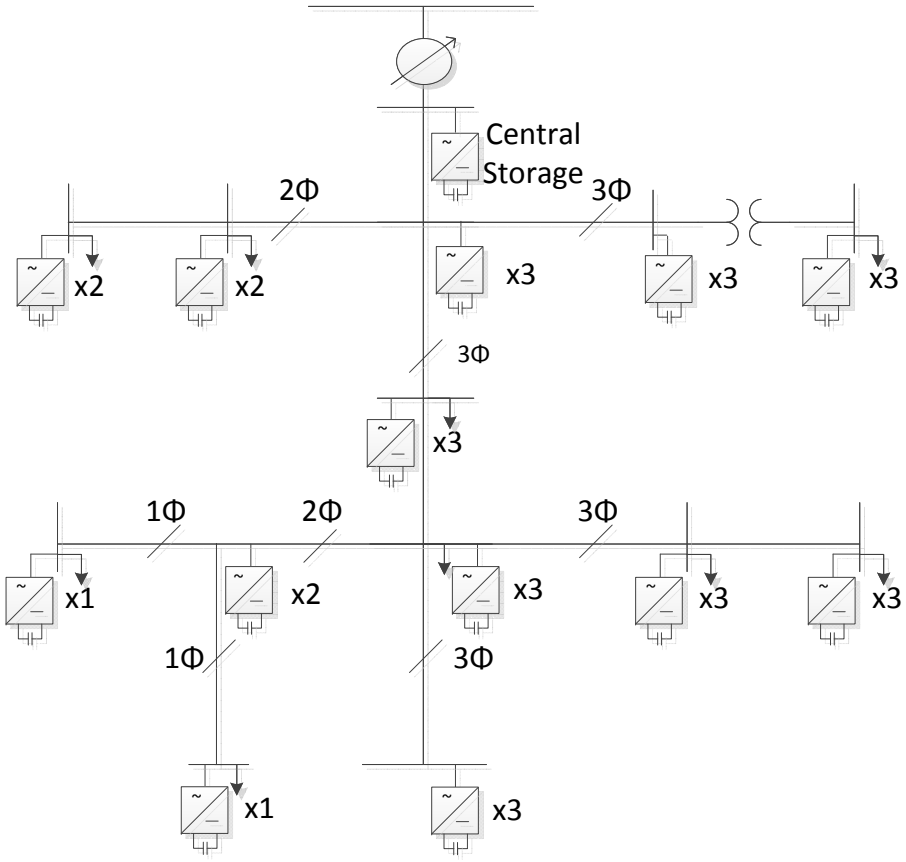

Figure 5.8: IEEE 13 Bus Feeder with One EV Charger per Phase per Bus

In the first set of simulations, we find the power received and leakage power as a function of the injected signal power. The power received is simply the sum of the power received by each distributed EV charger. The leakage power is the difference between the power injected (by the central inverter) and the power received. Ideally, if there were no leakage, the received power would equal the power injected by the central inverter and the plot would be linear with a slope of one. Negative quantities for the power injected indicate that the central inverter is drawing power from the injected signal. Likewise, negative quantities for the power received indicate that the distributed chargers

are injecting power back into the signal. The capability for both directions of power flow is necessary in order to control the distributed chargers to source as well as sink power.

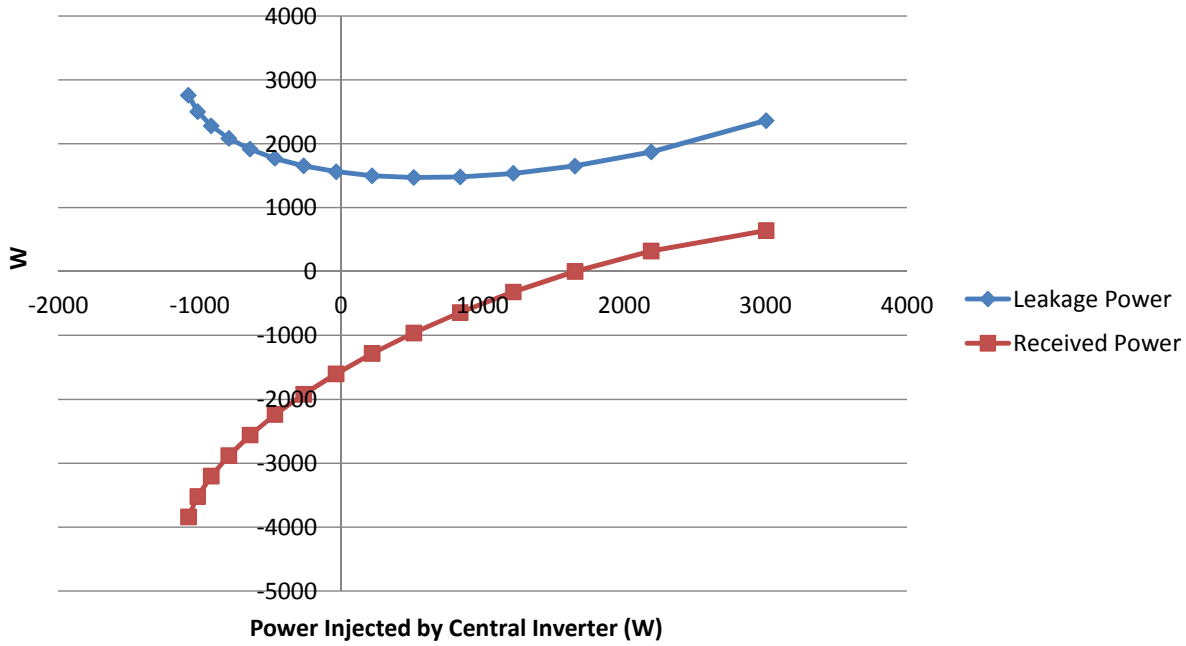

Figure 5.9: Leakage Power and Power Received vs Power Injected

The leakage power is not zero whenever the injected signal power is zero because the ripple voltage remains present on the line, thus there is power lost through the loads on the system. When the injected signal power is zero, the leakage power is supplied by the distributed chargers. This is the reason for the negative y-axis intercept for the received power curve.

To illustrate the effects of variations in the load on the system, the previous simulation was run for the same system with full rated, half rated, and zero load connected. The leakage curves for these three scenarios are plotted in Figure 5.10.

Variations in the system load affect the offset of the power received vs power injected

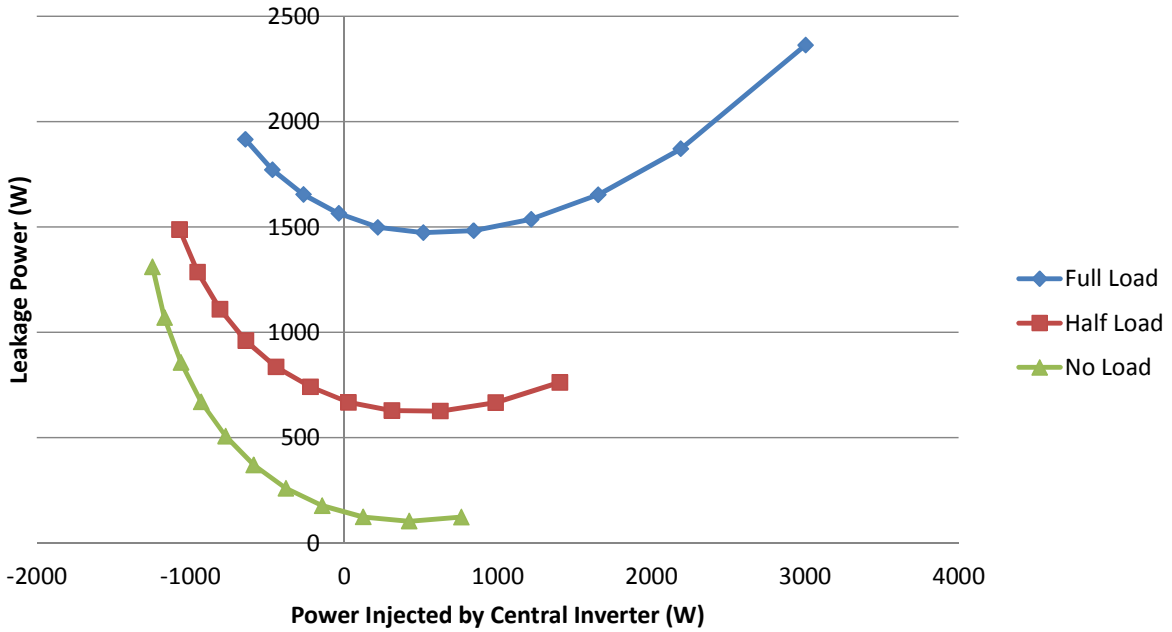

Figure 5.10: Leakage Power vs Power Injected as the System Load Varies

curves. The power received versus power injected curves for the cases of full load, half load, no load, and ideal (no line leakage) are plotted in Figure 5.11. These curves contain the critical information for the central controller since it must know the amount of power necessary to inject into the ripple signal to correspond to a particular quantity of power received. The power received quantity is the one which is used by the distributed chargers to determine the amount of fundamental power to exchange with the grid.

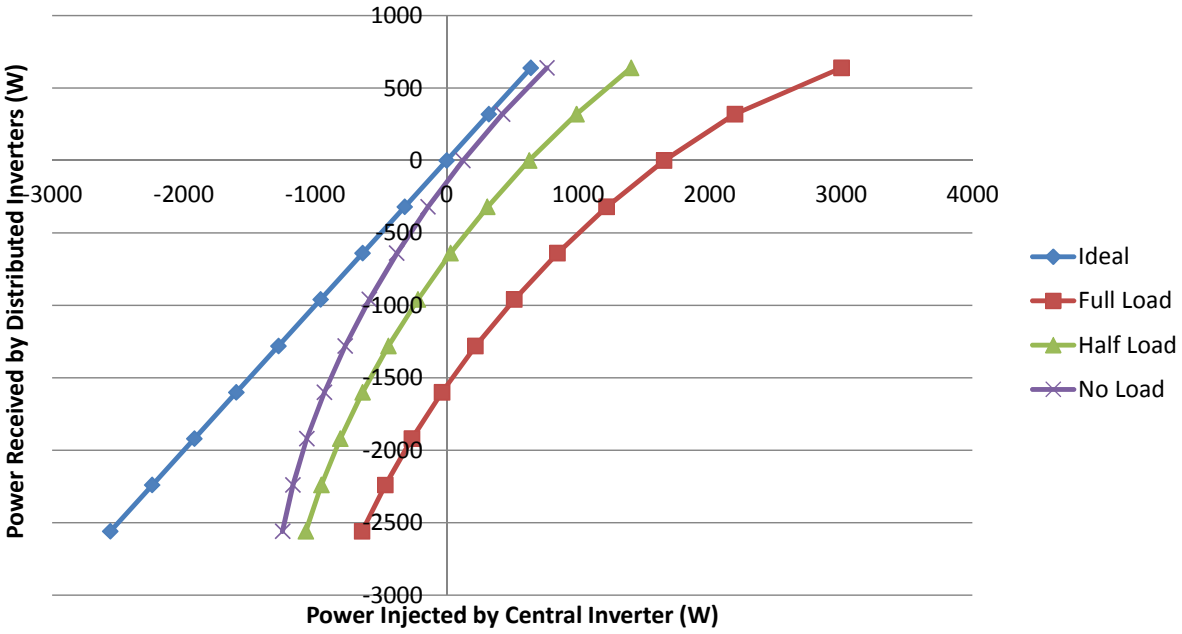

Figure 5.11: Power Received vs Power Injected as the System Load Varies

Lastly, the simulation was run for full load on the system while changing the number of distributed EV chargers. The results are compared to the nominal number of EV chargers in Figure 5.12. The results show that the leakage power does not vary much as the number of EV varies. This result is to be expected since there is no more current through the line or load as the number of distributed chargers changes. This is useful since the central inverter only needs to compensate for changes in the load when determining the leakage on the system. Figure 5.13 shows the power received versus power injected curves for varying quantities of EV on the system, showing that the number of EV chargers does not affect the leakage significantly.

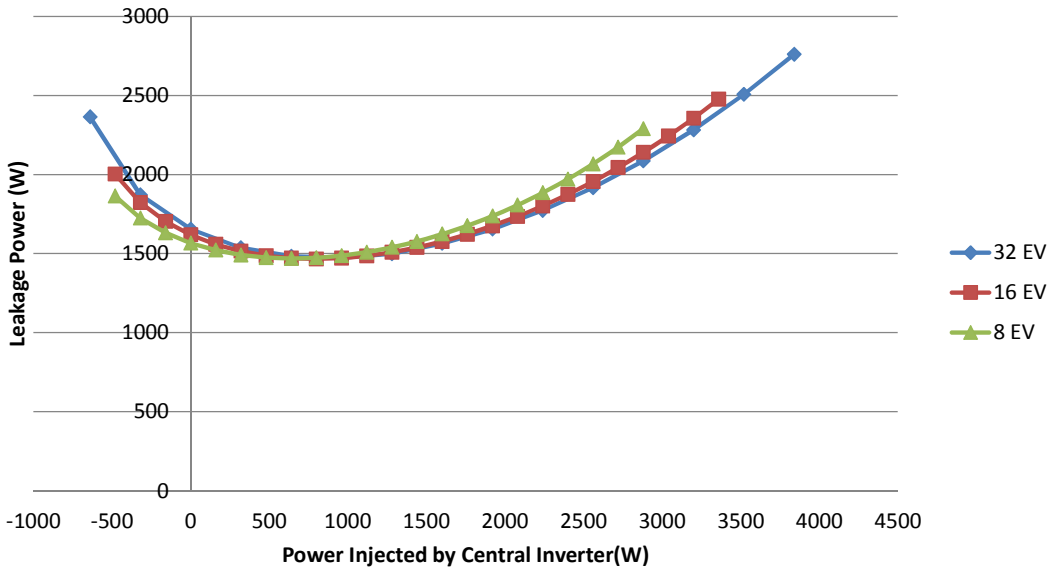

Figure 5.12: Leakage Power vs Power Injected as the Number of EV Varies

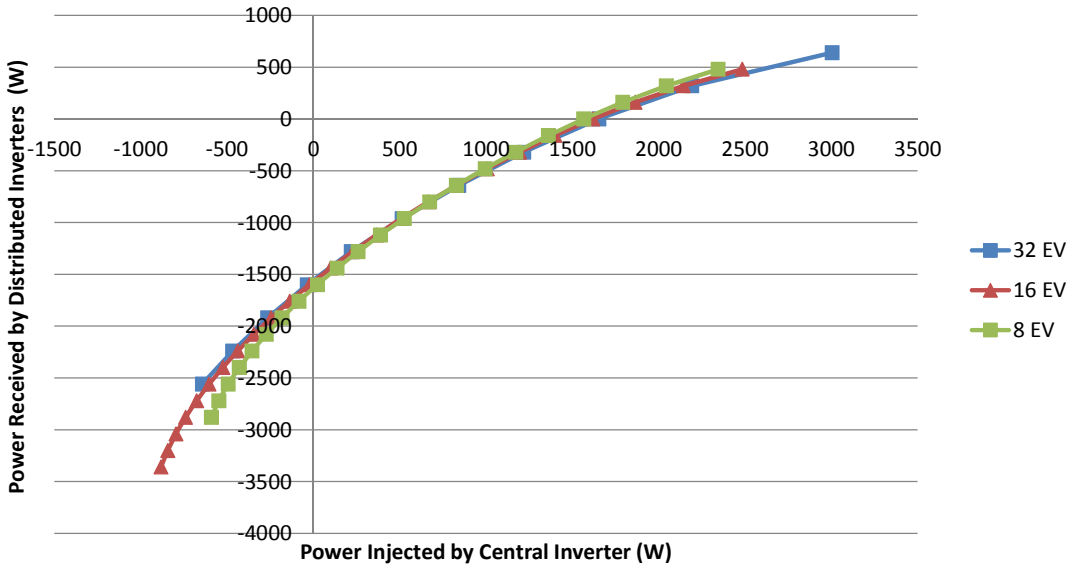

Figure 5.13: Power Received vs Power Injected as the Number of EV Varies

5.2.2 Received Power Identification Technique

In order to command a specific quantity of power from the aggregate of the distributed storage, it is necessary for the central inverter controller to know the amount of power that is received by the distributed inverters from the injected signal. This information is contained in the curves in Figure 5.11. The central inverter controller can measure the quantity of power it injects into the signal, yet it can not measure directly the amount of power that is received by distributed inverters. However, the central inverter does know the system frequency, which is uniform across the system in steady state, and from the system frequency it can determine the power received by each each distributed inverter. The final piece of information the central inverter needs to know is the number of distributed EV chargers on the system. If the central inverter knows the power received per distributed charger and the number of distributed chargers on the system, it can calculate the curves from Figure 5.11.

It was shown previously that these curves vary for the amount of load on the system, but do not vary as the number of EV chargers varies. Therefore, the central inverter must store in a lookup table a family of these curves corresponding to the magnitudes of the system load.

A method for estimating the number of distributed EV chargers on the system is described next. With this information, the central inverter can determine the power received versus power injected curves. This estimation procedure can be done quickly (two time constants), does not interrupt the normal operation of ripple droop, and can be performed by the central inverter using only quantities locally measurable to the central inverter controller.

Since the system frequency is uniform and the received power per inverter is a function

of the system frequency, the total received power received is equal to the power received by each charger times the number of chargers, as in Eq. 5.4.

$$P_{received\,total} = P_{received\,charger} \times \#EV \tag{5.4}$$

The central controller can determine the power received by each charger using the frequency of the injected signal and the droop equation used in the controller of each distributed charger, as in Eq. 5.5.

$$P_{received\,charger} = \frac{\omega_0 - \omega_{system}}{m} \tag{5.5}$$

Thus, the central controller simply needs the number of EV on the system in order to know the amount of power received. The number of EV on the system can be determined by introducing a small disturbance in the system frequency and measuring the resulting change of power drawn from the central inverter. From an equilibrium, the central inverter can alter the system frequency by $\Delta\omega$ to increase the power received per distributed inverter by $\frac{-\Delta\omega}{m}$, as in Eq. 5.6.

$$\Delta P_{received\,charger} = \frac{-\Delta\omega}{m} \tag{5.6}$$

This will result in an increase in the power drawn from the central inverter equal to the unit change in power times the number of EV on the system, plus the resultant change in line leakage, as in Eq. 5.7. The unit change in line leakage is equal to the unit change in the central power injected times the derivative of the line leakage with respect to the central power injected, as in Eq. 5.8. Substituting Eq. 5.8 into Eq. 5.7 and rearranging,

the central inverter controller can identify the number of EV on the system by Eq. 5.9.

$$\Delta P_{injected\ central} = \Delta P_{received\ charger} \times \#EV + \Delta P_{line\ leakage} \tag{5.7}$$

$$\Delta P_{line\ leakage} = \Delta P_{injected\ central} \times \frac{\partial P_{line\ leakage}}{\partial P_{injected\ central}} \tag{5.8}$$

$$\#EV = \frac{\Delta P_{injected\ central} * (1 - \frac{\partial P_{line\ leakage}}{\partial P_{injected\ central}})}{\Delta P_{received\ charger}} \tag{5.9}$$

The derivative of line leakage with respect to injected power is a quantity that must be estimated off-line, since the central inverter has no way to measure the line leakage power, unless it already knows the number of distributed EV chargers on the system. The line leakage derivative for the system in this work is pictured in Figure 5.14. From the plot, one can see that the line leakage derivative does not depend on the system load. Included in the plot is third order polynomial curve fitted to the data points.

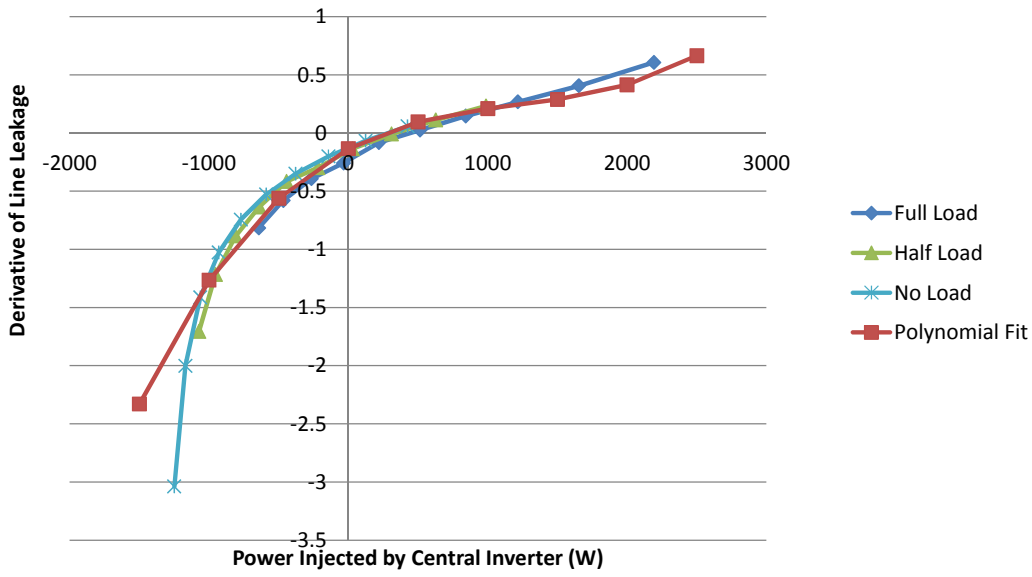

Figure 5.14: Line Leakage Derivative versus Central Power under Varying Loads

The leakage identification procedure was performed on the model of the feeder in order to verify its operation. Figure 5.15 shows the perturb method for the system operating at full load and central power at 1.5 kW.

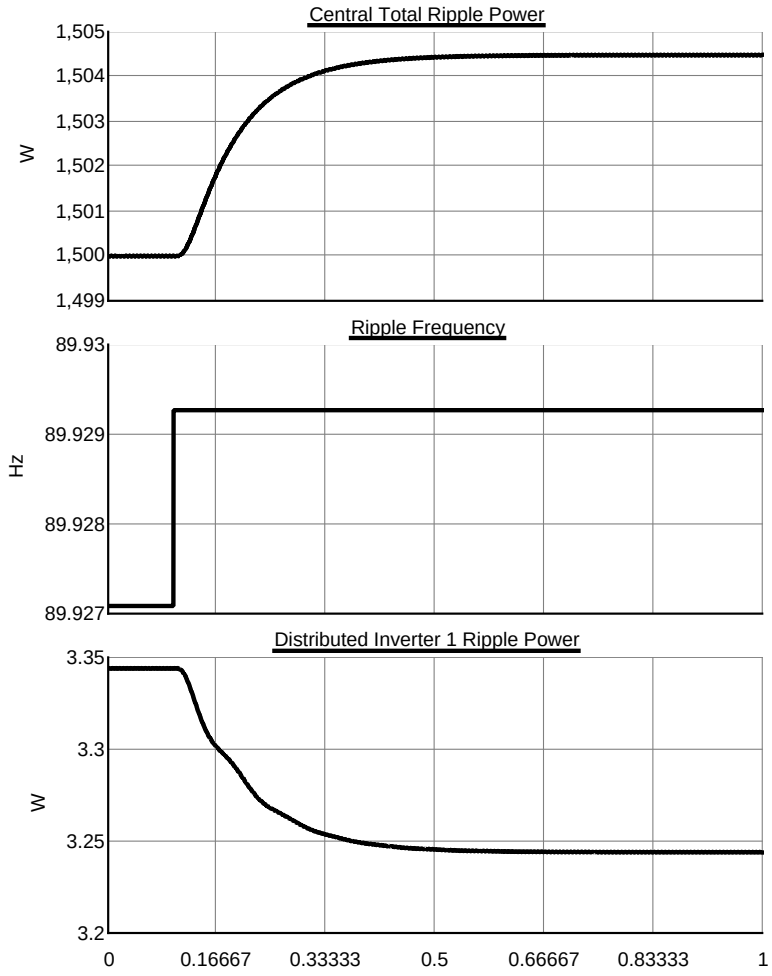

Figure 5.15: Perturbation of Ripple Frequency to for Leakage Estimation

The top two plots show the central inverter power and ripple frequency. The bottom plot shows the response from a distributed inverter to the frequency step change. The

ripple frequency is increased by $m/10$ in order to decrease the distributed inverter power by 0.1 W. The quantity of interest in this test is the change in power from the central inverter, which is 4.5 W in this case. Using Eq. 5.9 and the off-line knowledge of the derivative of the line leakage (0.288 at $P_{injected\ central} = 1,500$), the estimated quantity of EV is 32.04. The actual number on the system is 32 for this case. There can not be fractional numbers of EV chargers on the system, but for estimation purposes, rounding will not lead to a more accurate answer. Since the line leakage derivative is not an exact quantity, there is no need to round to the nearest whole charger for accuracy.

This process was repeated for varying values of central inverter power and at varying system loads. The results for the leakage identification tests are plotted against the actual measured quantities for the feeder. The power received versus power injected curves are plotted in Figure 5.16.

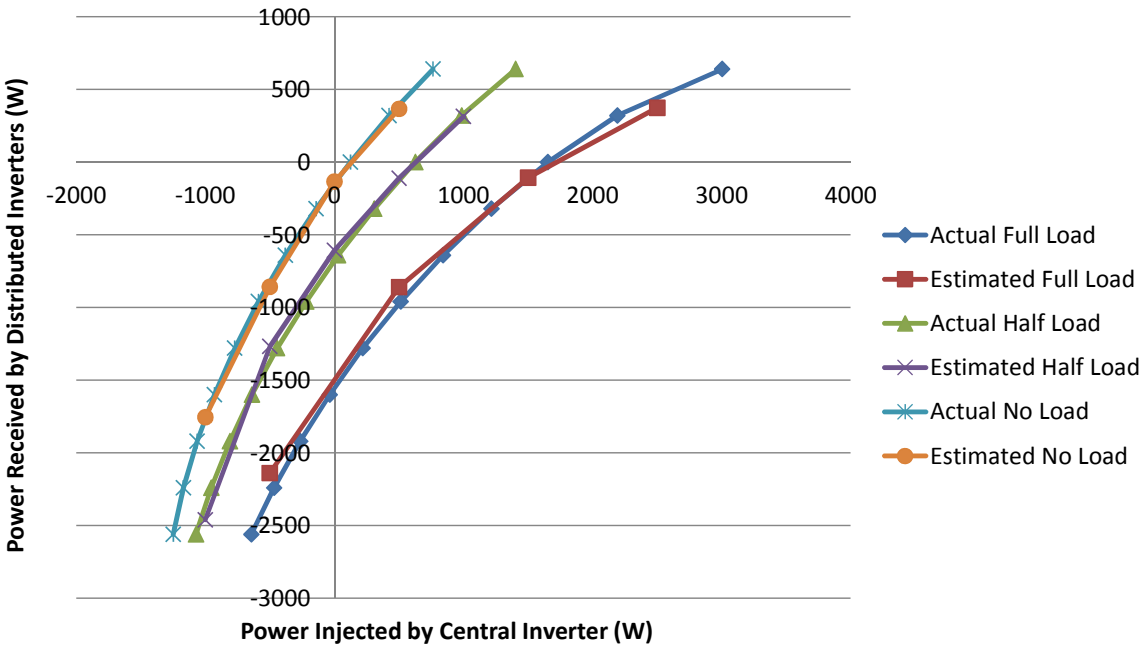

Figure 5.16: Power Received versus Power Injected Actual and Estimated Values

The amount of leakage power can be computed by the central inverter by Eq. 5.10, although the central inverter does not need to compute this value for operation. However, it is interesting to see the leakage estimation compared with the actual leakage values to verify the leakage identification procedure. The actual leakage values and the estimated values are plotted in Figure 5.17.

$$P_{leakage} = P_{injected\ central} - P_{received\ charger} \times \#EV \tag{5.10}$$

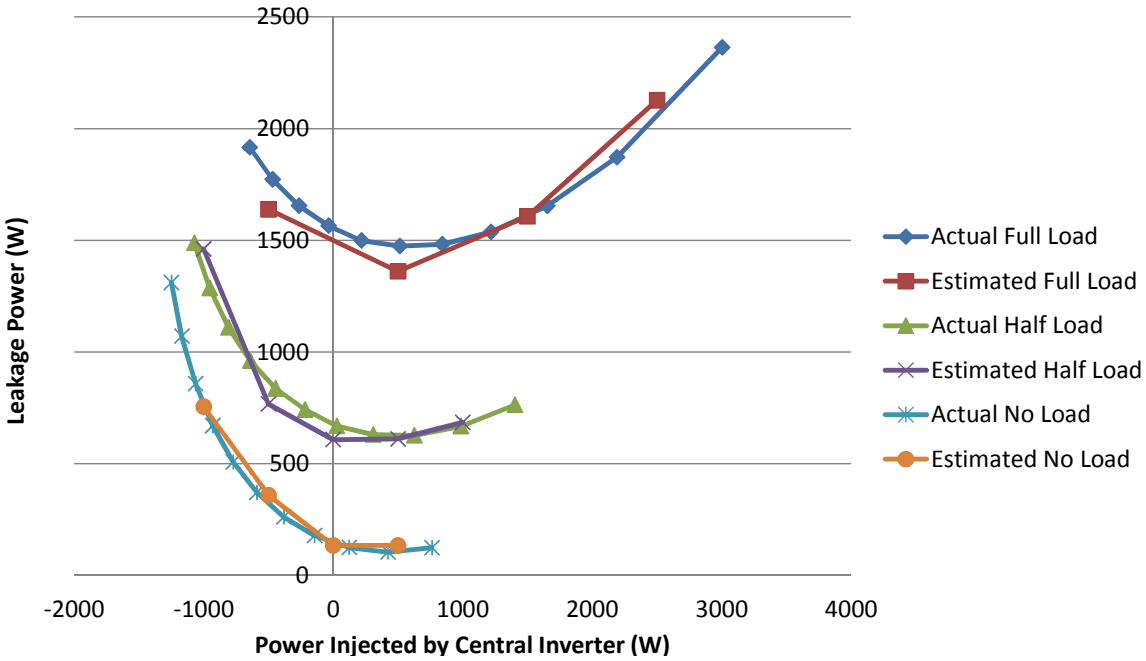

Figure 5.17: Leakage Power versus Power Injected Actual and Estimated Values

In summary, the leakage power is a function of the power injected in the signal, the system load, and the number of EV. The central inverter controller can perform the identification procedure periodically and record a look-up table of leakage power

quantities based on the signal power, system load, and number of EV. The central inverter can measure the system load through a CT since it is located upstream of all loads on the system. The look-up table would contain families of curves which are periodically updated. The central inverter controller can compensate for the expected leakage value for a given system state in order to inject the appropriate amount of power into the signal to get the desired quantity of power received.

As EV are added and removed from the system, the leakage power does not change as long as the distribution of EV throughout the system remains relatively constant. As EV are added or removed, the signal power remains fixed and through droop control, all of the EV chargers on the system adjust in order to equally share the power.

A additional benefits of the identification procedure come from the knowledge about the number of EV connected to the system. This data can be used either in real-time or off-line for control and planning. For example, a limit could be imposed on the quantity of power requested from the aggregate storage based on the number of EV on the system.

5.3 Signal Attributes: Voltage, Frequency and Power

In this section, the selection of the frequency, voltage, and power of the injected signal are presented. First, the selection of the signal frequency is discussed. It was found that in order to have a ripple voltage profile on the feeder somewhat close to uniform, the ripple frequency must be close to the fundamental frequency. This is because each feeder is designed with an X/R ratio and with capacitor banks such that the fundamental frequency voltage is within $\pm 5\%$ of nominal. Figure 5.18 shows the voltage profile on the 13 bus feeder for a various signal frequencies. The distance of the bus from the substation is shown on the x-axis.

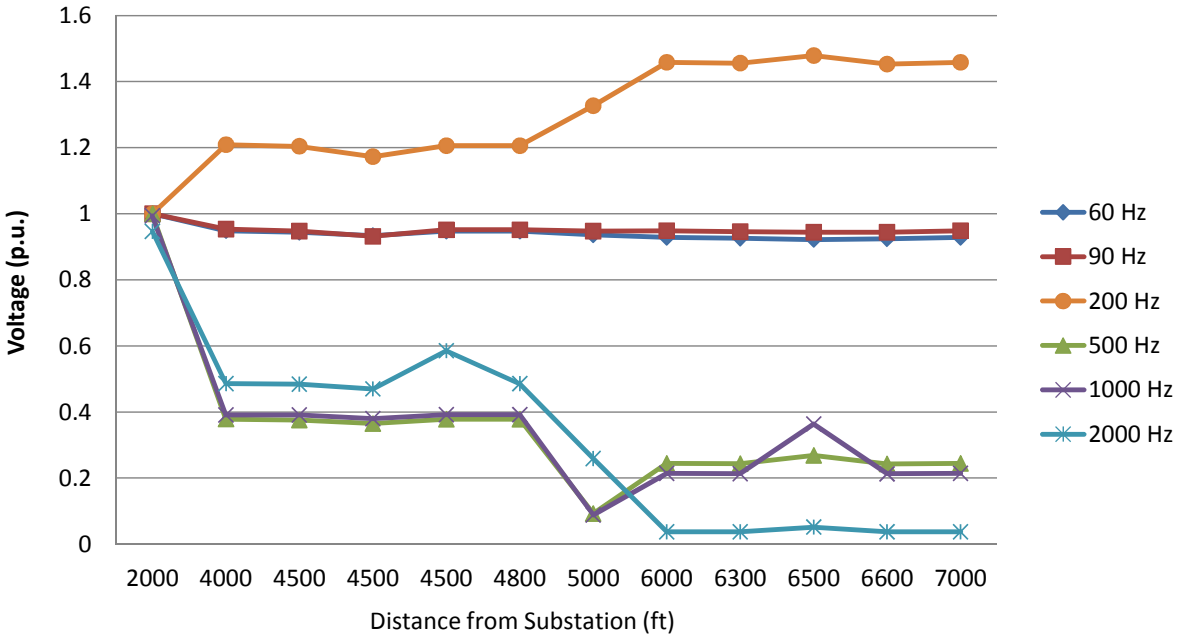

Figure 5.18: Feeder Voltage Profile for Varying Frequencies

It is clear from the voltage profile chart that as the signal frequency increases far from 60 Hz, the voltage profile is not consistent. The rise in voltage in the 200 Hz signal is caused by the increased reactive power injected by the capacitor bank. The reactive power injected is proportional to the frequency of the voltage. A further increase in signal frequency causes the reactive power injection to be too high, leading to high negative reactive current and a voltage collapse. Additionally, as the frequency increases, the inductance on the line increases causing the voltage to be more sensitive to reactive power.

The signal frequency of 90 Hz is selected for our application. Another frequency close to 60 Hz would be acceptable as well. Selecting a frequency close to fundamental frequency is necessary, however it causes several problems that will be addressed in full in the 'Power Electronics' section. In short, by selecting a frequency close to fundamental, filtering

the ripple voltage and frequency from the overall measurements requires higher order or lower bandwidth filters which are more selective. These filters have slower response times than less selective filters, thus the overall system response time must be decreased. Additionally, the control becomes rather complex for regulating both frequencies while achieving a fast current controller.

In selecting the voltage and power levels, the goal is to maximize the redundancy of the signal and lessen its susceptibility to noise. The quantities in the signal which are measured by each inverter are the signal voltage and current. These are the quantities that we wish to increase in order to increase the signal redundancy. Both of these quantities must be filtered from the signals which contain the fundamental frequency quantities. Furthermore, these signals will contain random noise and harmonics of the fundamental frequency.

The voltage of the injected signal is limited by the IEEE 519 Standard which outlines limitations for harmonic voltages and currents [31]. The standard gives a maximum value of 5% for the total harmonic distortion (THD) of the voltage on any point of the feeder. The standard goes on to limit the maximum voltage magnitude of any individual frequency other than fundamental to 3% of fundamental frequency voltage. This is the limitation that determines the magnitude of the injected voltage. It is desirable to choose the maximum voltage within the allowable range not only to increase the voltage signal to noise ratio, but to increase the the power which can be transferred in the signal, which is proportional to the current magnitude.

Unlike the frequency, the voltage magnitude does not affect the voltage profile of the signal on a per unit basis. The normalized voltage profiles for the fundamental signal and the ripple signal with 3% magnitude are nearly identical and are plotted in Figure 5.19.

In selecting the power level for the ripple signal, we wish to understand what is

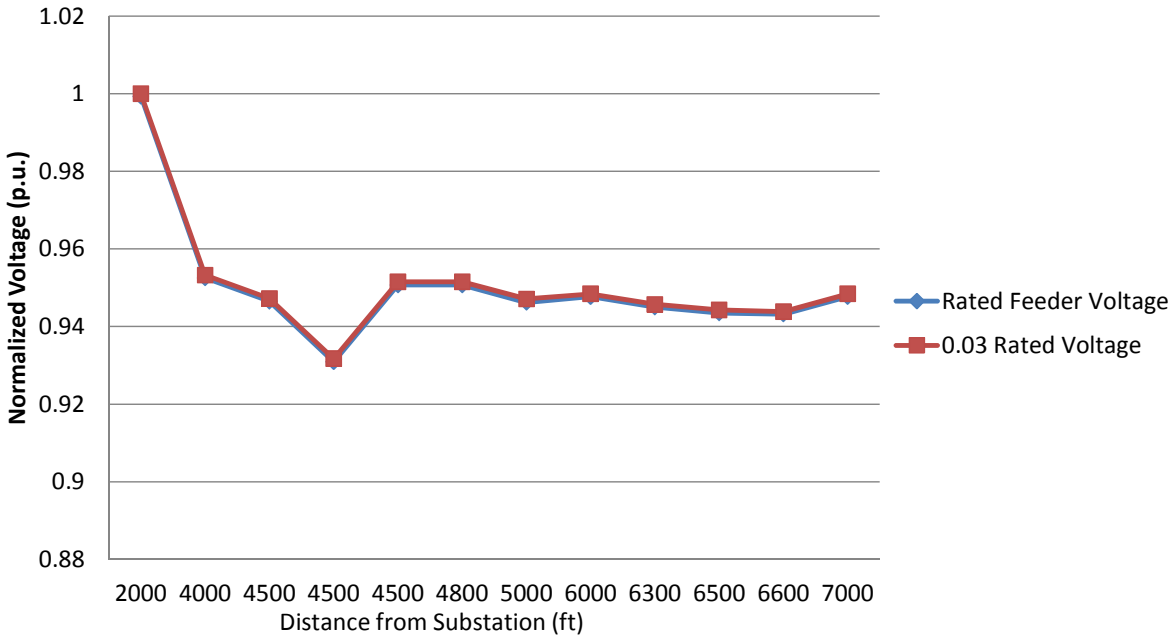

Figure 5.19: Feeder Voltage Profile for Fundamental and Ripple Magnitudes

the maximum level of power that can be transferred in a stable operating manner. The theoretical maximum power that can be transferred in the injected signal is governed by the fundamental equation for the amount of power that can be transferred between two voltage sources separated by an inductance, (Eq. 5.11).

$$P = \frac{|V|^2}{X} \sin \delta \tag{5.11}$$

In Eq. 5.11, δ is the angle between the two voltage sources. It is necessary for this angle to remain below 90° for the stability of the system in steady-state since an increase beyond 90° causes the power to drop and the negative feedback control becomes positive feedback. A safe operating margin between the maximum angle in the system and 90° is beneficial for the stability of the system in the case of disturbances or transients. We will consider 60° the highest allowable operating angle for the following analysis, leaving

a 30° margin. The system model and stability analysis, it was assumed that the angle of the system does not exceed the safe margin. In the analysis of this section, we will select system parameters such that the margin is not exceeded.

The signal range is defined as the range of power for which each distributed inverter on the system can inject or absorb without a single inverter exceeding the 60° operating margin.

Figure 5.20 shows the maximum angle on a simulated system with 32 distributed charger as a function of the power received by each distributed charger. These angles are found with consideration of only the transformer inductance, since inclusion of the LCL filter for each charger in the simulation would cause the model to be too large for our RTDS configuration. The actual signal range for the system is likely smaller than the one found here, although we are not able to find it with the given simulation capabilities.

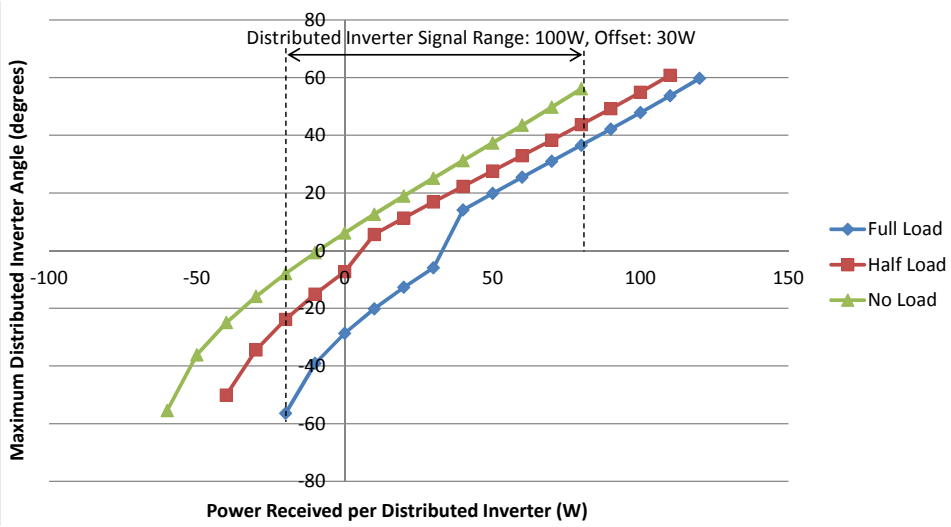

Figure 5.20: Maximum Angle vs Power Received as Load Varies

The three curves on this plot are for full, half, and no loading on the system. The max-

imum received power, within the stability margin, varies slightly as the loading changes. The smallest operating window for these cases is selected and labeled on the figure as the 'Distributed Inverter Signal Range' and is equal to 100 W. This range is not centered around 0 W, due to the presence of leakage power. An offset can easily be programmed into the distributed chargers when the signal power is used to command the fundamental power in order to account for the signal range not being centered around zero. In this case, the offset is 30 W.

It was determined that the signal range for a 32 charger system is 100 W. To determine the signal range as the number of EV on the system varies, several simulations were performed to gather curves similar to the ones in Figure 5.20, but with varying number of EV chargers instead of varying load. Figure 5.21 shows the maximum angle versus distributed charger power curves for varying numbers of distributed chargers. As the number of chargers decreases, the signal range increases.

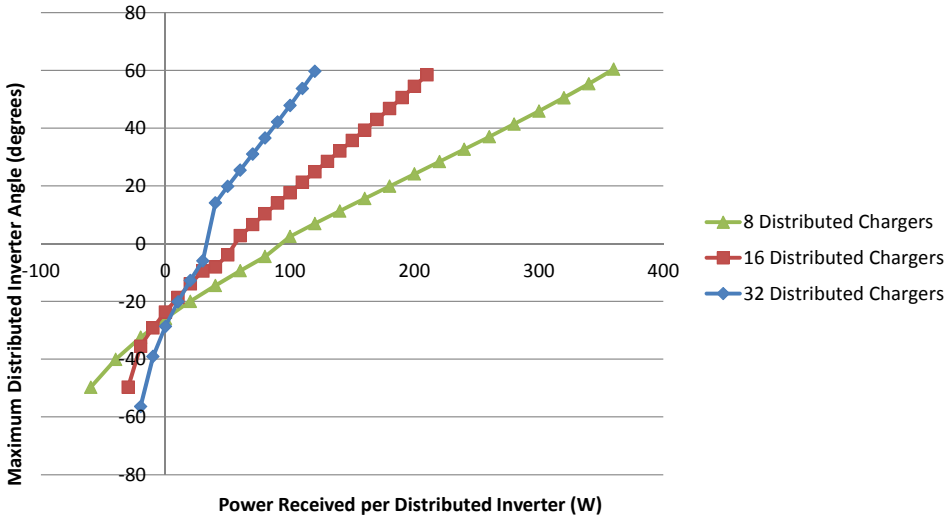

Figure 5.21: Maximum Angle vs Power Received as Number of Chargers Vary

A relationship was developed to quantify the signal range as a function of the number of distributed chargers on the system. Figure 5.22 shows the signal range versus number of distributed chargers. An inverse relationship is visible in this plot. Figure 5.23 shows the inverse of signal range versus number of distributed chargers and a linear relationship which fits the data. Figure 5.24 shows the predicted signal range curve using the curve fitted to the data. The predicted signal range for a system with 128 distributed chargers is highlighted to be 27 W. The equation for the predicted signal range is given in Eq. 5.12.

$$Signal\ Range = \frac{1}{0.000278\#EV + 0.0011} \tag{5.12}$$

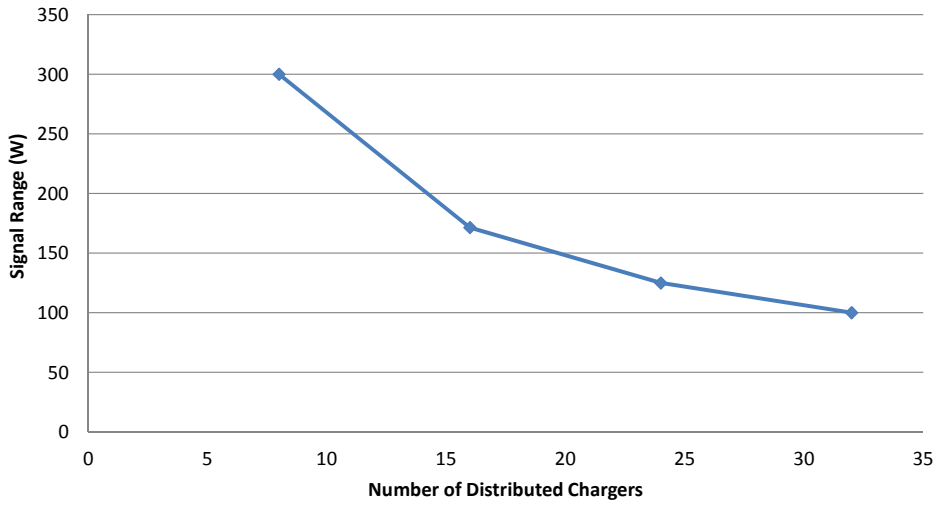

Figure 5.22: Signal Range versus Number of Distributed Chargers

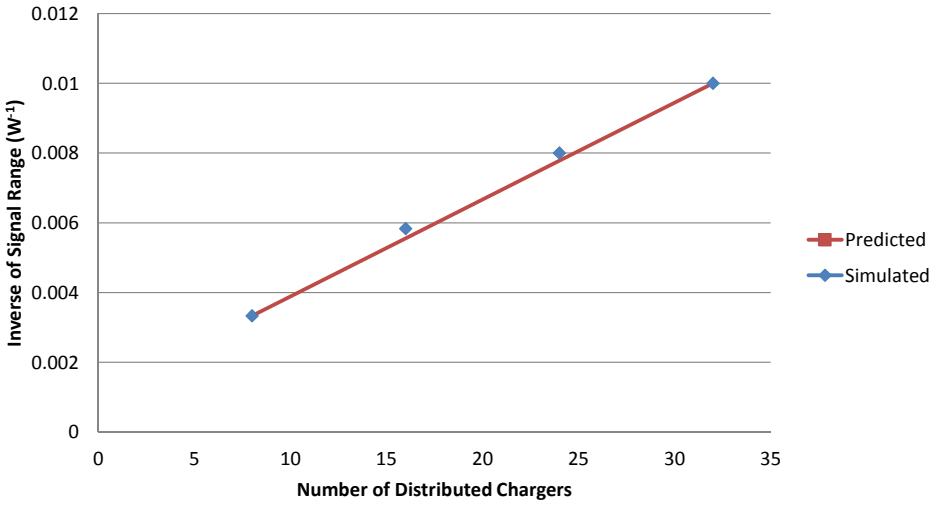

Figure 5.23: Inverse of Signal Range versus Number of Distributed Chargers

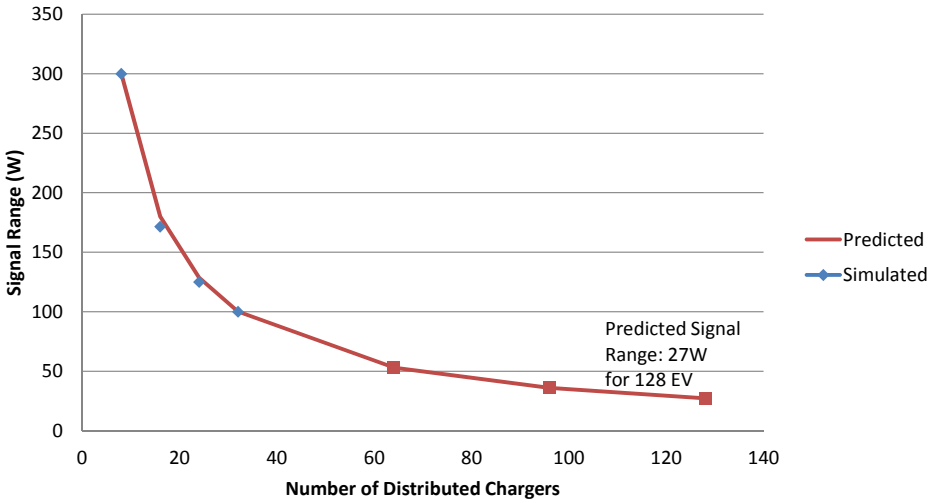

Figure 5.24: Predicted Signal Range versus Number of Distributed Chargers

The inverse relationship between the number of distributed EV chargers and the signal range intuitively makes sense. For a given power injected by the central inverter,

the power per charger should be a fraction of the central inverter power since the central inverter power is divided among the distributed inverters. The offset term comes from the leakage power on the system.

The predicted signal range for the IEEE 13 bus feeder with 128 distributed chargers is 27 W. The fundamental frequency power is per charger is 7.2 kW. The signal power to fundamental power ratio for this case would be 267. This value is used by the controller which is developed the next section.

5.4 Power Electronics and Control

In this section, the ripple droop controller structure is explained. The specifications for the EV charger schematic outlined in a previous chapter are given again in Table 5.1. The schematic and control overview for the converter is shown in Figure 5.25. The development of this control structure and an explanation of each of the blocks in this diagram will be given in this section.

Table 5.1: Bi-directional EV Charger Specifications

EV Charger	
Transformer Ratio	2.4 kV:240 V
Transformer Z	0.02 + j0.03 p.u.(50 kVA, 60 Hz)
Single-Phase $L_{leakage}$	91.7 μH (secondary)
AC Voltage	240 V_{rms}
Switching Frequency	10 kHz
L_{ac}	2.2 mH
C_{ac}	20 μF
V_{dc_bus}	400 V

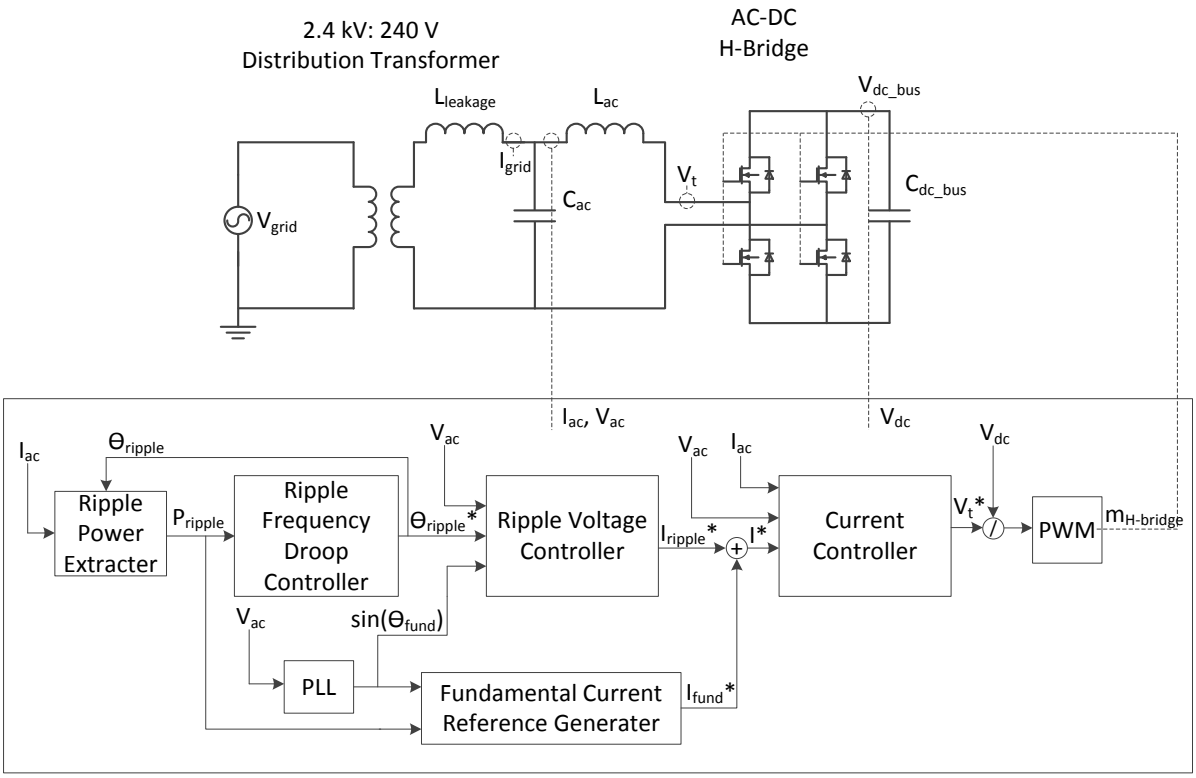

Figure 5.25: EV Charger Schematic and Control Overview

The H-bridge converter presented here is one stage of a two-stage converter that interfaces the storage to the grid. Not shown is the bi-directional buck boost converter that regulates the DC bus voltage. Its design and operation is common and well understood for EV chargers [45]. In our design, the AC/DC stage controls the real and reactive power flow while the DC/DC stage regulates the DC bus voltage. Other topologies include substituting the bi-directional buck converter with a dual active bridge to obtain isolation.

The output filter is designed to reduce the voltage and current harmonics injected into the grid at the switching frequency of the converter (10 kHz). An LCL filter was chosen with the leakage inductance on the distribution transformer is used as the outer inductor.

A major reason for selecting the ripple signal frequency to be close to fundamental frequency is that the output filter design is made simpler. The output filter should be able to pass through not only the 60 Hz signal but also the ripple signal, while rejecting the 10 kHz harmonics. The filter should provide a low impedance path to ground for the switching harmonics while allowing the 60 Hz and ripple signals to pass through. Too low of an impedance to ground at the ripple and fundamental frequencies will cause excess circulating current to flow. Too high of an impedance to ground at the switching frequency will allow unwanted harmonics to enter the grid.

For the controller design, a major challenge is to regulate both the 90 Hz ripple voltage and the 60 Hz fundamental current simultaneously without control interactions.

For a standard, fundamental frequency only, PQ inverter controller, a current control loop regulates the output current to match a desired reference waveform. Current regulation is advantageous over voltage regulation because its dynamics are first order, rather than second order for voltage regulation, it is faster, and it provides built-in over-current protection.

For implementing droop control, whether ripple droop or fundamental droop, the output voltage must be regulated to a voltage with its frequency determined by the droop equation, Eq. 5.13, and its magnitude constant. For droop control, either the H-bridge terminal voltage or the output capacitor voltage can be regulated. Regulating the terminal voltage is the simplest control method, since no voltage feedback is required.

$$\omega_{inv}^{*} = \omega_0 - m(P_{inv} - P_0) \tag{5.13}$$

To combine these two control objectives, fundamental current control and ripple voltage control, one can not simply superimpose the output of the two controllers as in

Figure 5.26. The problem with simply superimposing the outputs of the two controllers is that each controller will attempt to cancel the quantity being regulated by the other. In the current controller, the ripple current caused by the ripple voltage control will be viewed as a disturbance, thus the controller will attempt to mitigate it.

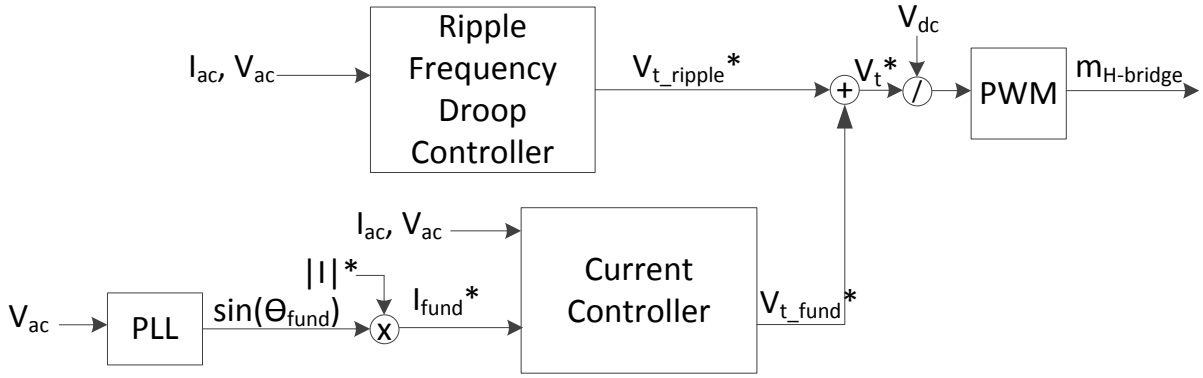

Figure 5.26: Superposition Ripple Droop Controller with Control Interactions

A potential solution to this control interaction is to filter the feedback signals to remove the quantity not being controlled, as in Figure 5.27.

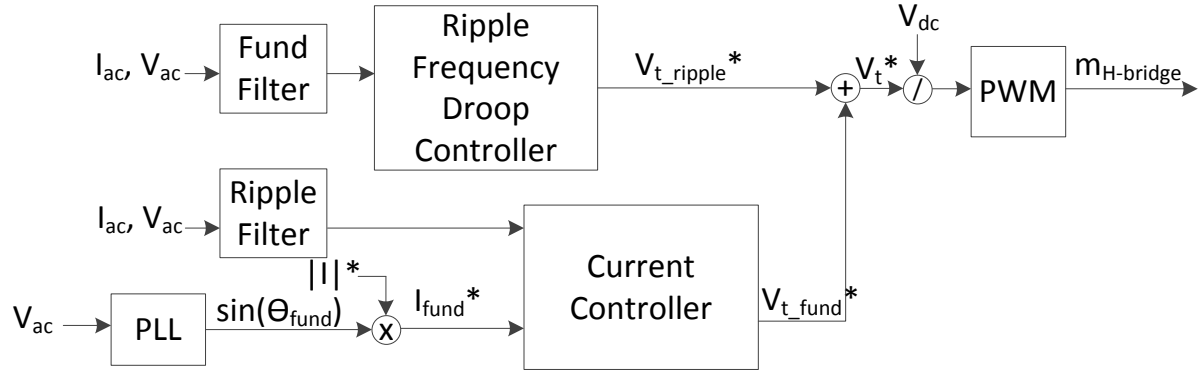

Figure 5.27: Superposition Ripple Droop Controller with Filtered Feedback

The problem with this method is that the feedback delay introduced by the filter must be small compared with the response time of the control loop. The feedback delay must be an order of magnitude faster than the controller in order to avoid introducing the filter dynamics into the system. This is not a problem for the droop controller, since its response time is on the order of a second, so the filters do not have to be very fast. The signal extractor block pictured in the overall control block diagram serves to remove the fundamental frequency component from the feedback signal before it is sent to the ripple droop controller.

On the other hand, it is not possible to filter the ripple frequency components from the feedback signal without introducing dynamics and likely instability into the current control loop. The current controller response time must be small, on the order of 100's of μS for reasonable operation. It is not possible to filter the 90 Hz ripple signal faster than this, thus introducing a delay from a 90 Hz filter would lead to instability in the current loop.

To solve the control interaction problem in the current controller, one must incorporate the ripple control objective into the current controller. This can be done by cascading the droop voltage controller with the current controller. In this configuration, the droop voltage controller serves as an outer control loop to the inner current control loop. The advantage of this configuration is that a ripple droop current reference signal is generated. At the interface between the two loops, the droop reference is simply added to the fundamental current reference. The current loop now regulates both quantities simultaneously.

The outer ripple voltage loop regulates the capacitor voltage to the desired ripple voltage and frequency that is found by the droop controller. Regulating the capacitor voltage, instead of the H-bridge terminal voltage, to the desired ripple voltage allows for

the generation of a current reference. In this configuration, shown in Figure 5.28, there are three control loops in cascade. These loops are the ripple frequency droop controller, the outer ripple voltage controller, and the inner current controller. To ensure that these loops do not interact with each other, the control speeds must coordinated. The inner current controller is the fastest, followed by the outer ripple voltage controller, and finally the frequency droop controller.

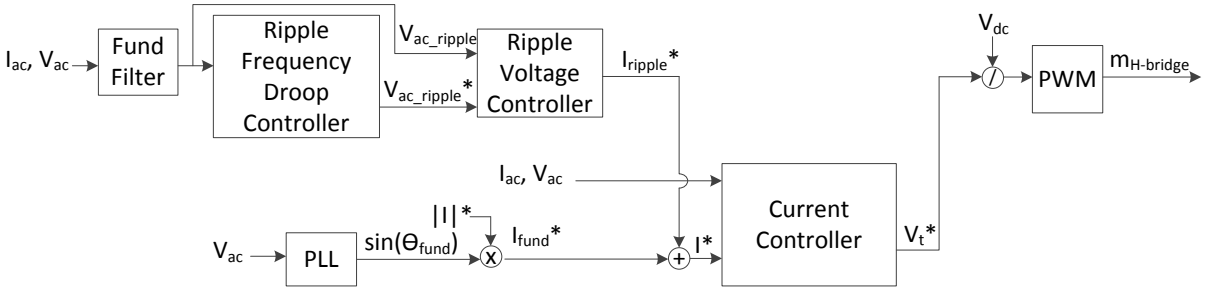

Figure 5.28: Cascaded Ripple Droop Controller to Eliminate Control Interactions

In the following three subsections, each of the control loops will be explained in further detail, starting with the inner current controller and ending with the outer most ripple frequency droop controller. A table of control parameters for the entire ripple droop controller is given below in Table 5.2.

Each of the notch and low pass filters are simple second order filters. The transfer function for the notch filter at frequency f_n and bandwidth BW is given in Eq. 5.14. The low pass filter has a damping factor of 2 and its transfer function is given in Eq. 5.15, for a cutoff frequency of f_c and damping of ζ.

$$G_{notch}(s) = \frac{s^2 + (2\pi f_n)^2}{s^2 + (BW 2\pi f_n)s + (2\pi f_n)^2} \tag{5.14}$$

Table 5.2: Inverter Controller Compensator

	Current Loop	Voltage Loop	Frequency Loop
Settling Time (5τ)	0.4 mS	0.5 S	2.5 S
τ	81 μS	0.1 S	0.5 S
Bandwidth	1.96 kHz	1.6 Hz	0.34 Hz
Total Feedback Delay		0.05 S	0.15 S
Low Pass Filters		100 Hz	3 at 20 Hz
Notch Filters		30, 150, 180 Hz	2*30, 90, 150 and 180 Hz
K_p (m for Droop)	27.12	7.37	0.0025
K_i	$6000 * K_p$	$40 * K_p$	
Steady State Error	0.2% at 60 Hz 0.3% at 90 Hz	0	0

$$G_{low\ pass}(s) = \frac{1}{\frac{1}{(2\pi f_c)^2}s^2 + \frac{2\zeta}{(2\pi f_c)}s + 1} \tag{5.15}$$

Each of the control loops contains primarily first order dynamics, given that the feedback delay is relatively small. τ is defined as the time for the system to reach $1 - 1/e$ or about 63.2% of the final value for a step response. For a first order system, τ is found according to Eq. 5.16. The settling time and bandwidth are found by Eq. 5.17 and Eq. 5.18.

$$H(s) = \frac{1}{\tau S + 1} \tag{5.16}$$

$$T_{settle} = 5\tau \tag{5.17}$$

$$f_{3dB} = \frac{1}{2\pi\tau} \tag{5.18}$$

The speed of the current loop is limited by the switching frequency of the inverter. The current control bandwidth is set at about 2 kHz, approximately an order of magnitude

below the switching frequency, which is 10 kHz.

The speed of the voltage control loop is limited by both the speed of the current control loop and the speed of the feedback filter. The limitation imposed by feedback filter is more constraining than the limitation imposed by the current control loop. Due to the 0.05 second feedback delay, the voltage loop settling time can be no faster than around 0.5 seconds. This corresponds to the time constant and bandwidth given in the table above.

Lastly, the frequency droop loop is limited by both the speed of the voltage control loop and its feedback delay. The speed of the voltage loop is the more constraining factor, limiting the the frequency droop loop to settle at no faster than 2.5 seconds.

5.4.1 Inner Current Controller

The current loop including the plant is pictured in Figure 5.29.

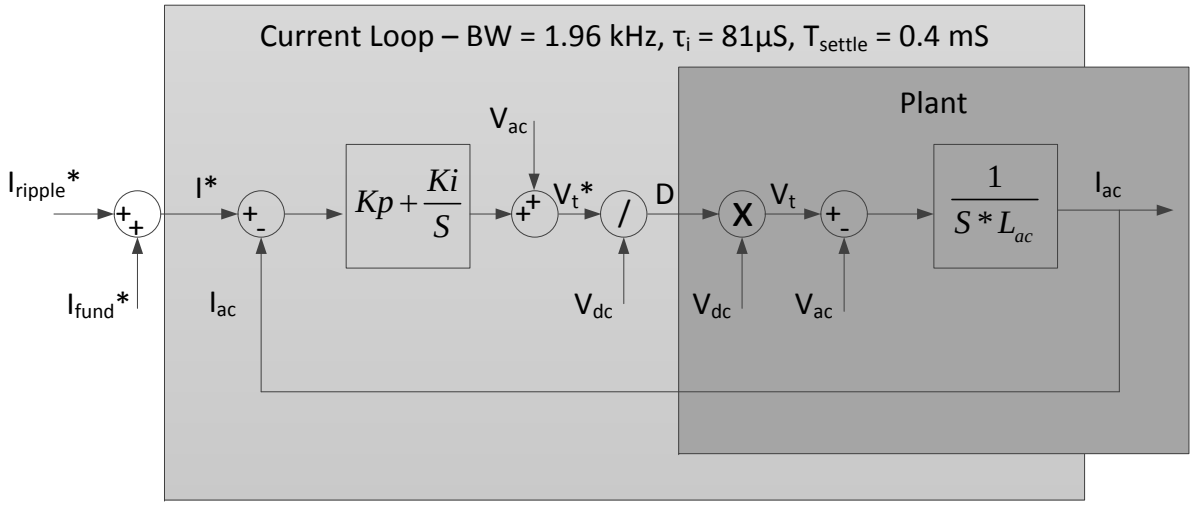

Figure 5.29: Current Control Loop and Plant

The current control is done in the stationary reference frame rather than the synchronous reference frame, because transformation of a single phase quantity into the DQ frame requires filtering the component that is produced by the transformation at twice the original frequency. This filtering adds a delay in the loop that can affect the controller performance, since the current loop bandwidth is rather high. The current loop includes a feed-forward term, V_{ac}, which cancels the supply voltage disturbance in the model and improves controller performance

The proportional term in the controller is selected such that the crossover frequency of the open loop gain is at the desired controller bandwidth of 2 kHz. This controller bandwidth is selected based on the switching frequency of 10 kHz. The integrator term is selected to be as high as possible without introducing too much phase lag into the open loop gain. A large integrator term gives a large open loop gain at the frequencies of the commanded reference signals, 60 Hz and 90 Hz. With this controller, we are able to achieve good performance in both dynamics and at steady state.

The current reference is found by summing the ripple and fundamental references. The ripple current reference is generated by the outer voltage controller, which is explained in the next subsection. The fundamental current reference generation is explained here. Figure 5.30 pictures the generation of the fundamental current reference.

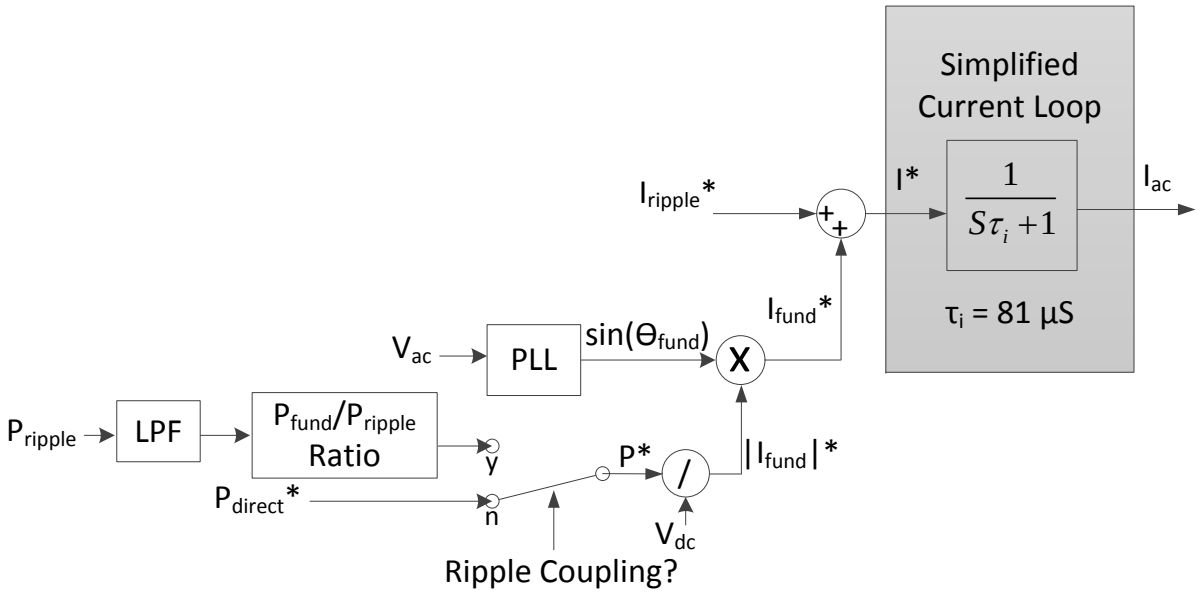

Figure 5.30: Fundamental Frequency Current Reference Generator

The instantaneous reference waveform is found by multiplying the desired magnitude by a unit sign wave in phase with the output capacitor voltage. The unit waveform is synchronized with the output voltage through a single phase power PLL (phase locked loop) [35], shown in Figure 5.31.

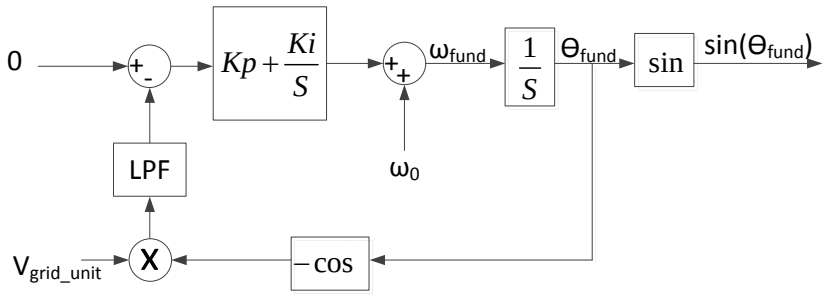

Figure 5.31: Single Phase Power PLL

The desired current magnitude can be controlled either directly or through the ripple power depending on whether ripple coupling is enabled. The power should be controlled directly whenever the EV charger wishes to charge the vehicle. The ripple coupling should be enabled whenever the battery participates in ripple droop control.

5.4.2 Outer Ripple Voltage Controller

The outer ripple voltage control loop including the plant is pictured in Figure 5.32.

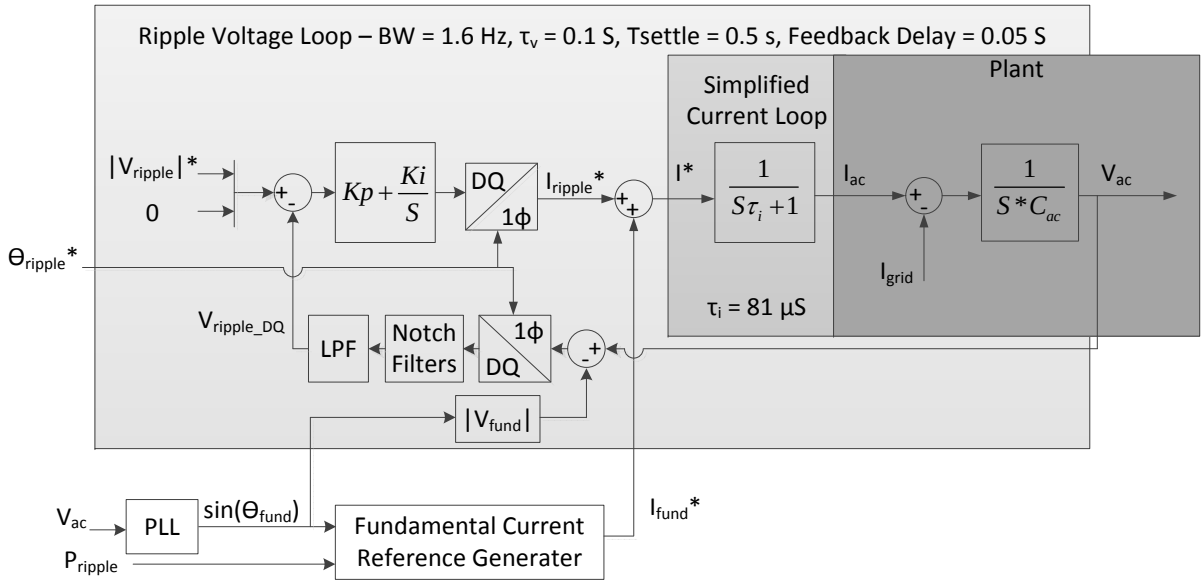

Figure 5.32: Ripple Voltage Control Loop and Plant

The objective of this controller is to regulate the filter capacitor voltage at the ripple frequency to the reference waveform generated by the ripple frequency droop controller. The simplified dynamics of the current control loop is captured in this diagram. Since the current control loop is much faster than the voltage control loop, in analyzing the voltage control loop dynamics we can assume that the current control operates instantaneously.

We can assume that I_{ac} is instantly regulated to I^* in this analysis.

Since this controller is responsible for regulating the ripple voltage only and not the fundamental frequency voltage, the voltage feedback signal must be filtered to remove the fundamental component. If this component are not removed from the feedback, the controller will attempt to regulate it to zero since the reference voltage does not contain a fundamental component.

To filter the fundamental component, first a feed-forward cancellation is done. The fundamental voltage is estimated by a constant magnitude multiplied by the unit waveform generated by the PLL. The feed-forward cancellation is successful in removing most of the fundamental component, but it does not remove it entirely. To remove the remaining component, the signal is rotated at the ripple frequency and passed through low pass and notch filters.

The single phase to DQ transform works by multiplying the signal by a unit sine wave at the desired frequency. The multiplication moves the quantity in the signal from the ripple frequency to DC. According to the trigonometric identity in Eq. 5.19, the resulting signal will include a constant (DC) value equal to one-half the amplitude of the signal at the frequency of interest and a component at twice the signal frequency. The value we desire is found by multiplying the constant term by two and filtering away the higher frequency term.

$$\cos^2\theta = \frac{1}{2}(1 + \cos 2\theta) \tag{5.19}$$

In addition to filtering the term at twice the ripple frequency, we must filter the components that are generated by transforming the fundamental component. These new components occur at the ripple frequency plus and minus the fundamental frequency.

The voltage controller contains notch filters at 30 Hz, 150 Hz and 180 Hz and a low pass filter at 100 Hz. The single-phase-to-DQ and DQ-to-single-phase transformations are pictured in Figure 5.33 and Figure 5.34.

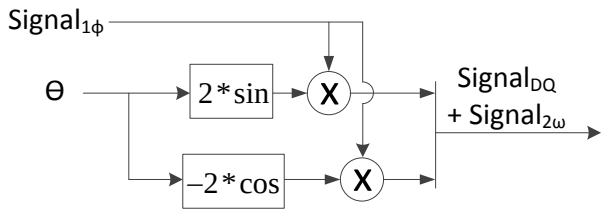

Figure 5.33: Single Phase to DQ Transformation

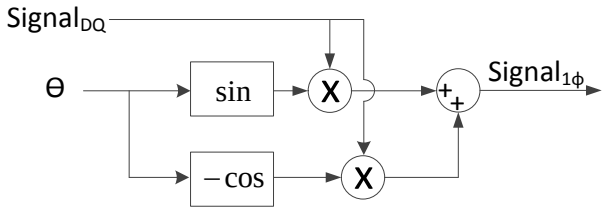

Figure 5.34: DQ to Single Phase Transformation

Because of the delay introduced by this feedback filter of 0.05 seconds, the settling time of the voltage loop can be no less than about 0.5 seconds. This means that the controller time constant and bandwidth are no faster than 0.1 seconds and 1.6 Hz respectively. In the stationary frame, it is not possible to regulate a 90 Hz waveform with a controller with such a low bandwidth. For this reason, the voltage loop is done in the synchronous reference frame at the ripple frequency.

The desired voltage magnitudes for the direct and quadrature axes are constants. The input for this controller is the desired angle for the ripple voltage. This angle is used

in the transformations in the controller. At steady state, the controller regulates a DC quantity with an infinite DC open loop gain, thus there is no stead state error.

5.4.3 Outermost Ripple Frequency Droop Controller

Lastly, the Ripple Frequency Frequency Droop Controller, shown in Figure 5.35, implements the basic droop equation, Eq. 5.13. The output of the controller is the angle of the desired ripple voltage.

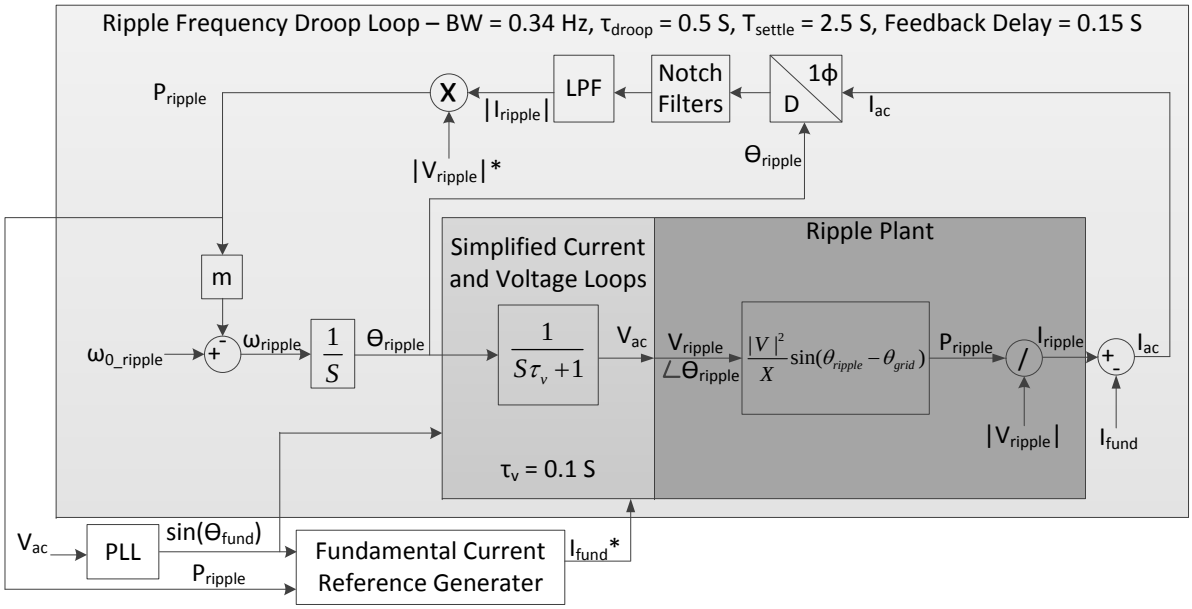

Figure 5.35: Ripple Frequency Droop Control Loop and Ripple Plant

In the figure, the voltage and current loops are simplified to a first order equivalent which has the response time of the voltage loop. The speed of the ripple frequency droop loop is limited by this speed of the voltage loop. The droop loop is set to operate five times slower than the voltage loop in order to avoid introducing the voltage dynamics into

the ripple droop loop. The feedback delay for the ripple droop loop does not significantly affect the dynamics since it is less than one tenth of the settling time of the ripple frequency droop settling time.

The plant pictured in Figure 5.35 is labeled the 'Ripple Plant' since it shows the equations that produce the ripple current from the ripple voltage. The basic power transfer equation between two sources, covered earlier in Chapter 3, determines the power drawn from the converter at the ripple frequency.

The feedback current contains both the fundamental and ripple components. The fundamental component is filtered through the same process described in the 'Outer Ripple Voltage Controller' subsection. The filtering consist of 30 Hz, 90 Hz, 150 Hz, and 180 Hz notch filters and three 20 Hz low pass filters. Such a high number of filters can be included since the ripple droop loop can tolerate a significant delay in the feedback path since its speed is low.

The control parameter m controls the open loop gain for this controller; thus it determines the loop speed. The selection of m is made such that the system speed does not exceed the speed of the voltage loop.

5.5 Practical System Considerations

This short section discusses practical system design considerations that should be considered before a ripple droop control system is implemented. Specifically, we wish to address how the system can be controlled to detect instability, to implement a planned or unplanned shut down, and to be made more redundant by including a backup central inverter.

First, for the case that the system becomes unstable, we propose that a shut down

mode be programmed into the control of each distributed charger. An instability can be triggered by a fault on the system, by a rapid change in load or system configuration, or by an unreachable command from the central inverter. In all of these cases, the instability can be detected by examining the frequency of the ripple voltage on the line. If the frequency exceeds a pre-defined range, each distributed inverter can detect it and shut off its ripple voltage.

For a planned shutdown, we propose that the central inverter inject a voltage at an alternate frequency to the ripple frequency. This 'emergency frequency' could be programmed in each distributed charger. The distributed chargers would be programmed to listen to this frequency continually and whenever the voltage is present, they should simply turn off their ripple voltage so that they no longer exchange power at the ripple signal.

For both cases of a planned shutdown and for an unplanned shutdown in the case of instability, the system can be restored or started up again by signaling from the central inverter. After a period of time, the central inverter can restore the ripple voltage to the line. The distributed inverters can sense this voltage and re-enable their ripple voltage in order to begin exchanging power with the ripple signal.

Lastly, in designing a ripple droop control system, one should consider selecting a backup central inverter at an alternate location on the feeder. In this case, if the central inverter is inactivated by a fault or by something else, the backup central inverter can control the system frequency. The backup inverter can help the system remain stable in this case and initiate a planned shutdown.

Chapter 6

Simulation and Experimental Verification

In this chapter, simulation and hardware-in-the-loop experimental results are presented in attempt to verify the theory developed in the previous chapters. In addition, the purpose of each simulation and the specifications of the models and simulation environments are given. Figure 6.1 illustrates the three configurations for the simulations presented in this chapter.

First, a single inverter switching model was simulated to verify the control algorithms. Next, a hardware-in-the-loop (HIL) configuration was simulated in order to test ripple droop control on a full-scale feeder model with multiple distributed chargers, including an external hardware emulator to capture the switching dynamics of a distributed charger. Finally, a large number of distributed chargers were simulated on the distribution feeder to capture the dynamics of the system at initialization, changes in power commanded, and addition and removal or chargers and system load.

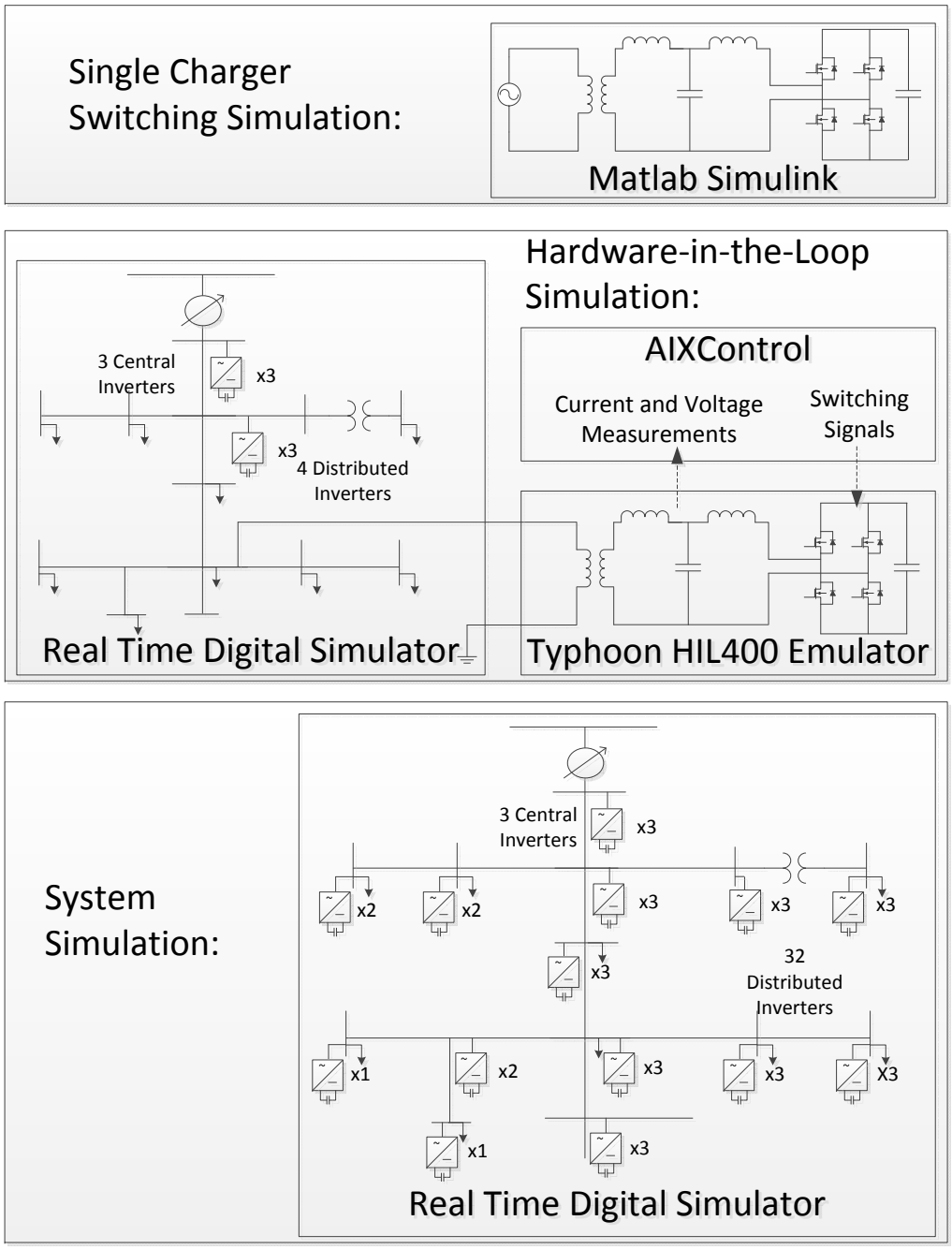

Figure 6.1: Overview of the Three Simulation Configurations

6.1 Single Charger Switching Simulation

In this section, results are presented from simulations performed with the software Matlab Simulink and the PLECS power electronics blockset. Simulations were carried out on a switching model of a distributed charger, pictured in Figure 6.2. The model includes the output filter and transformer and is connected to an infinite bus. The specifications for the model are the same as those described in the 'Charger Specifications' subsection in Chapter 3.

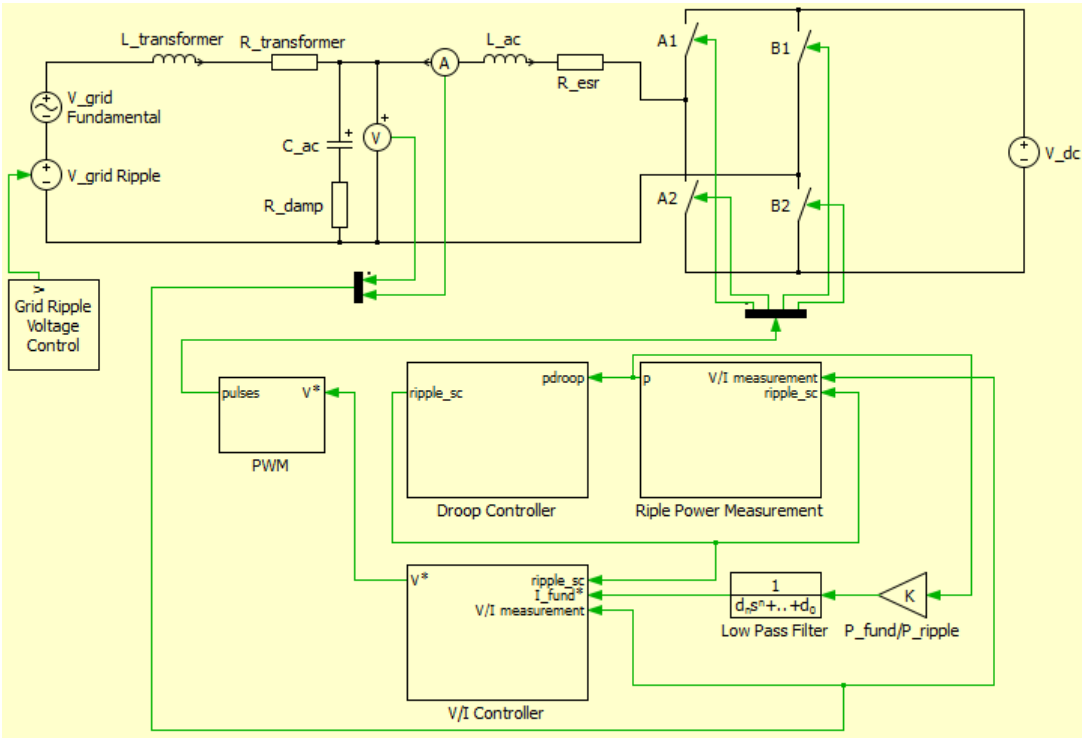

Figure 6.2: Model of Grid-Connected Charger in PLECS

The purpose of the switching model simulation is to verify the power electronics control and the design of the output filter. Specifically, we want to demonstrate the

simultaneous control of the fundamental and ripple signals. These tests verify the proper operation of the various control blocks and demonstrate the effectiveness of the ripple signal extraction in the presence of fundamental frequency voltage and the switching harmonics.

The simulated model is an H-bridge inverter with an output filter connected to an infinite bus through a transformer. The infinite bus presents a stiff voltage source at both fundamental and ripple frequencies. The bus ripple frequency is modified during the simulation in order to command power from the charger.

The simulation time totals 10 seconds. For the first six seconds, the ripple droop frequency is held constant at the nominal value such that the droop controller reaches an equilibrium at zero power exchanged. During this time, the charger draws pulses of negative and positive full power (7.2 kW) before returning to zero power.

For the final four seconds of the simulation, the fundamental power is controlled proportional to the ripple droop signal power. The P_{fund}/P_{droop} ratio is set to 7200 such that for one Watt of ripple power the controller will command the full rated power of 7.2 kW. At six seconds of simulation time, the ripple frequency of the infinite bus is changed by m such that the inverter will transfer 1 W of power in the droop signal. The ripple droop power reaches equilibrium in less than 1 second. At 8 seconds into the simulation, the droop frequency is once again changed such that droop power is reversed. The equilibrium is once again reached in less than 1 second. The fundamental frequency power is controlled to reflect the ripple droop power.

The charger output current, fundamental power and ripple power waveforms are given in Figure 6.3.

For the first six seconds of simulation time, the fundamental frequency power is controlled independently. During the last four seconds of the simulation it is proportional

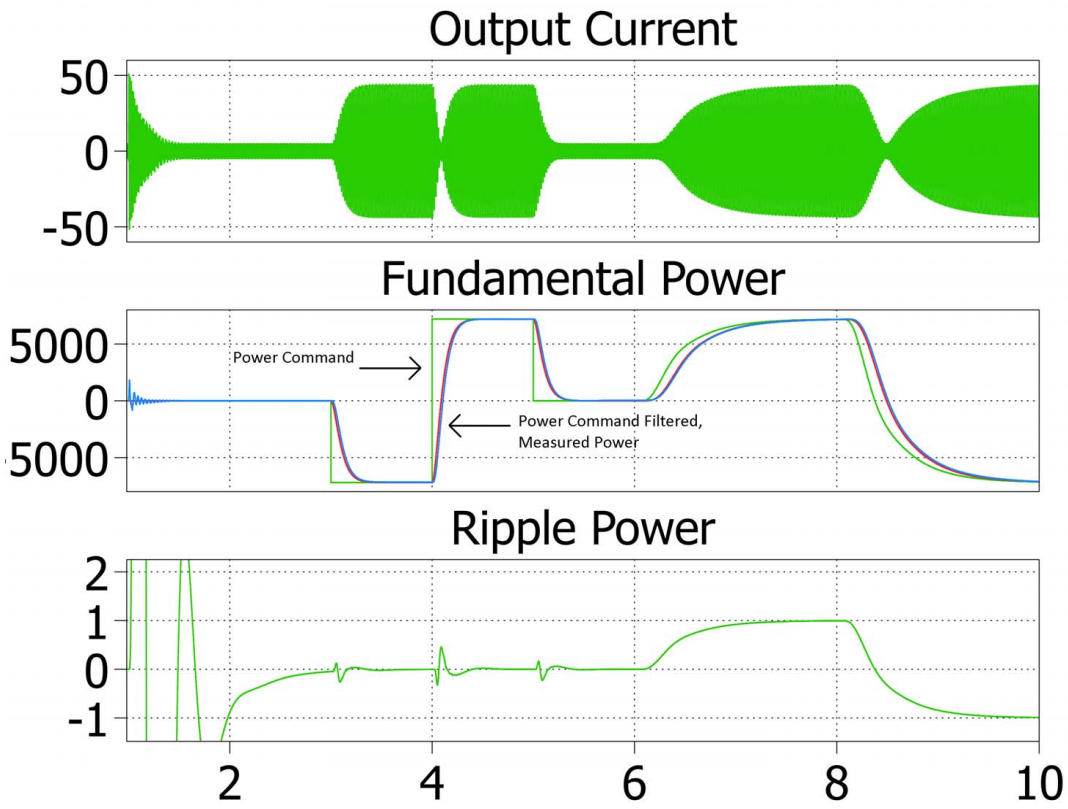

Figure 6.3: Switching Simulation Results

to the ripple droop power. The ripple droop power experiences a transient initially. This is an unavoidable transient since the controller must synchronize with the grid ripple frequency by exchanging power with it. To minimize the effects of this transient, the ripple droop controller should reach an equilibrium before the ripple droop power is used to control the fundamental frequency power.

Decoupling of the fundamental and ripple signals is demonstrated during the initial six seconds of simulation, while intentional coupling is demonstrated in the final four seconds. During the first two seconds, the fundamental power is kept very close to zero while the ripple power goes through the initialization transient. At simulation times of 3

s, 4 s, and 5 s, the ripple power transient is minimized while step changes occur in the fundamental power.

The output filter voltage and current are shown over a few cycles in Figure 6.4 to illustrate the superposition of the fundamental and ripple quantities and to demonstrate the effectiveness of the output filter to minimize switching harmonics. The presence of the ripple signal is noticeable in the output voltage but not the output current. This is because the ripple voltage magnitude is 3% of the fundamental voltage magnitude, while the ratio of the current magnitudes is smaller. The presence of the ripple voltage can be observed by noticing the varying the peak values of the voltage waveform.

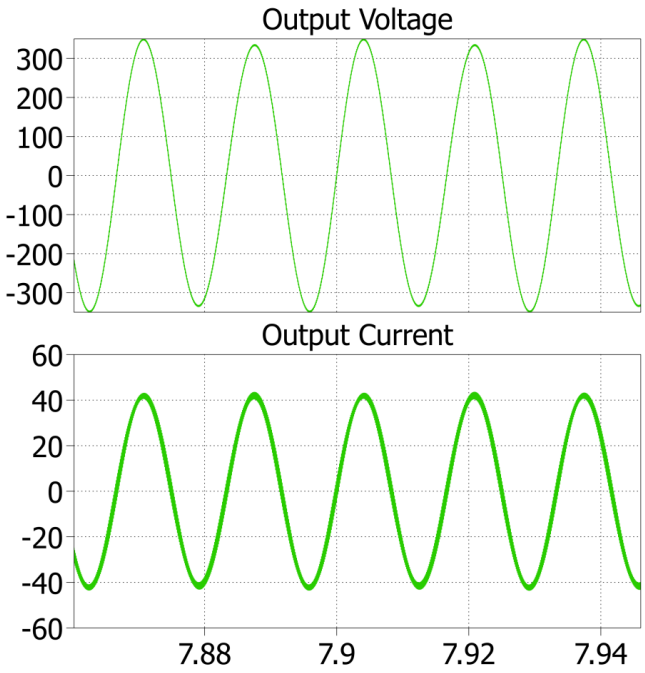

Figure 6.4: Output AC Voltage and Current of Switching Simulation

6.2 Hardware-in-the-Loop Simulation

A hardware-in-the-loop simulation was performed to test the dynamics of a distributed charger, controlled by an external DSP, with a full 13 bus distribution feeder including 6 average-model chargers. The full configuration including pictures from the laboratory setup is shown in Figure 6.5.

There are several purposes for the HIL simulation. First, this simulation demonstrates the ability of ripple droop control to function on a distribution feeder in the presence of the fundamental frequency voltages and currents. Second, this simulation verifies the ability of a digital signal processor (DSP) to implement the distributed charger controller algorithm. Decoupling and independent control of the fundamental and ripple signals is demonstrated. Filtering of the zero sequence ripple voltage and current at the substation transformer is demonstrated. Lastly, by including an external hardware emulator connected to the RTDS through analog input and output channels, noise is introduced into the simulation. This simulation demonstrates the stability of ripple droop control in the presence of this noise.

6.2.1 Feeder Model in RTDS

The IEEE 13 Bus Feeder, described in the first subsection of Chapter 3, was modeled in the RSCAD software, which is used to create power system models to simulate in the RTDS. The main advantage of the RTDS over simulators such as Simulink and PSCAD is that the simulation is performed in real-time which enables connecting external hardware to interface with the simulation. In addition, the RTDS is computationally powerful, so it is advantageous even for simulations that do not involve a external hardware. These simulations are performed much quicker than in Simulink or PSCAD. This second advantage

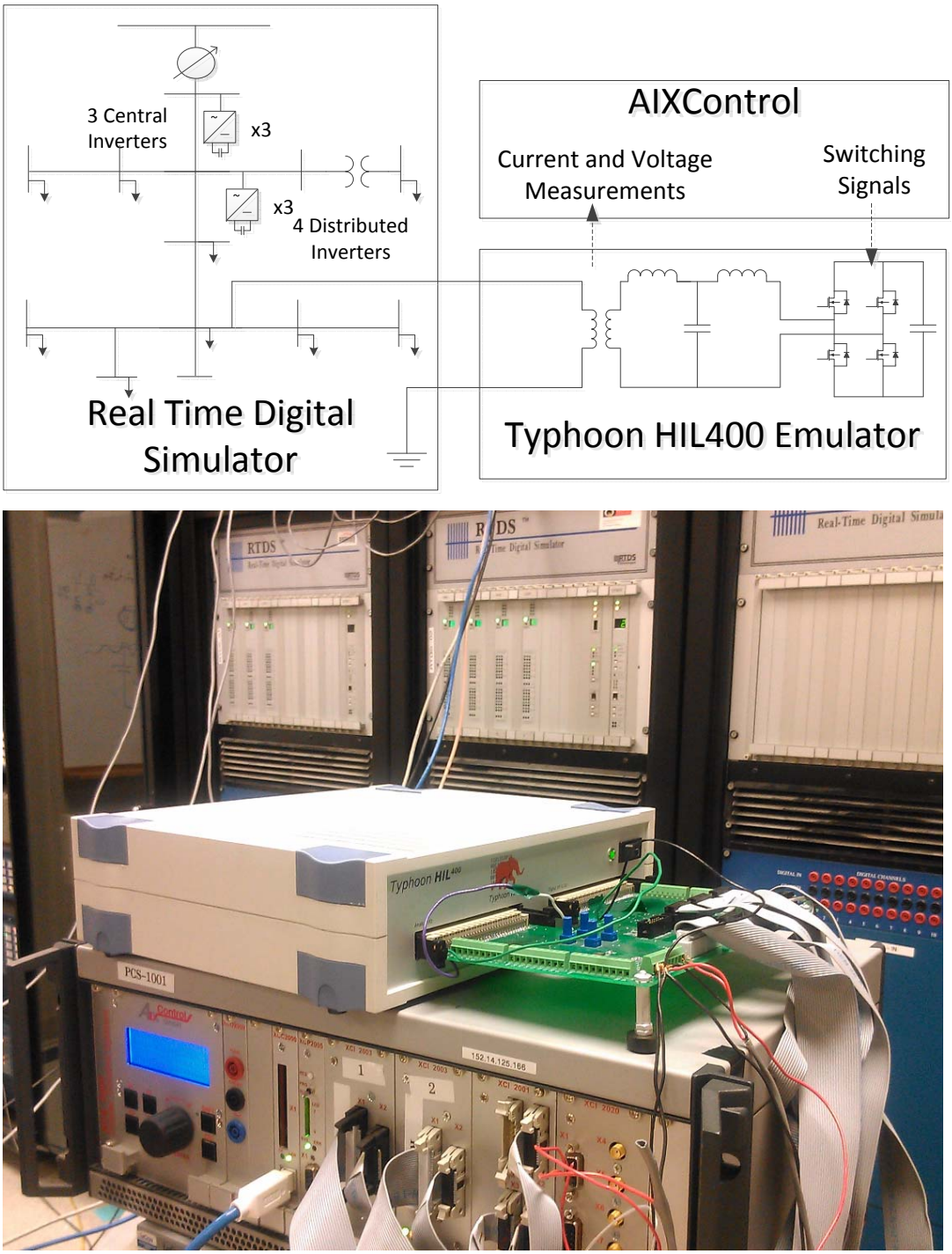

Figure 6.5: Hardware-in-the-Loop Simulation Configuration

is utilized in the next section, System Simulation.

To ensure real-time simulation, there are certain restrictions when modeling in the RTDS. These restrictions are dependent on the number of processors in the particular rack that is used for simulation. For the case of this work, the configuration of the RTDS rack that is used includes two PB5 and two GPC processors. Other configurations are possible for a more powerful simulator. For this configuration, the maximum number of electrical nodes is 72 and for our particular model, the smallest time step is 25 μS. The 72 node limitation does not effect our HIL simulation, however it does limit the system simulation described in the next section.

The RTDS allows for a time step from 50 μS to as low as 10 μS in its large-time-step mode and even smaller in its small-time-step mode. The disadvantage of the small-time-step mode is that the number of electrical nodes and control components allowed is greatly reduced. To include the entire feeder, the large-time-step mode must be used. The major disadvantage of using the large-time-step mode is that it is not possible to implement a switching model with a relatively high switching frequency. For our case, the RTDS time step equates to 40 kHz, whereas our switching frequency is 10 kHz. The resolution of four times our switching frequency is not nearly high enough to accurately simulate the switching dynamics. For this reason, we have used average models for the chargers in the RTDS model. This trade-off is mitigated by adding an external power electronics emulator capable of emulating the switching dynamics of a converter.

Within the large-time-step mode, the minimum time step that can be used varies depending on the complexity of the model. Through experimenting with the model and simulation, we determined that a time step of no larger than 25 μS is required to achieve correct operation of inverter controller. With any fixed time step, there is a fixed amount of computation that can be completed by the control elements. For the 25 μS time step,

it was found that the RTDS is able to simulate up to 6 inverters and their controllers, along with the 13 bus feeder. Three inverters are used as the central inverters on each phase, while the other three are distributed inverters, one per phase. A fourth distributed inverter is simulated by the external emulator.

Before adding the chargers to the model, the feeder was modeled and verified to match the specifications given in the IEEE report [37]. A plot of the voltages, currents, and current angles at each bus compared to the values from the standard is given in Figure 6.6. The currents at each branch are within 0.32 A and 2 degrees of the standard and the voltages are within 1.25 V per unit.

An overview of the RSCAD model with the 6 average-model inverters is given in Figure 6.7.

The specifications for the RTDS simulation are summarized in Table 6.1.

Table 6.1: RTDS Model Specifications - HIL Experiment

RTDS Feeder Model with EV Chargers	
Central Inverters	3
Distributed Inverters	3
Externally Controlled Source	1
Output Signals	$V_{external\_charger}$
Input Signals	$I_{external\_charger}$
Rack	2
Time Step	25 μS, 40 kHz
AI Resolution	$\pm$10 V, 16 bits
AI Sampling Time	6 μS Minimum
AO Resolution	$\pm$10 V, 16 Bits
AO Sampling Time	1 μS Oversampling
Current Controller Bandwidth	1.7 kHz
Droop Slope	0.00343 radians/s/W

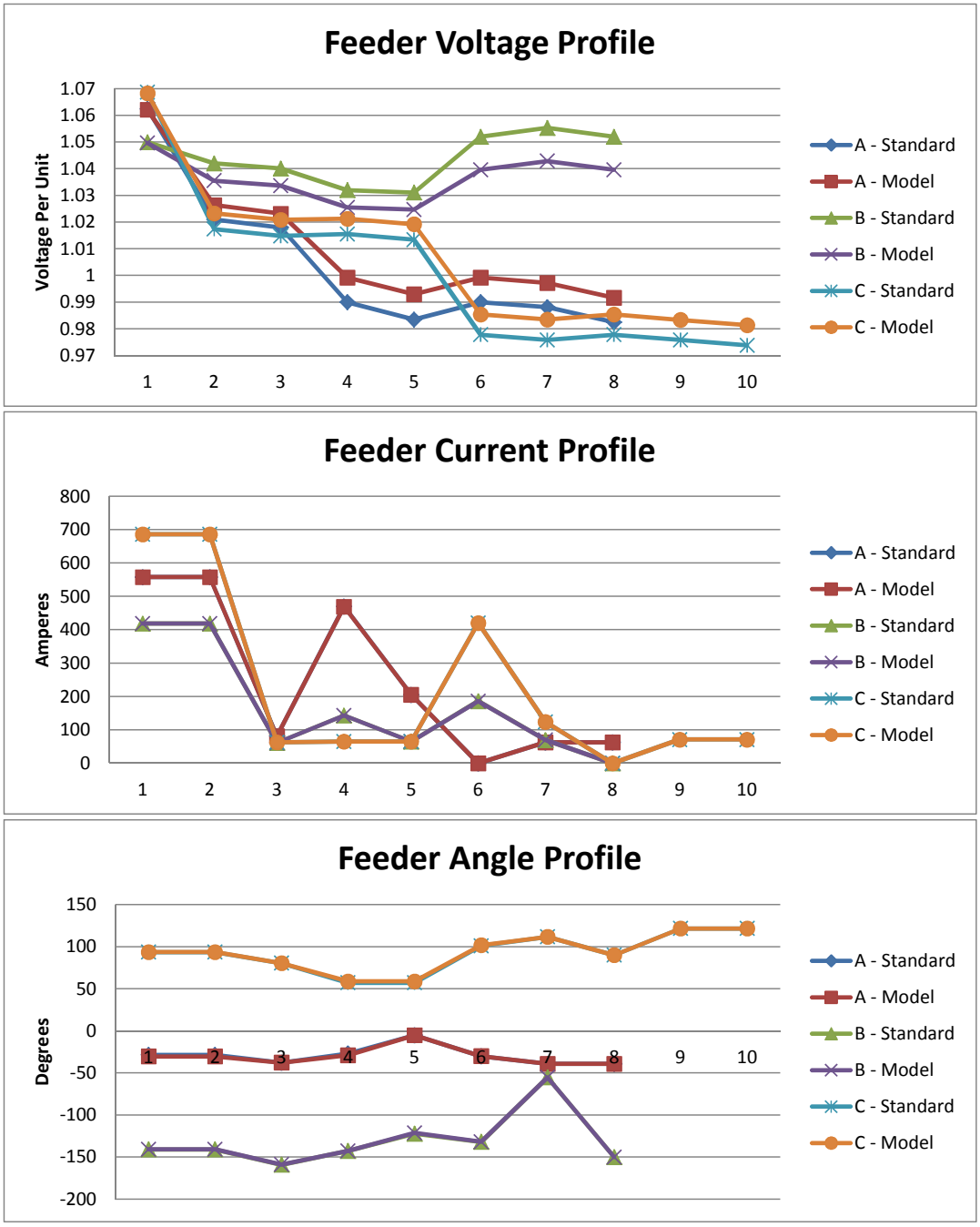

Figure 6.6: Verification of IEEE 13 Bus Feeder Model in RSCAD

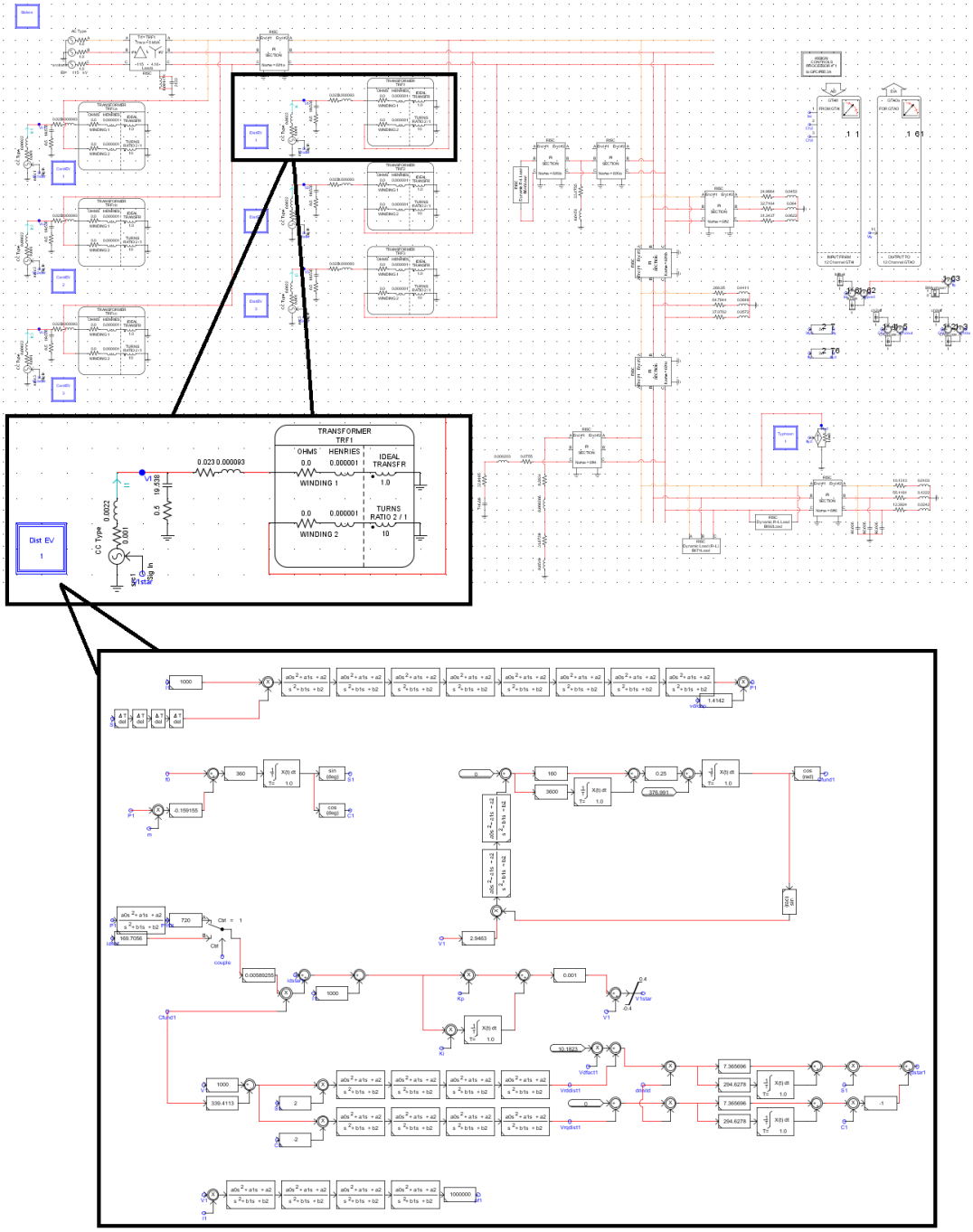

Figure 6.7: Model of IEEE 13 Bus Feeder with 6 Chargers and an External Source in RSCAD. Breakout Views of Single Charger and its Controller

6.2.2 Charger Emulator in Typhoon HIL400

The Typhoon HIL400 is a power electronics emulator that allows for rapid prototyping and HIL testing. The Typhoon emulator is similar to the RTDS in that it is able to simulate a converter in real time. It reads in analog and digital signals used for sources and gate signals and generates output signals that correspond to currents and voltages in the simulation. The difference between the Typhoon HIL400 and the RTDS is that the Typhoon is much smaller and much more specialized. Only a single converter can be simulated with this device. However, the resolution is much higher than that of the RTDS. For this reason, it is able to easily emulate switching models of power electronics converters. The schematic for the emulated converter, as seen in the Typhoon HIL Control Center Schematic Editor, is given in Figure 6.8 and the interface between the Typhoon HIL400 and the RTDS is pictured in Figure 6.9.

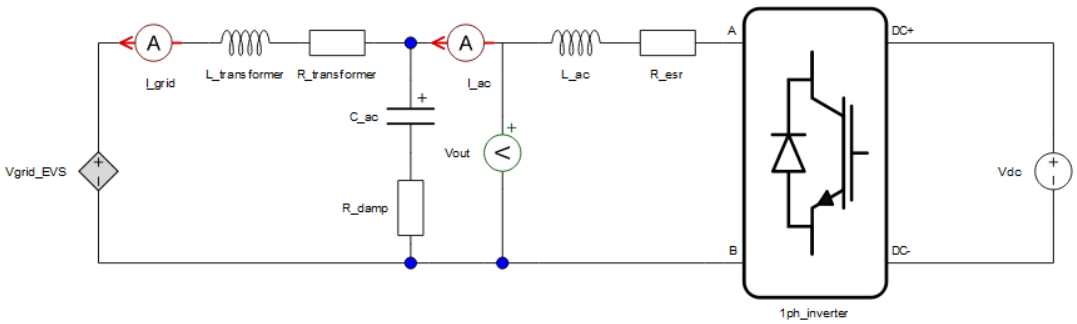

Figure 6.8: Model of Charger in Typhoon HIL

Controlled voltage and current sources are used to link the two real-time simulations together. The current from the switching emulator is sent to the RTDS power system emulator and injected into a bus. At the same time, that bus voltage is sensed and sent to the emulator to control its grid voltage. The resolution of the Typhoon emulator is much

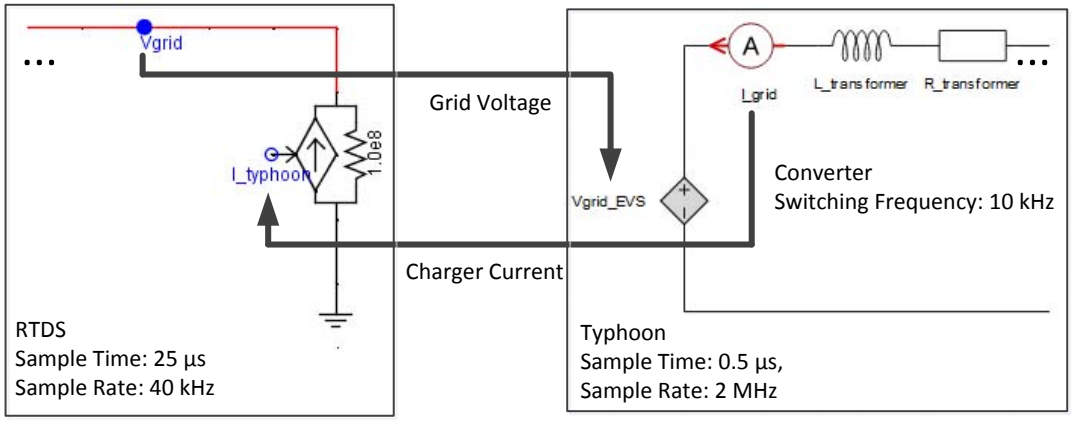

Figure 6.9: HIL Interface between Feeder and Charger

higher than that of the RTDS (2 MHz and 40 kHz respectively), however, the RTDS sampling rate is high enough to capture some of the switching dynamics of the converter (switching at 10 kHz).

The specifications for the Typhoon HIL simulation are summarized in Table 6.2.

Table 6.2: Typhoon Model Specifications

Typhoon HIL400 Charger Model	
Voltage Sources	2
Passive Elements	6
Switches	4
Measurements	3
Output Signals	I_{grid}, I_{ac}, V_{ac}
Input Signals	V_{grid}, Gate Pulses
Time Step	0.5 μS, 2 MHz
Analog I/O Resolution	$\pm$5 V, 12 bits
Switching Frequency	10 kHz

6.2.3 Charger Controller in AIXControl

The final component in the HIL simulation is the AIXControl DSP. This controller is interfaced with the Typhoon HIL400. The output filter current and voltage from the emulator is sent to the controller. The controller implements the ripple droop control algorithm and generates the switching pulses to be sent back to the emulator.

By implementing ripple droop control in the AIXControl, we are able to further verify the control algorithm we developed. Through this test, we verify proper control operation with realistic conditions such as discretized filters, noise in analog input signals, and possible loss of precision in analog to digital conversion. The specifications for the AIXControl DSP and for the ripple droop control algorithm implemented are summarized in Table 6.3.

The specifications for the AIXControl are summarized in Table 6.3.

Table 6.3: AIXControl Program Specifications

AIXControl Ripple Droop Controller	
Output Signals	$GatePulses$
Input Signals	V_{ac}, I_{ac}
Processor	100 MHz Floating Point
AI Resolution	$\pm$10 V, 14 bits
AI Sampling Rate	140 kHz
Implemented Sample Rate	50 kHz
Switching Frequency	10 kHz
Current Controller Bandwidth	1.7 kHz
Droop Slope	0.00343 radians/s/W

6.2.4 HIL Results

With the tests and results in this section, we attempt to demonstrate the ability of the controller to regulate the fundamental frequency current while participating in ripple droop control.

The first set of results from the HIL simulation are a series of steady state waveforms that demonstrate the proper operation of the model. Figure 6.10 shows the voltages at the point of common coupling between the central inverters and the grid. Due to the unbalance of the loads on the three phases, the voltage magnitudes are not uniform. The central inverter current during ripple droop operation, while no fundamental power is exchanged with the grid, is shown in Figure 6.11. One can see the zero sequence nature of the ripple current. The distributed charger current during ripple droop operation, with fundamental power exchanged with the grid, is shown in Figure 6.12. Lastly, the voltage and current from the external charger, emulated by the Typhoon HIL400, are shown in Figure 6.13 and Figure 6.14.

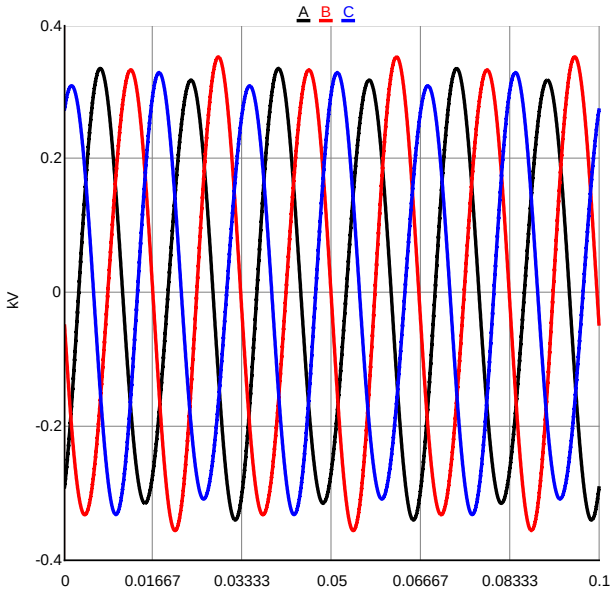

Figure 6.10: Central Inverter PCC Voltages

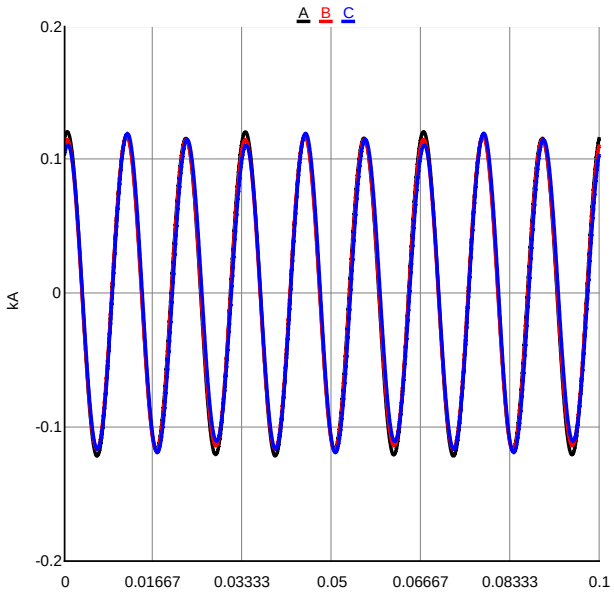

Figure 6.11: Central Inverter Current - Only Ripple Power

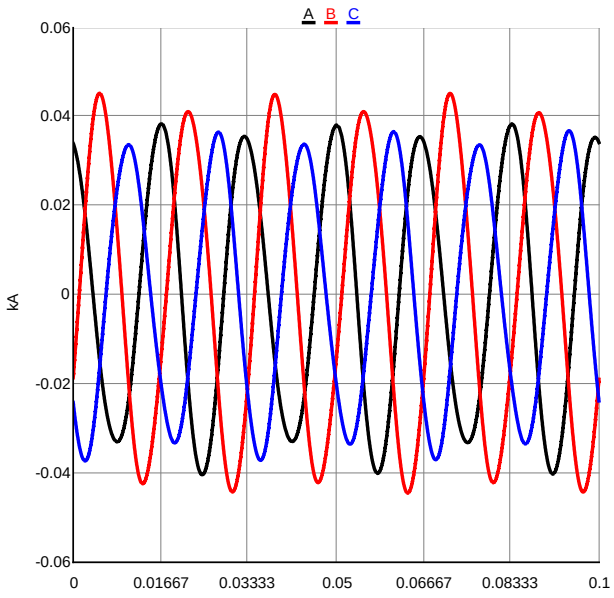

Figure 6.12: Distributed Inverter Current - Ripple and Fundamental

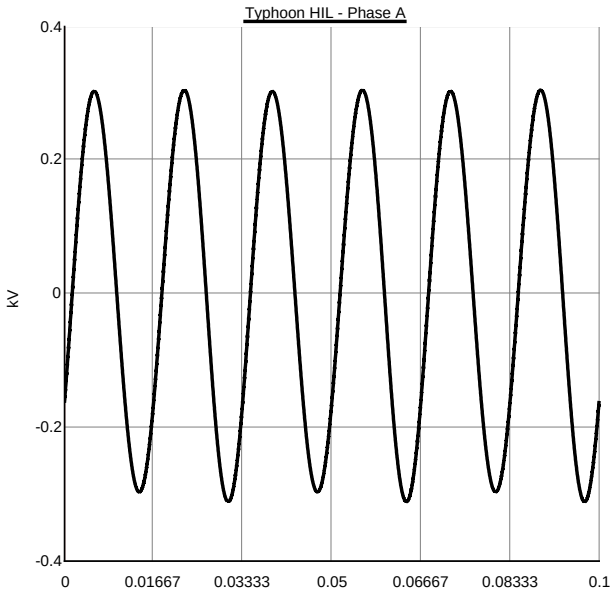

Figure 6.13: External Charger Voltage

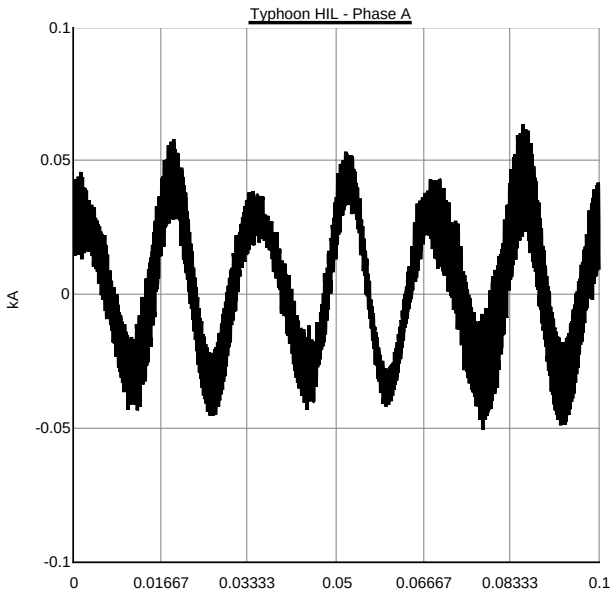

Figure 6.14: External Charger Current - Ripple and Fundamental

The noise in the external current is clearly visible in these waveforms. The voltage waveform is rather clean since it is generated internal to the RTDS. This noise is due to the analog interface between the Typhoon and the RTDS. Despite the noise, the ripple controller operates correctly. Figure 6.15 and Figure 6.16 show a much closer view of the external charger current. In Figure 6.16 one can see the individual data points that compose the signal. The switching frequency of the charger, emulated external to the RTDS, is 10 kHz while the sampling frequency of the RTDS is 40 kHz. This plot verifies that the RTDS captures 4 points per switching cycle from the external charger current waveform.

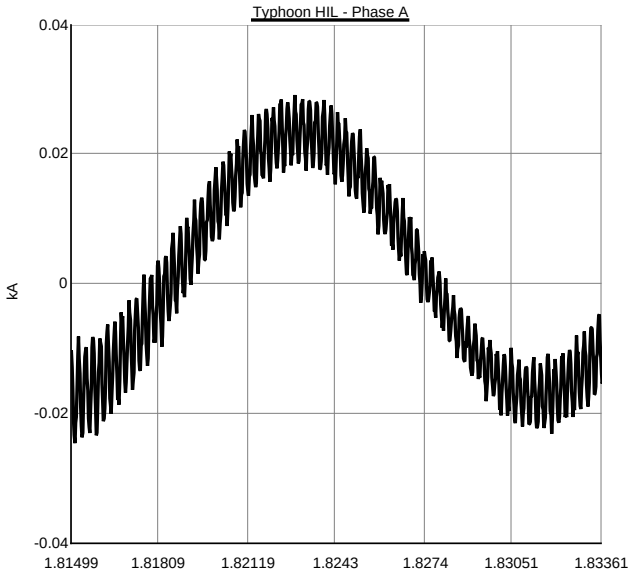

Figure 6.15: External Charger Current - Smaller Time Scale

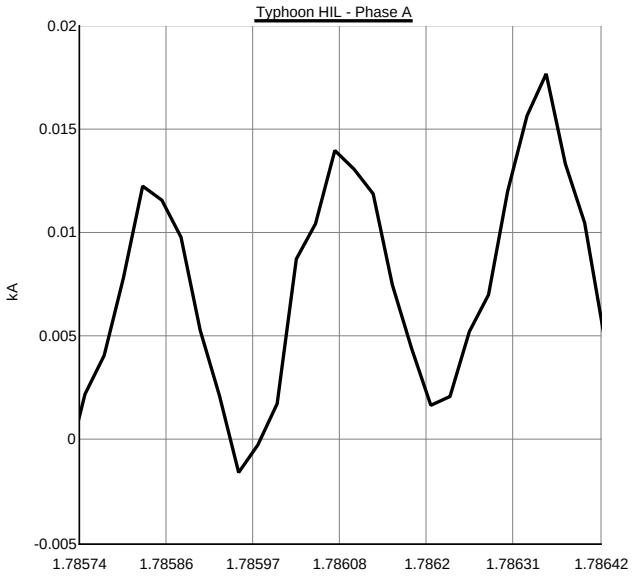

Figure 6.16: External Charger Current - Smallest Time Scale

The next few plots test the dynamic operation of the of the central and distributed chargers simulated in the RTDS before the Typhoon emulator is incorporated into the simulation. First, the fundamental frequency current control is demonstrated. Then, the initialization of ripple droop control is shown for the central then distributed chargers. Lastly, the response of the distributed chargers to step changes from the central inverters is shown.

Figure 6.17 and Figure 6.18 show the ability of the central and distributed controllers to regulate their fundamental frequency voltage very rapidly. These plots show the step response of the fundamental frequency current. It is important for the chargers to initially regulate the fundamental frequency current before the ripple droop control is enabled. This is because the fundamental control is much faster that the ripple control since the ripple control contains many filters to extract the 90 Hz component.

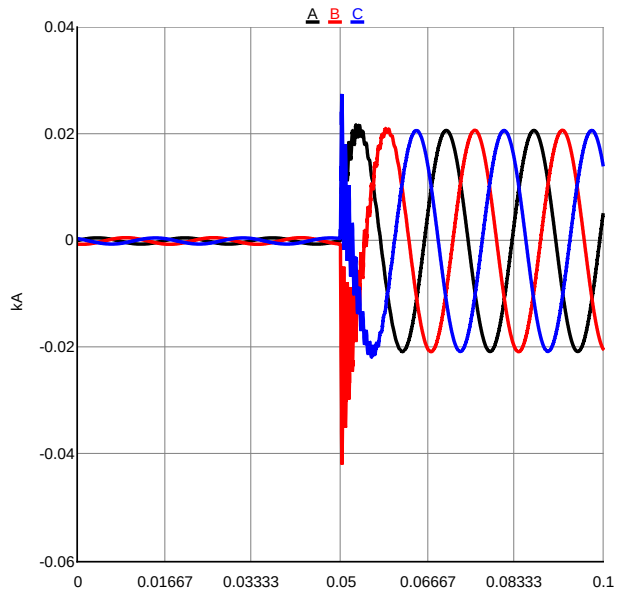

Figure 6.17: Fundamental Current Step Response by Central Inverter

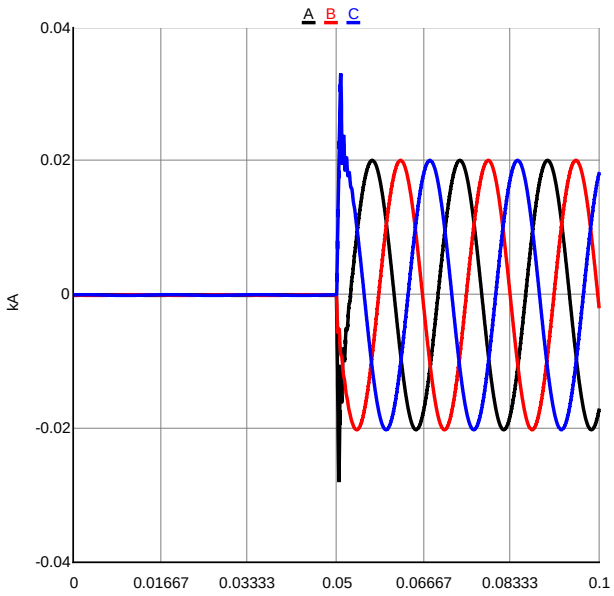

Figure 6.18: Fundamental Current Step Response by Distributed Inverter

The next few waveforms show the initialization of the ripple controllers. The ripple control is initialized after a period of at least 2 seconds after the charger is connected to the grid. This period allows for the notch and low pass filters in the controller to reach a steady state Figure 6.19 shows the ripple power of the 3 central inverters at initialization as well as the total power which is the sum of the three. This total power is equal to the leakage power whenever the distributed charger power is equal to zero. Figure 6.20 shows the regulation of the direct and quadrature components of the output ripple voltage by the ripple controller at initialization.

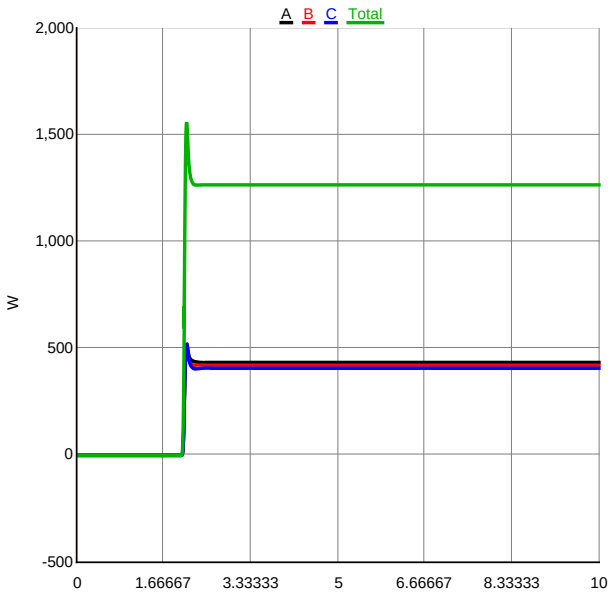

Figure 6.19: Central Inverter Power at Initialization

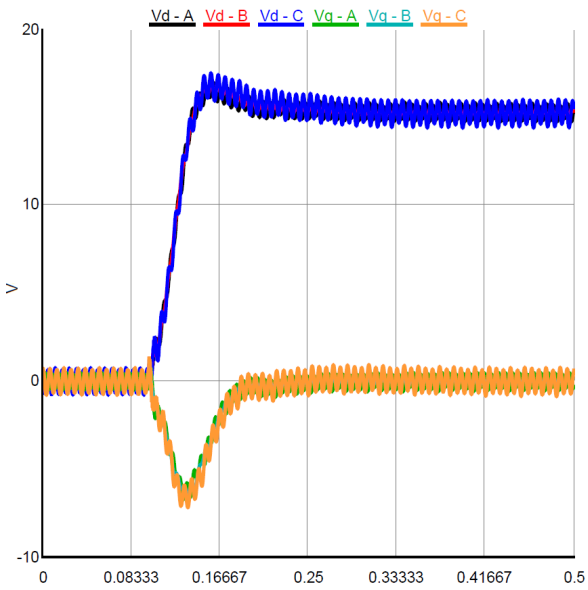

Figure 6.20: Central Inverter Ripple Voltage DQ Regulation at Initialization

After the central inverters establish the ripple voltage for the feeder, the distributed chargers are initialized. Figure 6.21 and Figure 6.22 show the distributed charger power at initialization and the response by the central inverters. For each of these tests, the frequency is held at the nominal 90 Hz, which corresponds to zero power exchanged with the grid from the distributed chargers.

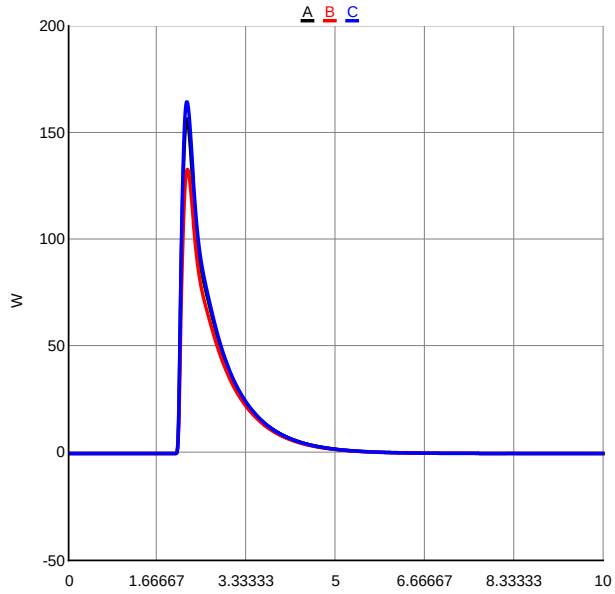

Figure 6.21: Distributed Charger Power at Initialization

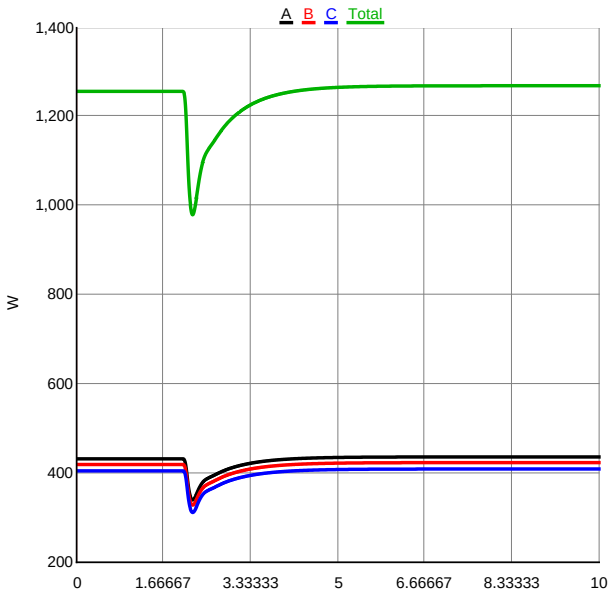

Figure 6.22: Response of Central Inverter to Initialization of Distributed Chargers

Next, the coupling between ripple power and fundamental power is demonstrated. For the next two tests, the central inverter controller alters its output frequency to command power from the distributed inverters. In two tests, the distributed charger power goes from 10 W to -10 W and from -10 W to 0 W. The fundamental power is commanded to change according to the ripple power, where 10W corresponds to full output power of magnitude 40 A. As described previously, the ripple power is sent through a low pass filter before it is used to command the fundamental current. Figure 6.23 and Figure 6.24 show the central inverter total power for these three step responses. The distributed inverter ripple power, filtered ripple power, and fundamental power for the three step responses are given in Figure 6.25 and Figure 6.26. Lastly, the current from one of the inverters for the two step responses are shown in Figure 6.27 and Figure 6.28.

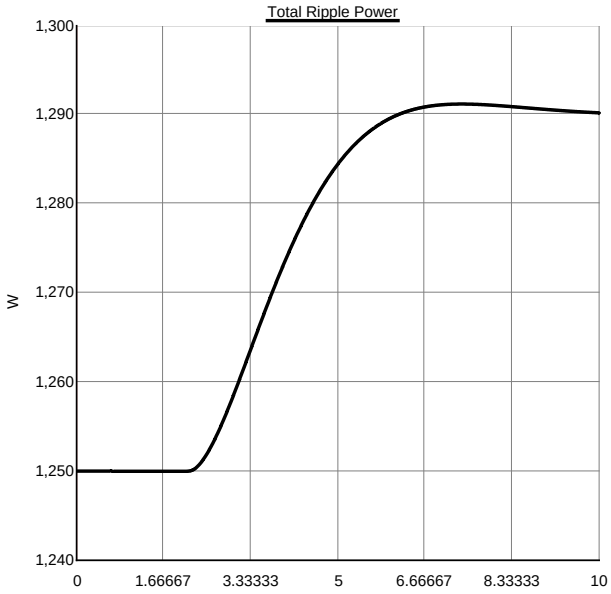

Figure 6.23: Central Inverter Total Power Step Response 1

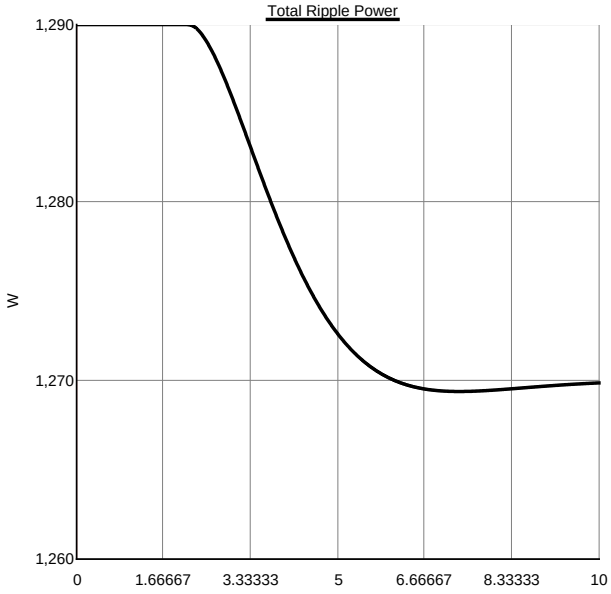

Figure 6.24: Central Inverter Total Power Step Response 2

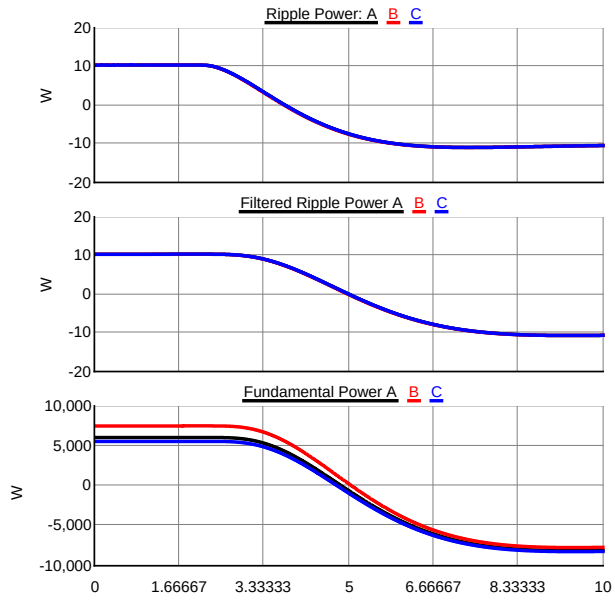

Figure 6.25: Distributed Charger Ripple and Fundamental Power Step Response 1

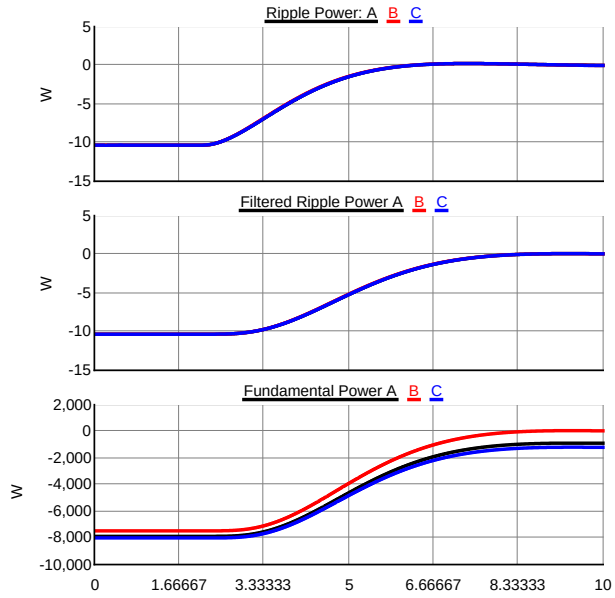

Figure 6.26: Distributed Charger Ripple and Fundamental Power Step Response 2

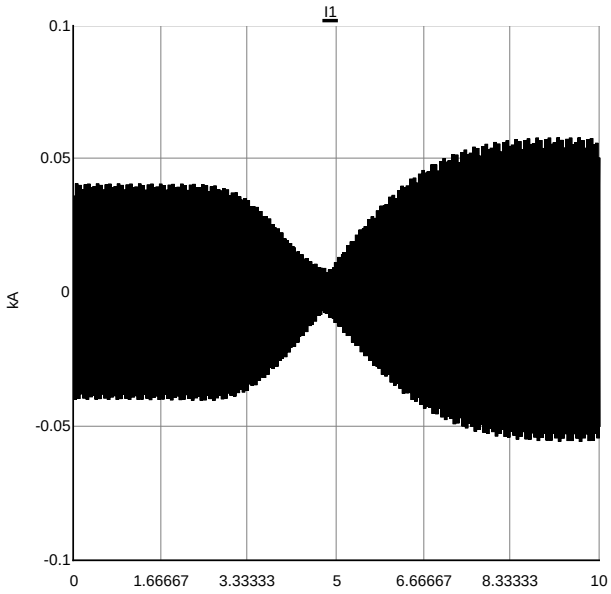

Figure 6.27: Distributed Charger Current Step Response 1

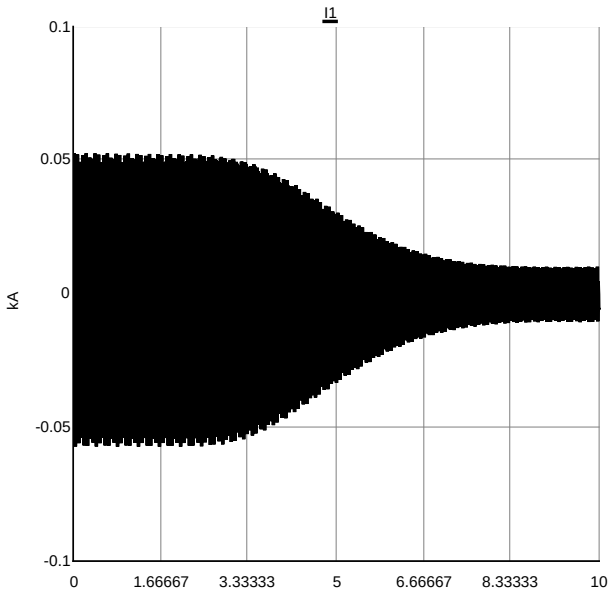

Figure 6.28: Distributed Charger Current Step Response 2

The remaining plots are from simulations which include the Typhoon HIL400 power electronics emulator. The first set of plots are from the initialization after the converter emulation is connected to the grid simulation. Figure 6.29 and Figure 6.30 show the PLL initialization and the ripple control direct and quadrature voltage initialization. The PLL must reach equilibrium before the fundamental current can be controlled. After the fundamental current is controlled and the ripple filters reach equilibrium, the ripple output voltage is regulated to the desired value. Figure 6.31 and Figure 6.32 show the external emulator ripple power and current, while Figure 6.33 shows the central inverter total power during the Typhoon initialization.

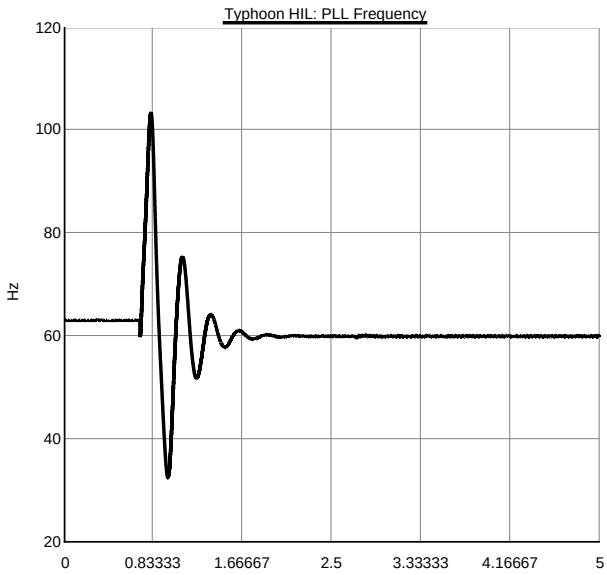

Figure 6.29: External Charger Initialization PLL Frequency

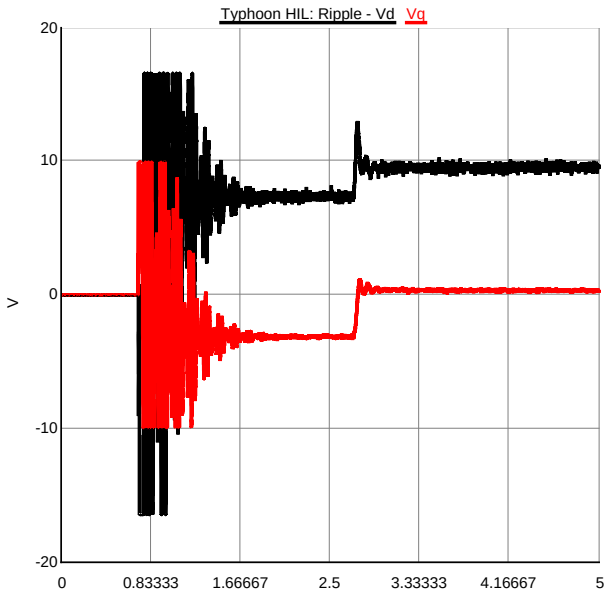

Figure 6.30: External Charger Initialization Ripple Voltage DQ Components

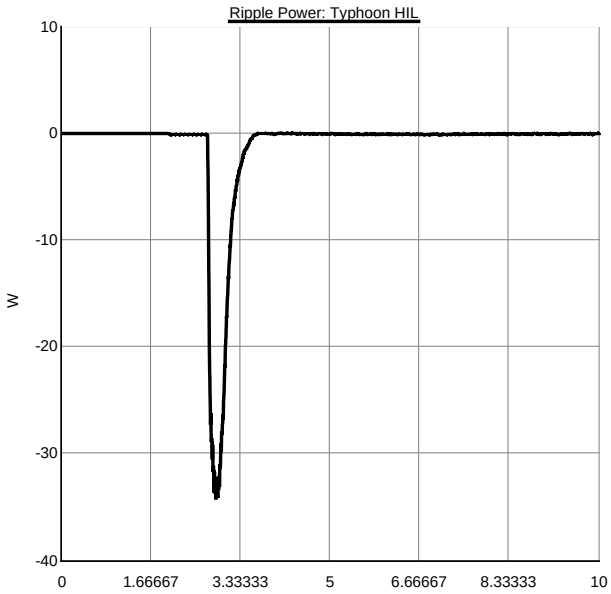

Figure 6.31: External Charger Initialization Ripple Power

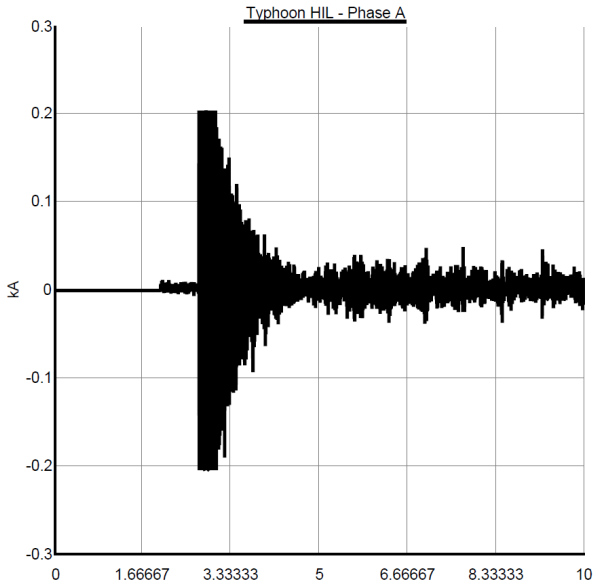

Figure 6.32: External Charger Initialization Current

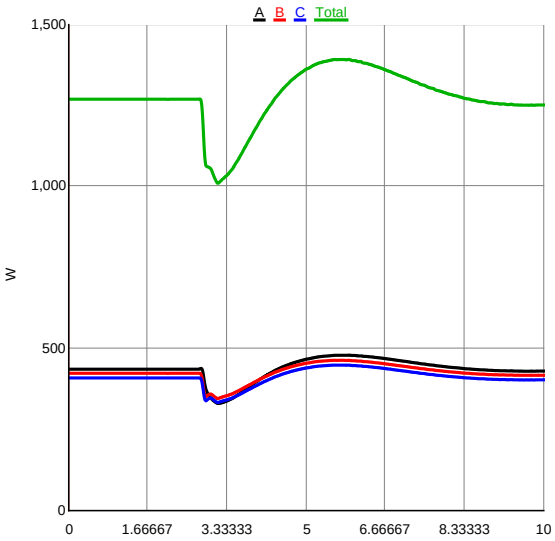

Figure 6.33: Central Ripple Power during External Charger Initialization

The next set of simulations test the dynamic response of the distributed chargers, including the external charger, to commands from the central controller. Additionally, the response of the system is tested upon the removal and re-insertion of the external charger. Figure 6.34 shows the step response of the external charger to a central inverter command from 0 to 10 W. Figure 6.35 shows the same response from all 4 distributed chargers on the system. From this plot, one can see that presence of the external charger in the simulation adds noise to the system. This noise can be seen on the ripple power waveforms. The controllers are able to perform correctly despite this noise. The second plot in Figure 6.35 shows the filtered ripple power, which is used to control the fundamental power. From this figure, one can also compare the response times of the chargers. The external charger takes longer to reach equilibrium since it is located further from the central inverters on the feeder, thus it is separated by a greater impedance. The settling times for many inverters on the system at once is further explored in the system simulation. Figure 6.36 and Figure 6.37 show the step response currents from the external charger and from an internal distributed charger. It can be seen that the external charger current is clearly more noisy than the distributed charger current.

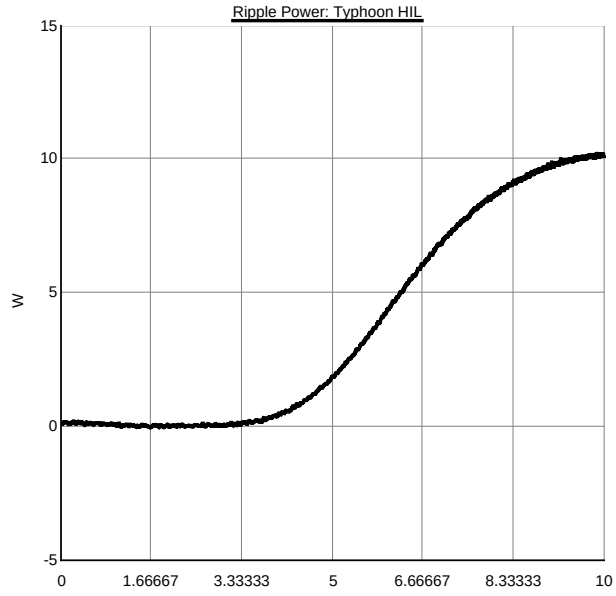

Figure 6.34: External Charger Ripple Power Step Response

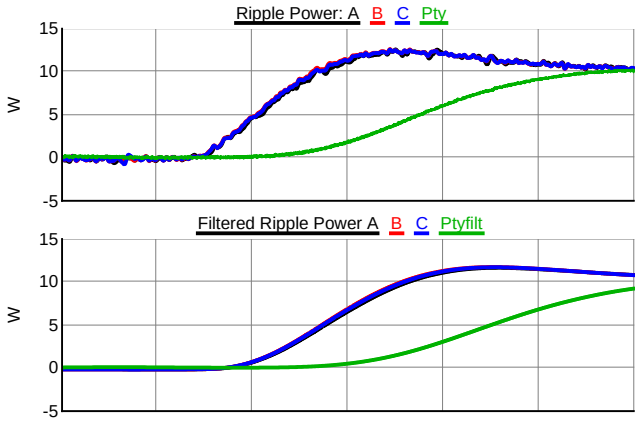

Figure 6.35: Distributed Chargers Ripple Power Step Response

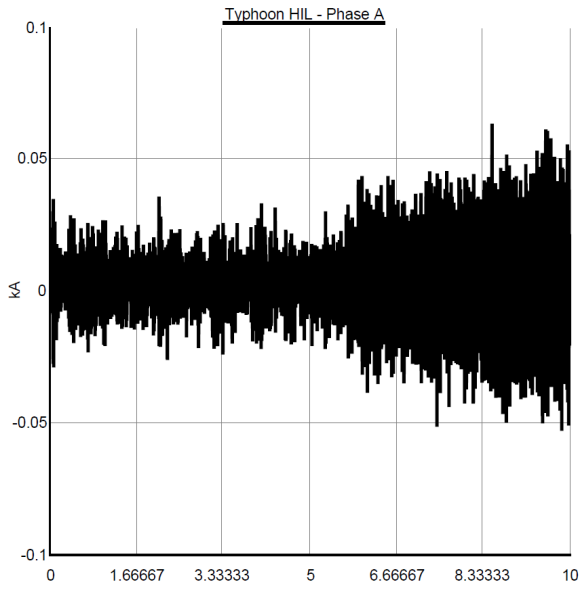

Figure 6.36: External Charger Current Step Response

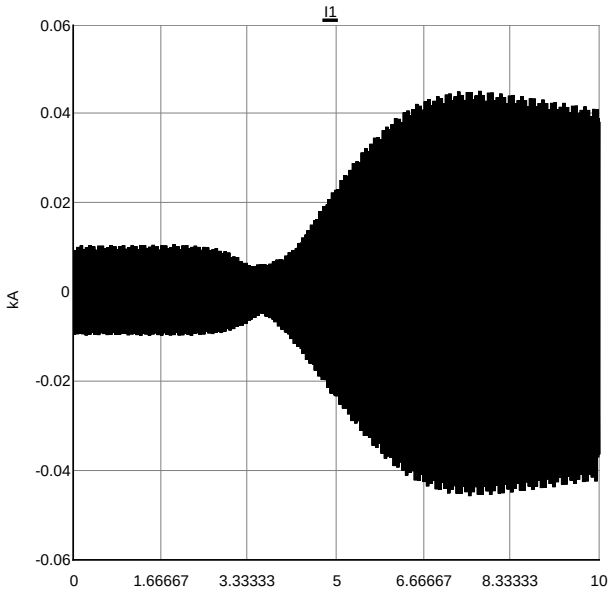

Figure 6.37: Distributed Charger Current Step Response

The next set of plots show the response from the central and distributed chargers as the external charger is disconnected and then reconnected from the system. It can be seen that the distributed chargers take up the missing power that was previously supplied by the external charger when the external charger is removed. They go back to their original value once the external charger is restored. The central ripple power experiences a short disturbance before returning to its previous vales in both the removal and the reinsertion of the external charger. For the disconnection of the external charger, the external charger power, distributed charger power, and central inverter power are plotted in Figure 6.38, Figure 6.39, and Figure 6.40. For the reconnection of the external charger, the external charger power, distributed charger power, and central inverter power are plotted in Figure 6.41, Figure 6.42, and Figure 6.43.

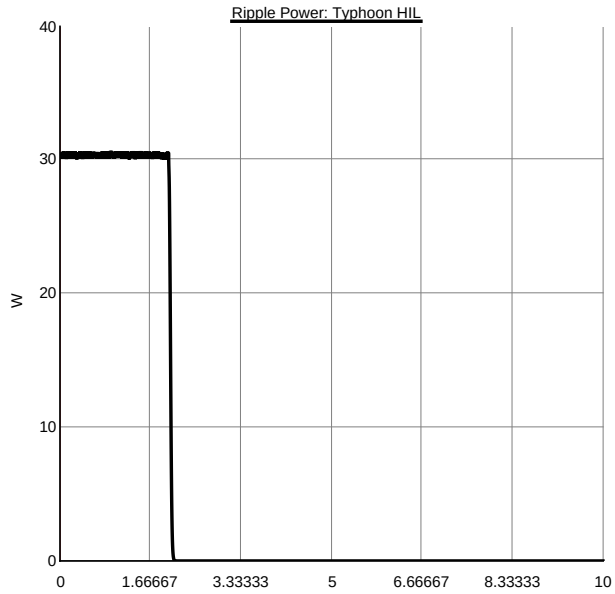

Figure 6.38: External Charger Ripple Power - Disconnection from Grid

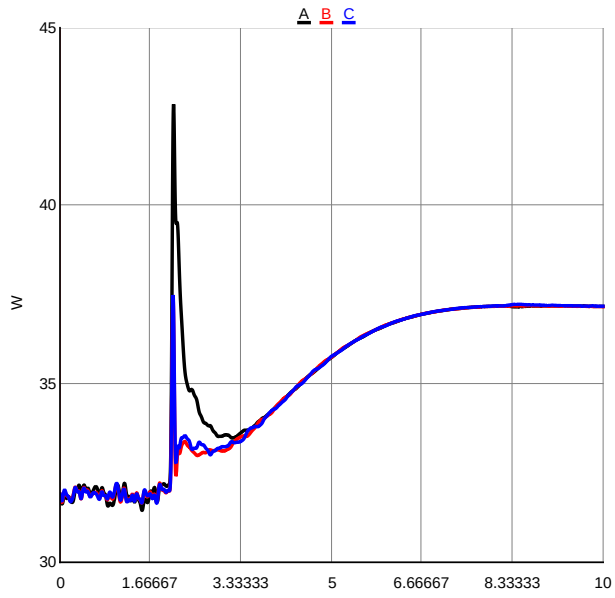

Figure 6.39: Distributed Charger Ripple Power - External Charger Disconnected

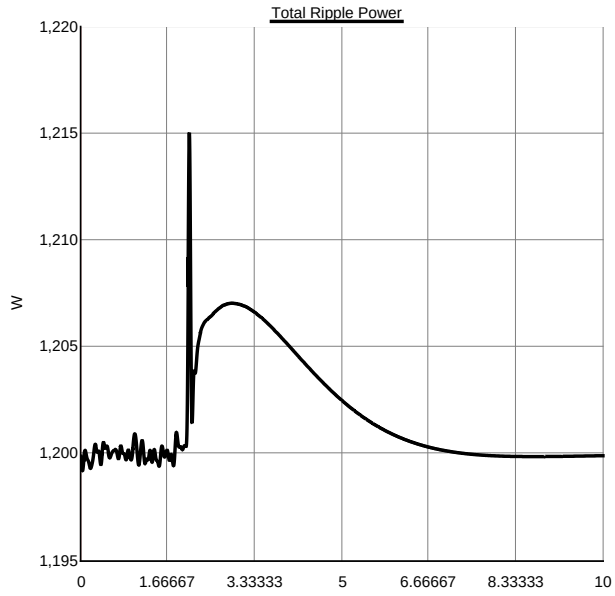

Figure 6.40: Central Charger Ripple Power - External Charger Disconnected

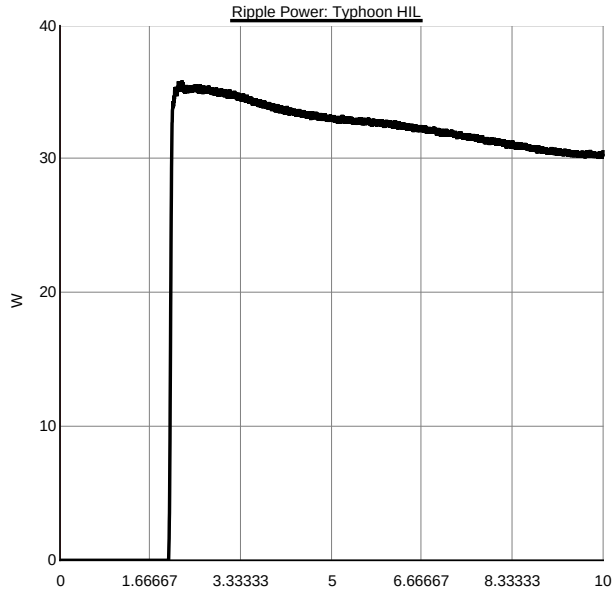

Figure 6.41: External Charger Ripple Power - Re-connection to Grid

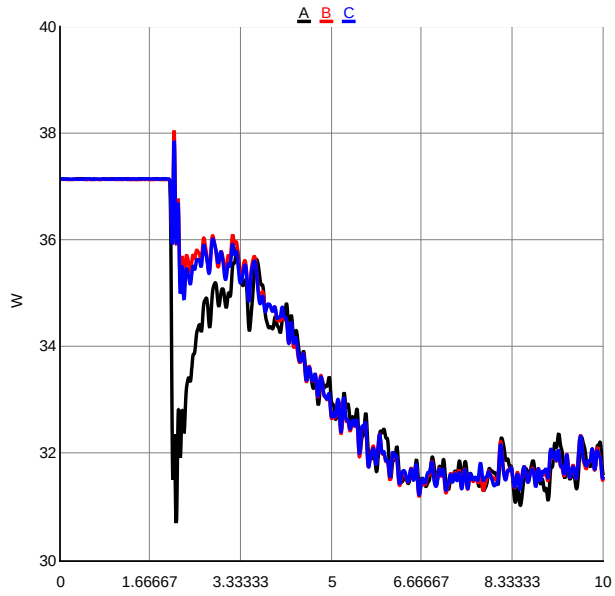

Figure 6.42: Distributed Charger Ripple Power - External Charger Reconnected

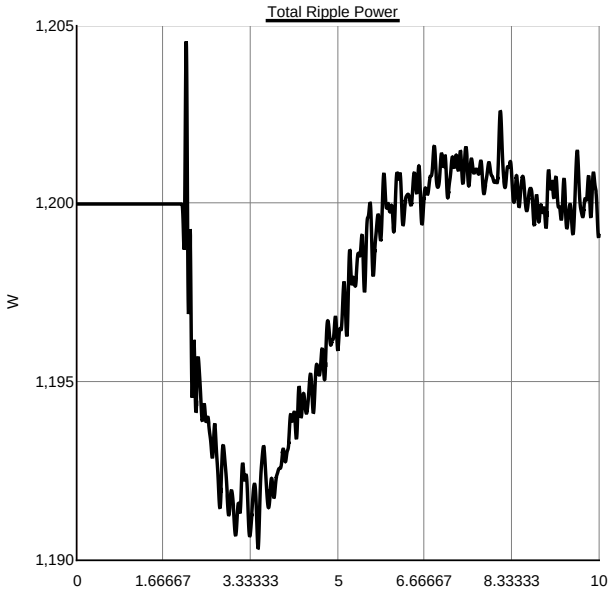

Figure 6.43: Central Charger Ripple Power - External Charger Reconnected

6.3 System Simulation

The previous section described a HIL setup where a limited number of distributed chargers were tested on a distribution feeder. This section describes the simulation of 32 distributed chargers and 3 central inverters on the IEEE 13 bus distribution feeder. This system level simulation is done entirely within the RTDS, where simulations can be performed rapidly and many variations and test cases can be run. The model created for the plots shown in this section was also used to gather the data for leakage power, signal range, and to test the leakage identification technique as presented in the 'Leakage Power' and 'Signal Attributes: Voltage, Frequency, and Power' sections of Chapter 5.

The purpose of the system level simulation is to test the droop dynamics and stability of a large number of distributed chargers on a realistic system with loads. The simulations

test the ability of the central inverter to draw and supply specific quantities of power in the signal and the ability of the distributed inverters to share this quantity equally. Through this simulation, we attempt to show the stability and first order salient dynamics of the system as derived in the 'System Model' chapter of this thesis.

The RSCAD model of the IEEE 13 bus feeder developed for the HIL testing was used as the base for the system model. The limitation of 72 electrical nodes, due to the particular set of processors available in the RTDS system we have, is the determining factor for including 32 distributed chargers in the model. With 32 distributed chargers, there is at least one charger on each bus on each phase of the feeder. With the feeder and distributed chargers consisting of 70 electrical nodes, two nodes are available to insert breakers into the model in order to test the removal of distributed chargers. An overview of the RSCAD model is shown in Figure 6.44.

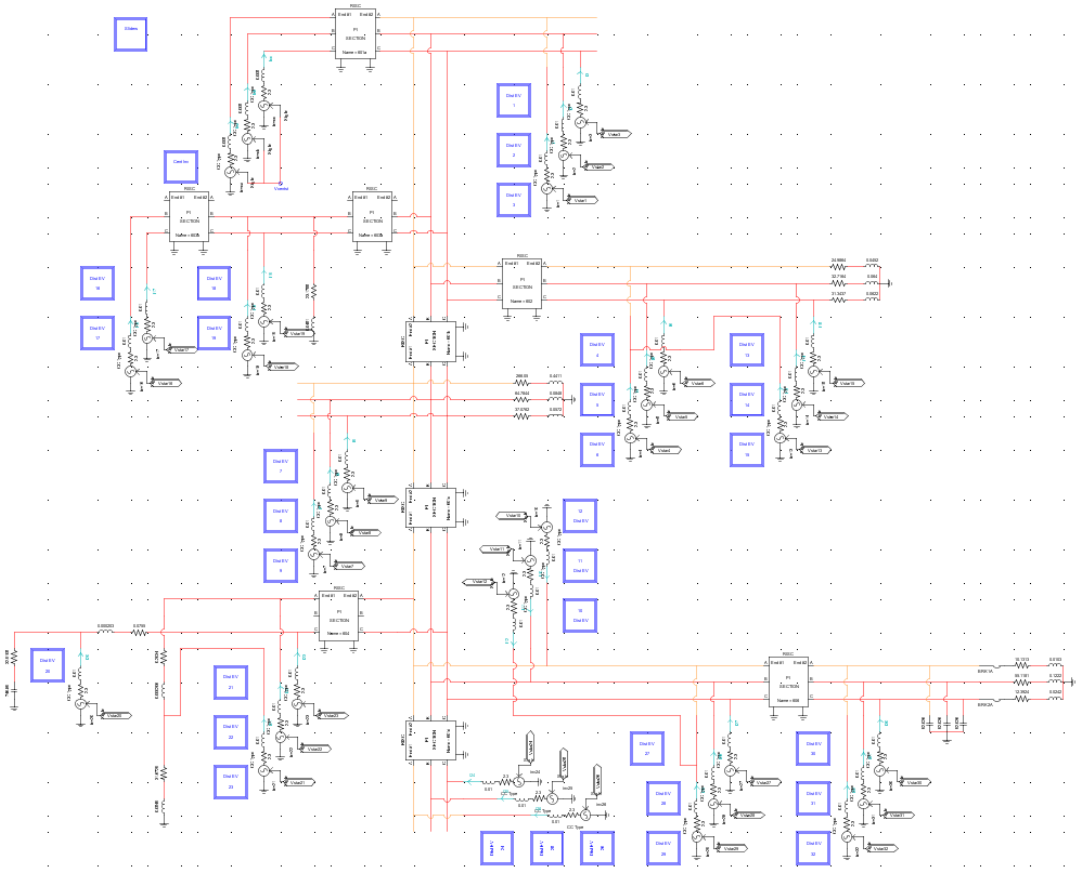

Figure 6.44: Model of Feeder with 3 Central and 32 Distributed Chargers

In order to include such a high number of chargers in the simulation, some simplifications were made to the chargers and their control. First, to greatly reduce the number of control components, the system simulation includes only the ripple voltage and does not include the fundamental frequency voltage. It is not possible to simulate the full ripple droop controller for 35 converters in the RTDS. Simply removing the fundamental part of the control would create short circuits at each distributed charger at fundamental frequency. Since the controller function was successfully demonstrated in the computer simulation and in the HIL simulation, we have decided to remove it here in order to

reduce the complexity of the model. The droop control response is made faster in the system simulation by increasing the droop slope. This is possible since the controller is no longer constrained by decoupling the ripple frequency from the fundamental frequency.

Second, to reduce the number of electrical nodes per charger, the transformer and output filter was removed. The transformer impedance referred to the grid side remains in the model. The justification behind this simplification is that it has been demonstrated in the computer simulation and the HIL simulation that the controller has the ability to regulate the AC capacitor voltage. This simplification assumes that we have direct control of the AC capacitor voltage. The specifications for the RTDS system simulation are summarized in Table 6.4, and a closer look at the simplified chargers and their control is given in Figure 6.45.

Table 6.4: RTDS Model Specifications - System Simulation

RTDS System Simulation	
Central Inverters	3
Distributed Chargers	32
Circuit Breakers	2
Time Step	50 μS
Electrical Nodes	72
Droop Slope	0.137 rad/W
Central Power Integration Factor	0.005
Signal Range	100 W/Charger

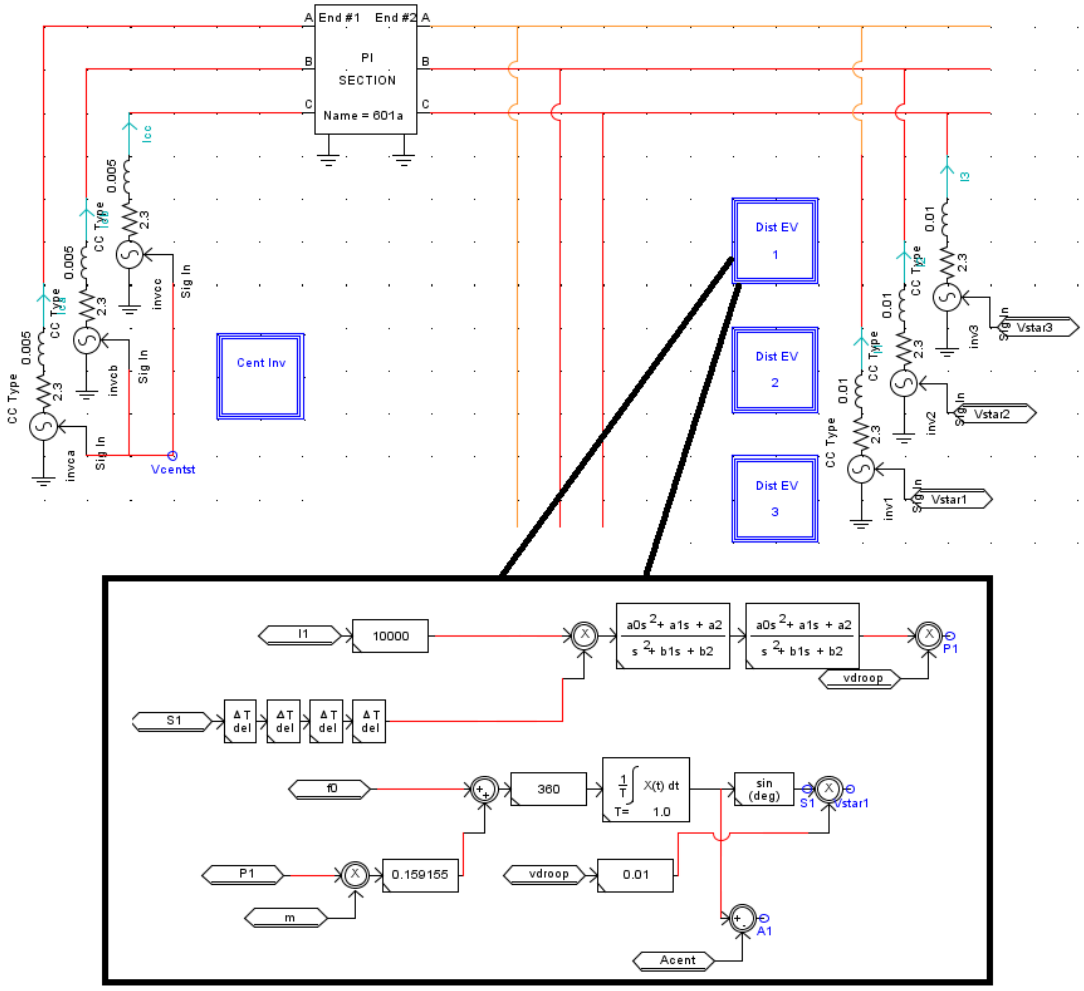

Figure 6.45: Model of Simplified Charger for System Simulation

The simulations and results presented here test the basic operation, stability, and response time of the ripple droop control as well as the flexibility of the control to respond to the removal of distributed chargers. The first two plots show the initialization power for the central inverter, Figure 6.46, and for the 32 distributed inverters, Figure 6.47. Like in the HIL simulations, the initialization is done at the nominal ripple frequency of 90 Hz, such that the distributed chargers should exchange no power with the grid and

reach an equilibrium at 0 W. The central inverters reach an equilibrium at the nominal value for the leakage power. For this case, the nominal leakage power is 1.65 kW total for the three phases. The distributed charger ripple power waveforms are divided among four charts such that the individual dynamics can be seen. For these simulations, the droop slope is set to a high value corresponding to a fast system response. As a result, the dynamics have a small amount of ringing caused by the response of the extraction filters. A smaller droop slope would yield a slower and smoother response. This small level of ringing is deemed acceptable for these simulations.

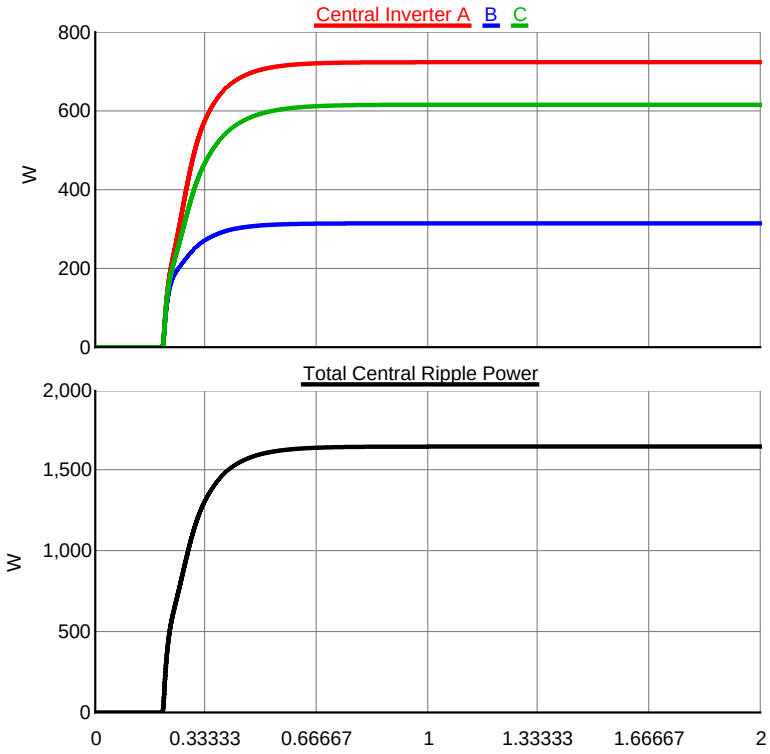

Figure 6.46: Central Inverter Ripple Power during System Initialization

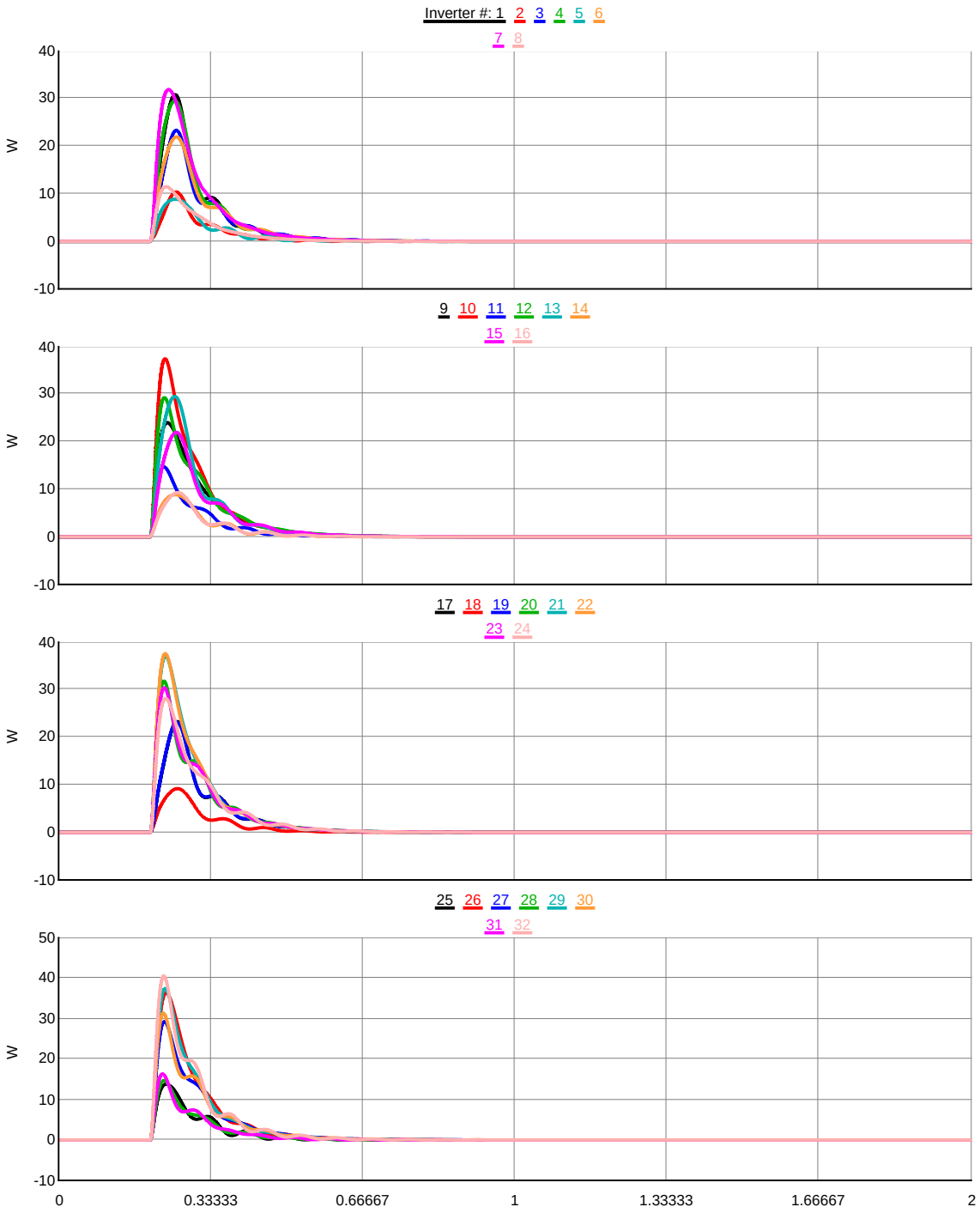

Figure 6.47: Ripple Power of Distributed Inverters during System Initialization

For the next few simulations, the central controller alters its frequency such that a specific total central inverter power is reached. The entire stable range of ripple power is spanned as the central controller goes from commanding nominal 1.65 kW to 3 kW and from 3 kW to -0.6 kW. The signal power of the distributed inverters spans from 0 W to -20W to 80 W, across the entire 100 W range. The initial step response is plotted in Figure 6.48 and Figure 6.49 for the central and distributed chargers. The next step response, going from one end of the signal range to the other, is plotted in Figure 6.50 and Figure 6.51 for the central and distributed chargers. In addition, the angles for each distributed charger with respect to the central inverters is given in Figure 6.52. It can be observed that the angles of the distributed chargers remain within 60 degrees of the central inverter angle.

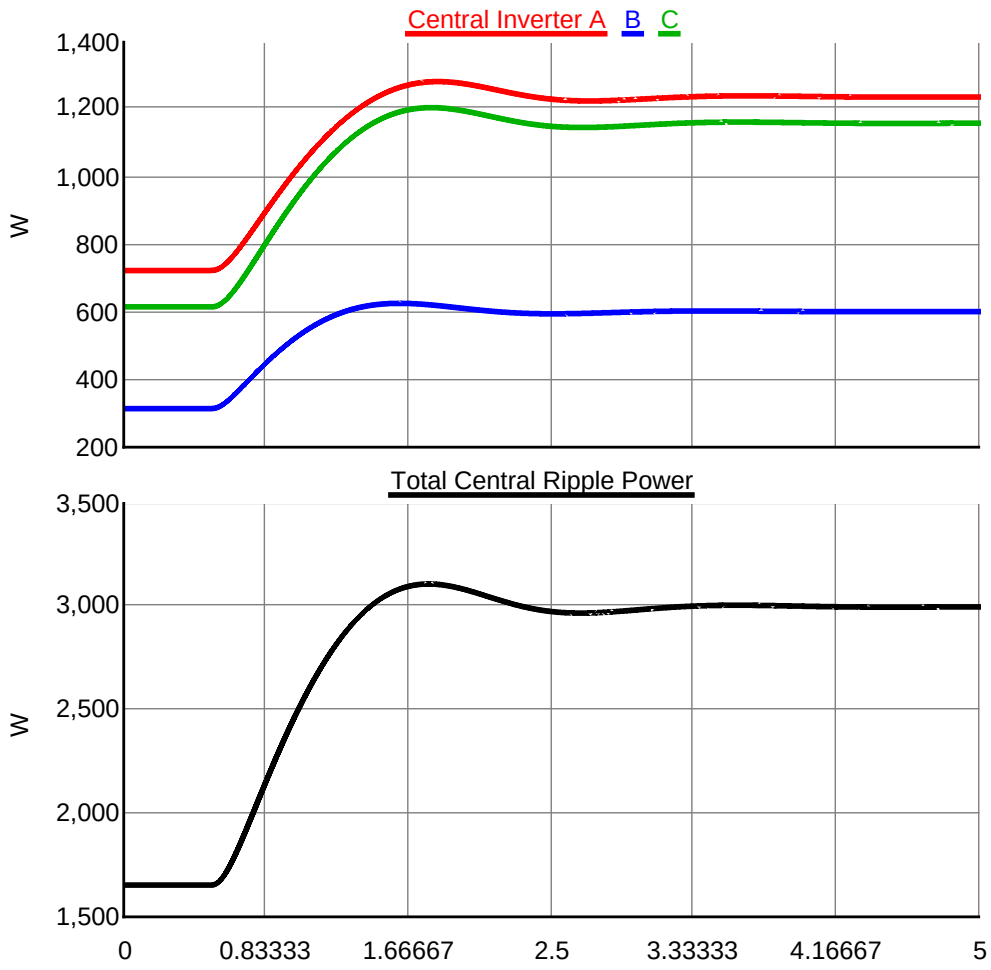

Figure 6.48: Central Inverter Ripple Power System Step Response 1

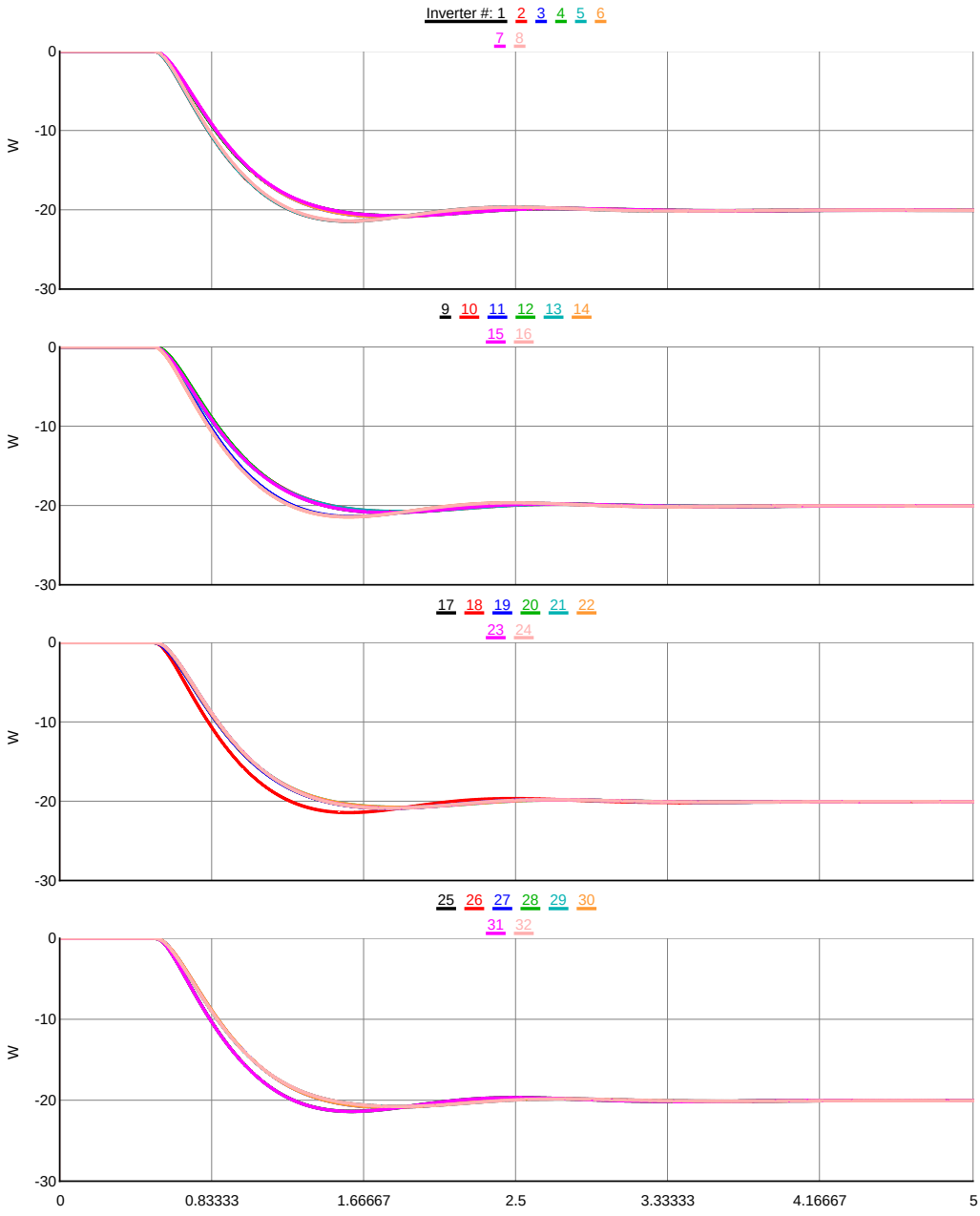

Figure 6.49: Distributed Inverter Ripple Power System Step Response 1

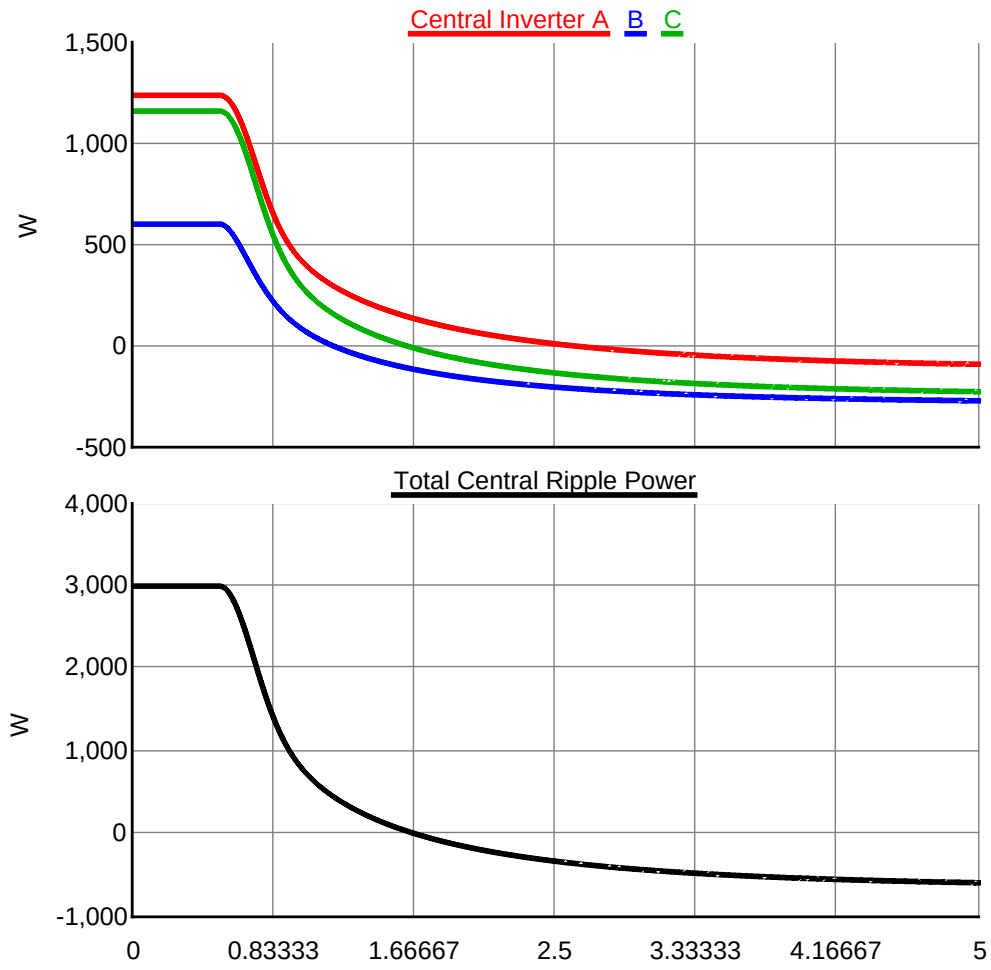

Figure 6.50: Central Inverter Ripple Power System Step Response 2

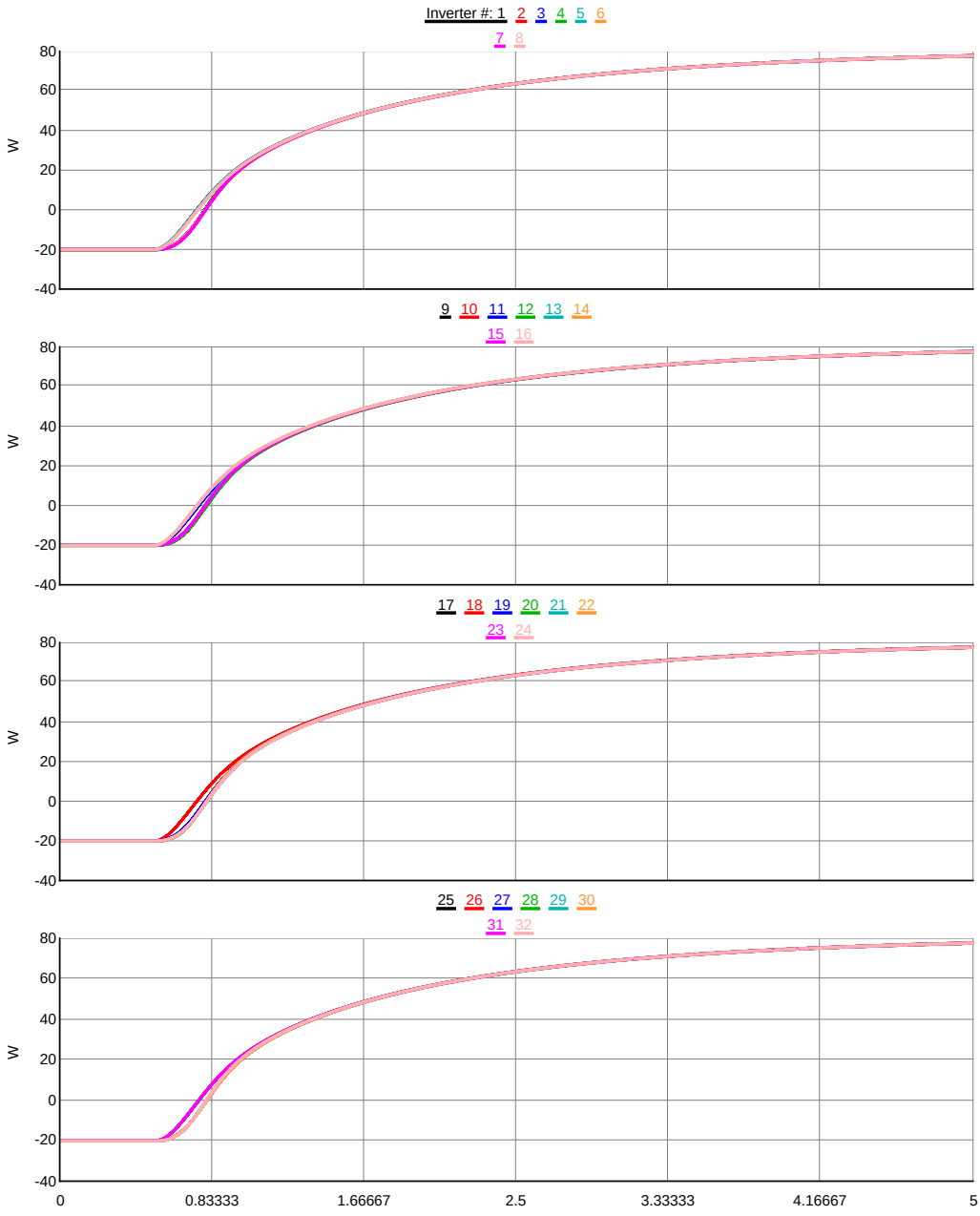

Figure 6.51: Distributed Inverter Ripple Power System Step Response 2

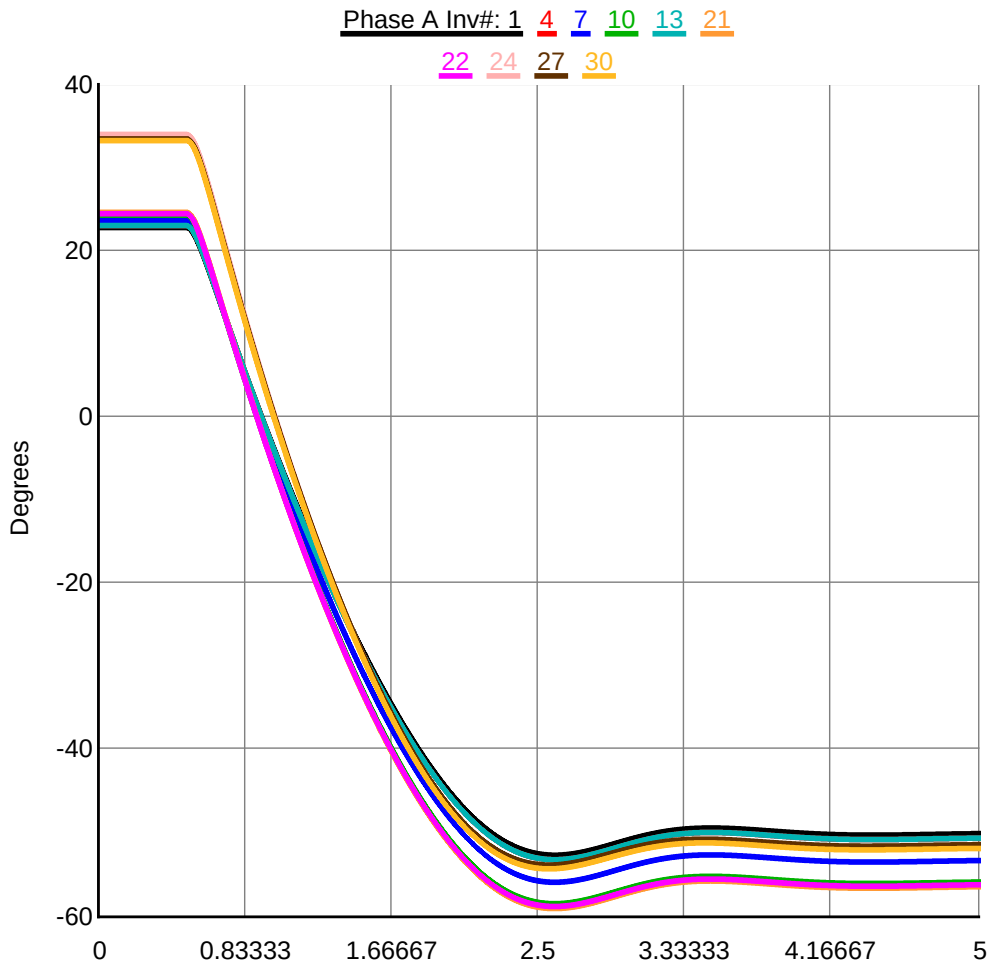

Figure 6.52: Distributed Inverter Ripple Angle System Step Response 2

The final simulation tests the ability of the distributed chargers to share the ripple power requested by the central controller as chargers are dropped. Four chargers are dropped from phase A. The 32 distributed chargers are initially drawing about 7 W of power from the ripple signal. As the four chargers are dropped, the central inverter experiences a drop in its ripple power injected. It then adjusts its frequency to restore the ripple power. The remaining chargers experience an increase in the power they are

drawing from the ripple signal. The distributed charger ripple power waveforms are shown in Figure 6.53. The chargers that are disconnected from the system are chargers number 4, 12, 13, and 29. The central inverter ripple power waveforms are shown in Figure 6.54. It can be seen that the power on Phase A experiences an initial decrease, folllowed by a smaller increase in all three phases.

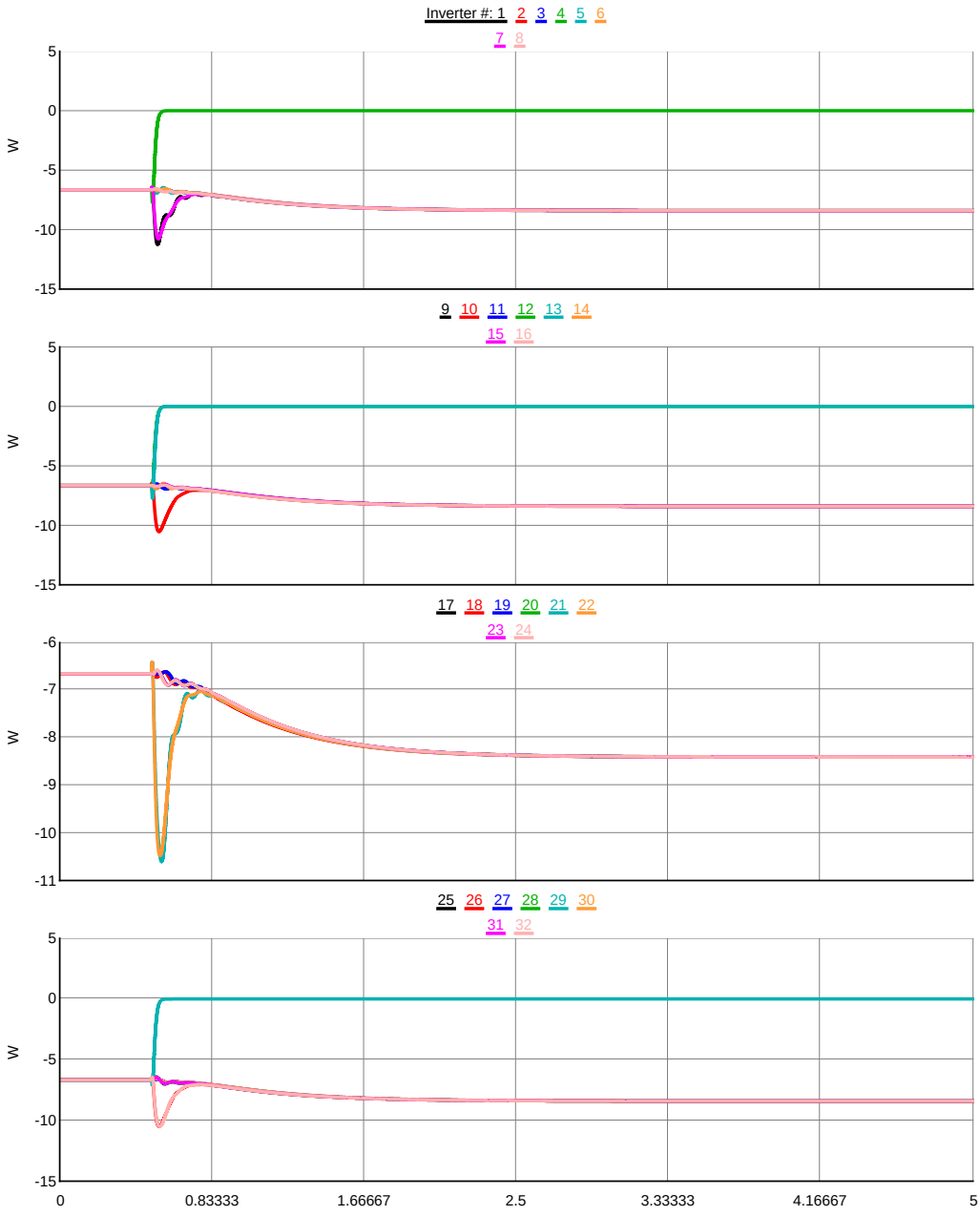

Figure 6.53: Distributed Charger Ripple Power - Disconnection of Four Chargers

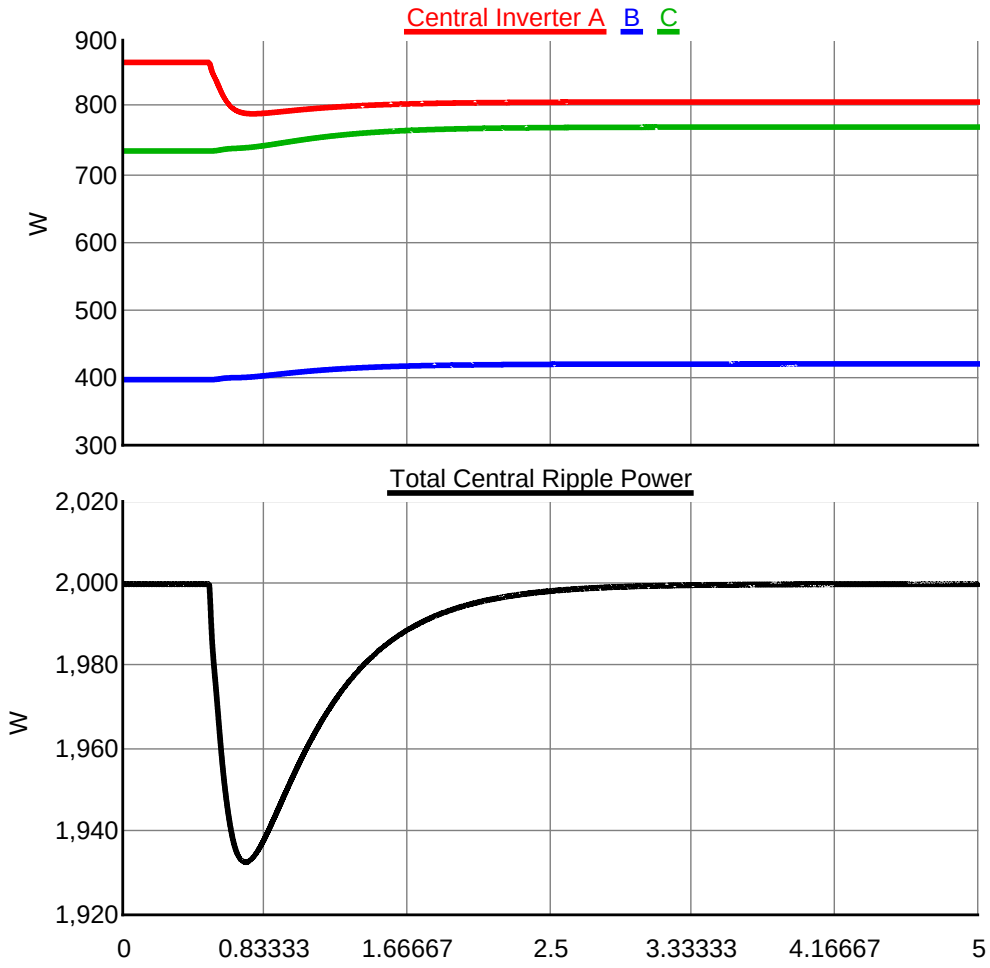

Figure 6.54: Central Inverter Ripple Power - Disconnection of Four Chargers

Chapter 7

Epilogue

7.1 Summary and Conclusions

This work presented a new method to control distributed storage devices on a distribution feeder by a signal injected through the power line. The signal is generated by standard power electronics inverters and requires no special hardware. The method of control uses frequency droop to control the distributed devices from a central inverter. The distributed devices are controlled simultaneously as the system frequency is used as a global variable. With this method, the distributed storage on the feeder is effectively controlled as a single large storage device.

As the importance of storage on the grid grows from the introduction of renewable sources and as the popularity of electric vehicles with storage grows, a method to control the distributed storage devices becomes more important. The proposed method could be adopted to control the distributed storage devices without the need for additional communication hardware.

In this thesis, we attempted to explain the proposed method, to describe a practical

application on a realistic feeder, to model the system, and to discuss practical concerns and limitations of the proposed method. Limitations of ripple droop control are discussed in this work and include the presence of leakage power and the finite operating speed of the frequency droop control. The leakage power caused by passive loads and active devices on the feeder presents a challenge to ripple droop control since it disrupts the conservation of power. We addressed this limitation by proposing the received power identification technique. In the 'Power Electronics and Control Section' we outlined the limitations on the speed of the ripple droop controller and concluded that a settling time of around 2.5 seconds is the fastest achievable time.

Finally, an attempt to demonstrate ripple droop control was made through simulation and HIL experimentation. The IEEE 13 bus feeder with 32 distributed EV chargers was simulated with the Real-Time-Digital-Simulator and the basic operation of ripple droop control was demonstrated. The full feeder with a smaller number of chargers was included in a HIL experiment with an external power electronics switching emulator. This experiment verified the operation full ripple droop controller to regulate both fundamental and ripple frequency signals.

7.2 Extension

An extension of this work could include testing and verifying the operation of ripple droop control with alternate feeders. A simulation could be performed with distributed chargers on feeders of different sizes. This could further verify the leakage estimation technique. In addition, the immunity of ripple droop control to to noise and active loads could be further verified through a more detailed simulation. Furthermore, with sufficient resources available, testing ripple droop control on an actual feeder or a very detailed

feeder emulator would be valuable in verification.

For the ripple droop controller development, an extension could include better understanding and minimization of transient power when distributed chargers are connected to the line. A more smooth synchronization of the chargers would increase system robustness.

Lastly, the contingency backup inverter and the planned and unplanned shutdown and startup procedures presented in the 'Practical System Considerations' subsection could be further verified in HIL experiments for the 13 bus feeder and for other feeders.

REFERENCES

[1] EPRI-DOE Handbook of Energy Storage for Transmission and Distribution Applications, EPRI, Palo Alto, CA, and the U.S. Department of Energy, Washington, DC: 2003. 1001834.

[2] pluginamerica.org.

[3] IEC, 61850-5: Communication requirements for functions and device models, IEC. 2002.

[4] Summary of KEMA validation report: Two megawatt advanced lithium-ion BESS successfully demonstrates potential for utility applications. *KEMA, Inc. report for The AES Corp. [Online]*, June 2008.

[5] A. R. Bergen. *Power System Analysis*. Englewood Cliffs, NJ: Prentice-Hall, 1986.

[6] J. Cai, Z. Huang, J. Hauer, and K. Martin. Current status and experience of wams implementation in North America. *IEEE/PES Transmission and Distribution Conference and Exhibition (Asia and Pacific)*, 2005.

[7] M.C. Chandorkar, D.M. Divan, and R. Adapa. Control of parallel connected inverters in standalone AC supply systems. *Industry Applications, IEEE Transactions on*, 29(1):136–143, Jan 1993.

[8] C.Y. Chang, C.J. Wu, C.T. Chang, C.H. Lin, J.L. Yen, T.G. Lu, and W.C. Chang. Experiences of direct load control using ripple signals in Taiwan Power System. *Advances in Power System Control, Operation and Management*, 2:591–596, Nov. 1997.

[9] Po-Tai Cheng and Tzung-Lin Lee. A Dynamic Tuning Method for Distributed Active Filter Systems, Industry Applications Conference, 2006. 41st IAS Annual Meeting. Conference Record of the 2006 IEEE. 1:175–182, Oct. 2006.

[10] T. Cleary, McGill R., K. Sikes, S. Hadley, V. Marano, E. Ungar, and T Gross. Plug-In Hybrid Electric Vehicle Value Proposition Study, Oak Ridge National Laboratory. 2010.

[11] D. C. Erb, O. C. Onar, and A. Khaligh. Bi-Directional Charging Topologies for Plug-in Hybrid Electric Vehicles. *Proceedings of IEEE Applied Power Electronics Conference and Exposition*, pages 2066–2072, Feb 2010.

[12] J. Eto, J. Undrill, P. Mackin, R. Daschmans, B. lliams, B. Haney, R. Hunt, J. Ellis, H. Illian, C. Martinez, M. OMalley, K. Coughlin, and K LaCommare. Use of Frequency Response Metrics to Assess the Planning and Operation Requirements for Reliable Integration of Variable Renewable Generation, Lawrence Berkeley National Laboratory. 2010.

[13] J. Eyer and G Corey. Energy Storage for the Electricity Grid: Benefits and Market Potential Assessment Guide, Sandia National Laboratories. 2010.

[14] J. Eyer, J. Iannucci, and G Corey. Energy Storage Benefits and Market Analysis Handbook, Sandia National Laboratories. 2004.

[15] J. Eyer and S Schoenung. Benefit/Cost Framework for Evaluating Modular Energy Storage, Sandia National Laboratories. 2008.

[16] H. Ferreira, L. Lampe, J. Newbury, and T Swart. *Power Line Communications: Theory and Applications for Narrowband and Broadband Communications over Power Lines*. John Wiley and Sons, LTD., 2010.

[17] J.M. Guerrero, L.G. de Vicuna, J. Matas, M. Castilla, and J. Miret. A wireless controller to enhance dynamic performance of parallel inverters in distributed generation systems. *Power Electronics, IEEE Transactions on*, 19(5):1205–1213, Sept. 2004.

[18] J.M. Guerrero, J.C. Vasquez, J. Matas, L.G. de Vicuna, and M Castilla. Hierarchical Control of Droop-Controlled AC and DC MicrogridsA General Approach Toward Standardization. *Industrial Electronics, IEEE Transactions on*, 58(1):158–172, Jan. 2011.

[19] L. Hossenlopp. Engineering perspectives on IEC 61850. *Power and Energy Magazine, IEEE*, 5(3):45–50, May-June 2007.

[20] P. Karlsson, J. Bjornstedt, and M. Strom. Stability of voltage and frequency control in distributed generation based on parallel-connected converters feeding constant power loads, Power Electronics and Applications 2005 European Conference on. page 10.

[21] F. Katiraei and M.R. Iravani. Power Management Strategies for a Microgrid With Multiple Distributed Generation Units. *Power Systems, IEEE Transactions on*, 21(4):1821–1831, Nov. 2006.

[22] T. Khalifa, K. Naik, and A. Nayak. A survey of communication protocols for automatic meter reading applications. *Communication Survey and Tutorials*, pages 1–6, Second Quarter 2011.

[23] Jaehong Kim, J.M. Guerrero, P. Rodriguez, R. Teodorescu, and Kwanghee Nam. Mode Adaptive Droop Control With Virtual Output Impedances for an Inverter-Based Flexible AC Microgrid. *Power Electronics, IEEE Transactions on*, 26(3):689–701, March 2011.

[24] M. Kintner-Meyer, P. Balducci, C. Jin, T. Nguyen, M. Elizondo, V. Viswanathan, X. Guo, and F Tuffner. Energy Storage for Power Systems Applications: A Regional Assessment for the Northwest Power Pool (NWPP), Pacific Northwest National Laboratory. 2010.

[25] H. Laaksonen, P. Saari, and R. Komulainen. Voltage and frequency control of inverter based weak LV network microgrid, Int. Conf. Future Power Syst., Amsterdam, the Netherlands. Nov.18, 2005.

[26] Tzung-Lin Lee and Po-Tai Cheng. Design of a New Cooperative Harmonic Filtering Strategy for Distributed Generation Interface Converters in an Islanding Network. *Power Electronics, IEEE Transactions on*, 22(5):1919–1927, Sept. 2007.

[27] R. Majumder, B. Chaudhuri, A. Ghosh, R. Majumder, G. Ledwich, and F. Zare. Improvement of Stability and Load Sharing in an Autonomous Microgrid Using Supplementary Droop Control Loop. *Power Systems, IEEE Transactions on*, 25(2):796–808, May 2010.

[28] R. Majumder, G. Ledwich, A. Ghosh, S. Chakrabarti, and F Zare. Droop Control of Converter-Interfaced Microsources in Rural Distributed Generation. *Power Delivery, IEEE Transactions on*, 25(4):2768–2778, Oct. 2010.

[29] Y.V. Makarov, Du Pengwei, M.C.W. Kintner-Meyer, Chunlian Jin, and H.F. Illian. Sizing Energy Storage to Accommodate High Penetration of Variable Energy Resources. *Sustainable Energy, IEEE Transactions on*, 3(1):34–40, Jan. 2012.

[30] P.K. Olulope, K.A. Folly, S. Chowdhury, and S.P. Chowdhury. Dynamic impact and assessment of stability of power systems with dg penetration: A review, Universities Power Engineering Conference (UPEC), 2010 45th International. pages 1–6, Aug. 31 2010-Sept. 3 2010.

[31] IEEE P519.1/D12. IEEE Draft Guide for Applying Harmonic Limits on Power Systems. pages 1–124, July 2012.

[32] Muhamad Reza. Stability analysis of transmission systems with high penetration of distributed generation, PhD Thesis, Delft University of Technology. 2006.

[33] T.W. Ross and R.M.A. Smith. Centralized ripple control on high-voltage networks. *Electrical Engineers - Part II: Power Engineering, Journal of the Institution of*, 95(47):470–480, October 1948.

[34] Schoenung S. Energy Storage Systems Cost Update, Sandia National Laboratories. 2011.

[35] R. Santos Filho, P. Seixas, P. Cortizo, L. Torres, and A. Souza. Comparison of Three Single-Phase PLL Algorithms for UPS Applications. *Industrial Electronics, IEEE Transactions on*, 55(8):2923–2932, Aug. 2008.

[36] S. Schey, D. Scoffield, and J Smart. A First Look at the Impact of Electric Vehicle Charging on the Electric Grid in The EV Project, EVS26 International Battery, Hybrid and Fuel Cell Electric Vehicle Symposium. May 6-9, 2013.

[37] IEEE 13 Node TestFeeder. Distribution System Analysis Subcommittee Report. *Ieee Transactions*, 2003.

[38] F. Tuffner and M Kintner-Meyer. Using Electric Vehicles to Meet Balancing Requirements Associated with Wind Power, Pacific Northwest National Laboratory. 2011.

[39] A. Tuladhar, Hua Jin, T. Unger, and K. Mauch. Control of parallel inverters in distributed AC power systems with consideration of line impedance effect. *Industry Applications, IEEE Transactions on*, 36(1):131–138, Jan/Feb 2000.

[40] Anil Tuladhar. Advanced Control Techniques for Parallel Inverter Operation without Control Interconnections, PhD Thesis, The University of British Columbia. 2000.

[41] T. Vandoorn, B. Meersman, J. De Kooning, and L. Vandevelde. Controllable Harmonic Current Sharing in Islanded Microgrids: DG Units With Programmable Resistive Behavior Toward Harmonics. *Power Delivery, IEEE Transactions on*, 27(2):831–841, April 2012.

[42] T. L. Vandoorn, B. Meersman, J. D. M. De Kooning, and L. Vandevelde. Analogy Between Conventional Grid Control and Islanded Microgrid Control Based on a Global DC-Link Voltage Droop. *Power Delivery, IEEE Transactions on*, 27(3):1405–1414, July 2012.

[43] C. Vartanian. Grid stability battery systems for renewable energy success. *A123 Systems [Online]*.

[44] J. Wishart and J Francfort. The Development of a Charge Protocol to Take Advantage of Off- and On-Peak Demand Economics at Facilities, Idaho National Laboratory. 2012.

[45] M. Yilmaz and P. T. Krein. Rreview of Battery Charger Topologies, Charging Power Levels, and Infrastructure for Plug-In Electric and Hybrid Vehicles. *Power Electronics, IEEE Transactions on*, 28(5):2151–2169, May 2013.

[46] Zhihui Yuan, S.W.H. de Haan, J.B. Ferreira, and D. Cvoric. A FACTS Device: Distributed Power-Flow Controller (DPFC). *Power Electronics, IEEE Transactions on*, 25(10):2564–2572, Oct. 2010.

[47] X. Yuzhe and C. Fischione. Real-time scheduling in LTE for smart grids. *Communications Control and Signal Processing (ISCCSP), 2012 5th International Symposium on*, pages 1–6, May 2012.